Thermomechanical characterization of NiTiNOL and NiTiNOL based structures using ACES methodology

A Dissertation
Submitted to the Faculty
of the

Worcester Polytechnic Institute

in partial fulfillment of the requirement for the
Doctor of Philosophy
in
Mechanical Engineering
by

Shivananda Pai Mizar

2 December 2005

Approved:

Prof. Ryszard J. Pryputniewicz, Major Advisor

Prof. Isa Bar-On, Member, Dissertation Committee

Prof. Richard D. Sisson Jr., Member, Dissertation Committee

Prof. Gretar Tryggvason, Member, Dissertation Committee

Dr. Gordon C. Brown, Member, Dissertation Committee
Director of Engineering, Cambrius, Waltham, MA

Prof. Yiming Rong, Graduate Committee Representative

SUMMARY

Recent advances in materials engineering have given rise to a new class of materials known as active materials. These materials when used appropriately can aid in development of smart structural systems. Smart structural systems are adaptive in nature and can be utilized in applications that are subject to time varying loads such as aircraft wings, structures exposed to earthquakes, electrical interconnections, biomedical applications, and many more. Materials such as piezoelectric crystals, electrorheological fluids, and shape memory alloys (SMAs) constitute some of the active materials that have the innate ability to response to a load by either changing phase (e.g., liquid to solid), and recovering deformation. Active materials when combined with conventional materials (passive materials) such as polymers, stainless steel, and aluminum, can result in the development of smart structural systems (SSS). This Dissertation focuses on characterization of SMAs and structures that incorporate SMAs. This characterization is based on a hybrid analytical, computational, and experimental solutions (ACES) methodology.

SMAs have a unique ability to recover extensive amounts of deformation (up to 8% strain). NiTiNOL (NOL: Naval Ordinance Lab) is the most commonly used commercially available SMA and is used in this Dissertation. NiTiNOL undergoes a solid-solid phase transformation from a low temperature phase (Martensite) to a high temperature phase (Austenite). This phase transformation is complete at a critical

temperature known as the transformation temperature (TT). The low temperature phase is softer than the high temperature phase (Martensite is four times softer than Austenite).

In this Dissertation, use of NiTiNOL in representative engineering applications is investigated. Today, the NiTiNOL is either in ribbon form (rectangular in cross-section) or thin sheets. In this Dissertation, NiTiNOL is embedded in parent materials, and the effect of incorporating the SMA on the dynamic behavior of the composite are studied. In addition, dynamics of thin sheet SMA is also investigated. The characterization is conducted using state-of-the- art (SOTA) ACES methodology. The ACES methodology facilitates obtaining an optimal solution that may otherwise be difficult, or even impossible, to obtain using only either an analytical, or a computational, or an experimental solution alone. For analytical solutions energy based methods are used. For computational solutions finite element method (FEM) are used. For experimental solutions time-average optoelectronic holography (OEH) and stroboscopic interferometry (SI) are used.

The major contributions of this Dissertation are:

1. Temperature dependent material properties (e.g., modulus of elasticity) of NiTiNOL based on OEH measurements.
2. Thermomechanical response of representative composite materials that incorporate NiTiNOL “fibers”.

The Dissertation focuses on thermomechanical characterization of NiTiNOL and representative structures based on NiTiNOL; this type of an evaluation is essential in gainfully employing these materials in engineering designs.

ACKNOWLEDGEMENTS

First of all I would like to thank my advisor Professor Ryszard J. Pryputniewicz for giving me the opportunity to work in the very interesting area of shape memory alloys. I would also like to specially thank Peter Hefti, Optoelectronic Specialist, for his valuable advice during my experimental phase and for assisting me in experimental phase of my Dissertation. I would also like to thank Dr. William C.S. Weir, Robotics Labs at WPI for helping me in the manufacture of the NiTiNOL composites used in this Dissertation. I would like to thank my fellow colleagues, Ryan Marinis, Adam Klempner, and Dr. Wei Han at the CHSLT for their support. Most important of all I would like to thank my wife Sonia for her support, and unconditional love, and also our little bundle of joy, my baby girl Sanjna for sticking by me tirelessly and making this dream of mine materialize. I would like to also thank my rest of the family for being there for me throughout all the years I was a student.

Thank you.

Table of contents

List of figures

List of tables

NOMENCLATURE

$\cos(ky)$	particular solution to the equation of motion of a prismatic beam
$\cosh(ky)$	particular solution to the equation of motion of a prismatic beam
dE_{el}	reversible part of the interfacial and elastic deformation energies
df_M	transformed fraction increment
dG_c	increment of absorbed, or dissipated energy
dG_R	reversible energy of non chemical nature associated with the transformation
dH	change in enthalpy
dQ	heat exchange between the SMA crystal and its surroundings, or latent heat of the phase transformation
dS	change in entropy of the SMA crystal
dW	work accomplished as a result of the heat exchange dQ, or mechanical work
dW_i	energy dissipated that represents irreversible energy loss
dV	change in volume of the SMA crystal
f	resonant frequency, or finish temperature of phase transformation
f_M	fraction of Martensite that has been transformed into Austenite
fps	frames per second
h	thickness, or thickness of the composite
m	matrix portion of a composite
n	a discrete value of a solution, or a mode shape, or the number of elements in a FEM mesh
p	pressure
s	start temperature of phase transformation
$\sin(ky)$	particular solution to the equation of motion of a prismatic beam
$\sinh(ky)$	particular solution to the equation of motion of a prismatic beam
t	time
u	displacement field of a plate
v	displacement field of a plate
u^0, v^0	inplane displacements
w	deflection of a plate, or displacement field of a plate, or transverse displacement
A	cross sectional area, or Austenite
A_f	Austenite finish temperature
A_s	Austenite start temperature
A_r	amplitude of irradiance distribution of the reference beam
A_{t_o}	amplitude of irradiance distribution of the vibrating object
A_{mn}, B_{mn}, C_{mn}	undetermined coefficients from Ritz method for vibration of a plate

B	lattice deformation as a result of the formation of Martensite from the parent phase, or phasor bias
B_{ij}	stiffness term affecting bending-stretching term of a plate
C	arbitrary constant
C_1, C_2, C_3, C_4	constants determined based on the conditions at the end of a prismatic beam
D_{ij}	function of the effective moduli of the composite
D_{11}	dynamic stiffness
E	modulus of elasticity, or internal energy
E_f	modulus of elasticity in the fibers
EI	flexural rigidity of a prismatic beam
E_{AVG}	average modulus of elasticity of NiTiNOL
E_{B1}	modulus of elasticity determined from the first bending mode
E_{B2}	modulus of elasticity determined from the second bending mode
E_{B3}	modulus of elasticity determined from the third bending mode
E_{B4}	modulus of elasticity determined from the fourth bending mode
E_{AVG}	average modulus of elasticity
E_L	modulus of elasticity in the longitudinal direction
E_m	modulus of elasticity in the matrix
G	Gibbs free energy
G-code	commonly used CNC programming protocol
G^M	Gibbs free energy for the martensitic phase
G^P	Gibbs free energy for the parent phase (Austenite)
G^*	generalized form of the Gibbs free energy
H	enthalpy
H^M	enthalpy of the martensitic phase
H^P	enthalpy for the parent phase (Austenite)
I	moment of inertia
I_{a_t}	local average background irradiance from scattered light of the vibrating object
I_h	general irradiance
I_{h_t}	general irradiance of a vibrating object
I_{m_t}	local maximum irradiance
I_{t_o}	irradiance distribution of the vibrating object
I_r	irradiance distribution of the reference beam
I_{tn}	irradiance distribution for the *n*-th sequential frame
$I_{h_{t1}}(x,y)$	irradiance distribution corresponding to the first time-average hologram
$I_{h_{t2}}(x,y)$	irradiance distribution corresponding to the second time-average hologram

$I_{h_{t_3}}(x,y)$	irradiance distribution corresponding to the third time-average hologram
J_o	zero-order Bessel function of the first kind
$\mathbf{K_1}$ and $\mathbf{K_2}$	directions of illumination and observation vectors
K_i	stiffness of the NiTiNOL composites for mode i
L, L_{eff}	active length, or longitudinal direction in a composite
M	Martensite, or characteristic function that modulates the interference of the two fields due to the motion of the object, or bending moment
$M\left[\Omega_t(x,y)\right]$	characteristic function
M_d	temperature at which critical stress required to induce Martensite is greater than the stress required to move the dislocations
M_f	Martensite finish temperature
M_s	Martensite start temperature, or shifted Martensite start temperature
$N_x^i,\ N_y^i,\ N_z^i$	initial inplane force resultants applied to a plate in a pre-buckled state
P	pressure
P_2	lattice invariant shear as a result of twinning, slip, or faulting
$Q(\sigma)$	latent heat of phase transformation
R	lattice rotation
R-phase	type of SME
R_{PP}	critical stress
S	entropy
S^M	entropy of the martensitic phase
S^P	entropy of the parent phase (Austenite)
T	transverse direction, or temperature, or kinetic energy of an elastic body
T_o	transition temperature
TdS_i	reversible heat loss
U	internal energy, or strain energy of an elastic body
U_{mn}	known displacement functions used in the solution of a vibrating plate
V	volume, or potential energy of an elastic body due to inplane loads
V_{mn}	known displacement functions used in the solution of a vibrating plate
V_o	volume of the SMA crystal
$V_o\sigma d\varepsilon$	dissipated energy
W	potential energy as a result of external loads acting on a elastic body
W_{mn}	known displacement functions used in the solution of a vibrating plate
X	shape of the normal mode of vibration
$X(x)$	displacement function
$Y(y)$	displacement function
ΔL	change in longitudinal deformation
ΔL_T	change in transverse deformation
β_n	a constant with specific values for mode shape n

δD_{11}	uncertainty in the stiffness based on the RSS method
δE	uncertainty in the modulus of elasticity based on the RSS method
ρ	density, or integral of the density through the thickness of the plate
ρ_0	density of the material of the composite
$\rho_0^{(k)}$	density of the k^{th} layer of a composite plate
σ	applied stress
σ_{ij}	applied stress on the SMA crystal
μ_{LT}	Poisson's ratio for the NiTiNOL composite
ε_0	transformational strain
$\Delta\phi$	phase difference between optical fields
$\Delta\phi_t$	phase difference between optical fields of the vibrating object
$\Delta\theta_n$	finite phase step imposed on the reference beam between sequential frames recording individual images
ε	error in the fringe-locus function
ε_f	strain in the fiber
ε_{ij}	incremental macroscopic strain of the SMA crystal
ε_L	longitudinal strain
ε_m	strain in the matrix
ε_T	transverse strain
$\varepsilon_x^{'}$, $\varepsilon_y^{'}$, $\varepsilon_z^{'}$	midplane strains due to the deflection w
Ω	fringe-locus function
Ω_t	fringe-locus function defining fringe loci on the surface of a vibrating object
$\Omega_{t_{approx}}$	approximate fringe-locus function
Π	energy condition for free vibration of rectangular plates
ΔH	latent heat of transformation
ΔV	volume change of the phase transformation
ACES	analytical, computational, and experimental solutions methodology
AMMT	active modal modification technique
ARSME	all-round shape memory effect
ASETM	active strain energy tuning method
BCC	body centered cubic
BCT	body centered tetragonal
B2	atomic structure found in NiTiNOL, where different atom types are found in specific locations
BEM	boundary element method
BR	object beam rotator
BS	beam splitter
CHSLT	Center for Holographic Studies and Laser micro-mechaTronics
CCD	charged coupled device

CNC	computer numerically controlled
CW	continuous wave
DSC	differential scanning calorimetry
EC	environmental chamber
EMOE	effective modulus of elasticity
EOM	equation of motion
FCC	face centered cubic
FDM	finite difference method
FE	finite element
FEM	finite element method
LS	laser
MANSIDE	memory alloys for new seismic isolation and energy dissipation devices
M1 and M2	mirrors
MT	martensitic transformation
NiTiNOL	Nickel Titanium Naval Ordinance Laboratory, most popular SMA
OEH	optoelectronic holography
OWE	one-way effect
PP	pseudoplasticity
PE	pseudoelasticity
PS1 and PS2	phase steppers
PZT	piezoelectric
RSS	root sum square
SEM	scanning electron microscope
SE1 and SE2	spatial filter beam expander assemblies
SFBE	spatial filter beam expander
SI	stroboscopic interferometry, or speckle interferometer
SIM	stress induced martensite
SMA	shape memory alloy
SMABC	shape memory alloy based composites
SME	shape memory effect
SMSL	shape memory strain limit
SOTA	state-of-the-art
SSS	smart structural systems
OEH	optoelectronic holography
TEM	transmission electron microscope
TT	transition temperature
TWSM	two-way shape memory
XRD	X-ray diffraction

1. INTRODUCTION

1.1. General discussion

The thermomechanical behavior of equiatomic NiTi is investigated in this Dissertation. Also representative composites that include NiTiNOL are studied using the ACES methodology (Pryputniewicz, 1997; Mizar et al., 1999; Mizar and Pryputniewicz, 2000, 2003) through which a hybrid, optimal solution will be sought. The variation of modulus of elasticity as a function of temperature is investigated for NiTiNOL and NiTiNOL based representative structures. The effect of repeated thermomechanical cycling on shape memory behavior is evaluated.

The NiTiNOL samples used in this study are shaped as a ribbon, with cross sectional dimensions of 2250 μm by 500 μm. The modulus of elasticity was determined during preliminary phase leading to this Dissertation, from the resonant frequencies for the first through fourth resonant bending modes as measured using optoelectronic holography (OEH). Based on experimental results there exists a difference in temperatures between the forward (Martensite $\rightarrow$Austenite) and the reverse (Austenite $\rightarrow$ Martensite) transformation. This can be attributed to hysteresis which is an indication of absorption of energy.

Increase in modulus occurs as a result of a phase transformation and is one of several ways to quantify the transition. This phase transition is the driving force for the shape memory effect (SME) that results in recovery of plastic strains of up to 8%. During the preliminary measurements, the NiTiNOL samples were heat-treated from 400°C to 500°C for 2.5 hours in order to remove the residual stresses in the

microstructure caused by the forming process (this step was recommended by the manufacturer). After heat treatment the NiTiNOL was subjected to tensile loads on the order of 50 Newtons to 70 Newtons (resulting in tensile stress from 44 MPa to 66 MPa) in order to have a uniform stress distribution. The results obtained from different heat treatment temperatures as well as from the stressed condition after heat treatment were compared. This comparison is essential as SME can be activated by both temperature and stress fields acting independently or in unison.

1.2. Background

The scientific investigation of the SME has been primarily initiated through considerable increase in industrial applications. Computer simulation tools have been developed as a result of constitutive material laws that will eventually reduce design costs. Comprehensive thermomechanical models incorporate the following considerations for optimal simulation of the SME (Trochu, 1996):

1) simulation of three-dimensional stress states,
2) include rubber-like behavior (superelasticity),
3) modeling of hysteresis and subcycles,
4) computational algorithm to simulate response of complex devices that incorporate SMAs,
5) minimal experimental testing to obtain characteristic parameters for the computational models,

6) effect of fatigue on mechanical properties.

From the above considerations it is obvious that the resulting model will be rather complex and sometimes of no practical significance. Therefore, many researchers have formulated material laws taking into account certain aspects and thus simplifying the model in general (Trochu, 1996). Constitutive laws can be based on micromechanical models or on phenomenological models. Micromechanical models are based on a statistical approach while the phenomenological models are based on experimental considerations. The different material laws are also used in FEM simulations of SMA devices. This Section highlights various modeling schemes that have been used by different authors to simulate the phenomenon of SME. The thermomechanical models that follow are based on thermodynamic analysis and are governed by the Clausius-Clayperon equation.

Muller (1986) has proposed an approach for SME based on the thermodynamics of phase transformation and statistical physics. His approach does not clearly define as to why high stresses are required to induce the martensitic transformation at higher temperatures. Falk (1980) has presented a phenomenological model free energy function based on Landau's theory to explain the SME.

The stress induced phase transition exhibits hysteresis, provided thermodynamic barriers exist that prevent an equilibrium phase transition. In practice the phase transition can occur at lower stress levels, where the Gibb's free energy of both phases is equal.

Falk (1980) also attributes characteristic stress-strain response of SMAs to entropy and these alloys can be also called entropy elastic or rubber elastic. He also has developed relations for the Gibbs free energy, G, and relations for temperature induced phase transition. SME is explained based on the scaled free energy versus normalized strain. Experimental verification of the material parameters has also been discussed. This theory is applied only to single crystals and is, therefore, not widely used. Also, the determination of the scaling parameters for the various SMA systems is rather complicated and hence not very practical.

Hoffmann and Sprekles (1987) have developed a model similar to the one developed by Falk (1980), with the difference of using a generalized free energy expression in comparison to an explicit relation used by Falk. A system of differential equations was investigated that results in a one-dimensional model for the dynamics of martensitic phase transitions in SMAs. The stability of the system under distributed heat sources and loads and heat sources at the boundary has also been investigated. This particular approach used loads and heat sources as control variables in order to model both stress and temperature induced phase transition. This model is mathematical and its numerical computations reflect the physics of the martensitic transformation of SMA and its material behavior. Complex mathematical formulations require the use of sophisticated algorithms and this model still awaits experimental verification.

Tanaka (1990) has proposed a theory that consists of a constitutive equation and transformation kinetics to describe thermomechanical behavior of SMAs. The theory when applied in particular to uniaxial stress situations for NiTi to simulate the stress-

strain-temperature relation provides good applicability. The constitutive law is based on the theory of internal variables from continuum mechanics and deals with transformation kinetics, pseudoelasticity, SME, and partial pseudoelasticity. Simulation of recovery stress induced in the partially strained specimen during the heating process revealed an interaction between thermomechanical behavior and phase transformation. Validity of this theory for multiaxial stress situations is still under investigations.

Brinson et al. (1996) have proposed a macro-scale, phenomenological constitutive model for SMAs in conjunction with energy balance equations in order to study evolution of temperature and deformation profiles seen in SMA wires under specific thermal and mechanical boundary conditions. A fully coupled thermomechanical problem was formulated and analytical solutions were sought for the decoupled case and limit cases were investigated. The SME phenomenon is dependent on stress, strain, and temperature. The problem is considered decoupled when either one or two of the three dependent states are either not included or held constant in the analysis. Results for two specific cases are presented: 1) resistive heating of an SMA wire – initial detwinned Martensite leads to strain recovery (contraction) on heating, and 2) deformation wave in a semi-infinite, initially Austenite SMA wire cooled at the boundary – deformation zone propagates and expands as the wire transforms to Martensite (expansion). In both cases, the region and extent of the transformation was identified, indicating the magnitude of actuation obtained. Implications of the modeling for active control of structures are also discussed. The model developed provides accurate results for space-averaged transformation, and hence does not represent nucleation and propagation of the

Martensite transformation of the micro-scale level, but rather the mechanical response. The results still await comparison with experimental data for completion.

Ford and White (1995) have presented thermomechanical behavior of 55Ni45Ti over full range mechanical testing up to failure and over a wide range of temperatures. Thermomechanical properties measured include initial modulus, secondary modulus, critical martensitic start and finish stresses, plastic flow stress, recovery strain limit, failure stress, and plastic modulus. Data are correlated with the Brinson constitutive model. Acceptable correlation between experimental data and Brinson model (Brinson et al., 1996) was reported. The NiTiNOL specimen (wire) was loaded in uniaxial tension to failure and testing was conducted on an MTS-880 test frame. According to Ford and White (1995), the loading was at the rate of 0.1 mm per second with the period of loading being 200 ms. Emphasis of thermal dependence of the initial modulus and critical stress and their effect on SMA sensors and actuator components have also been investigated.

Investigation of binary NiTi by light optical microscopy is difficult, the only successful method is etching using hydrofluoric acid (Lee and Withers, 1978). Successful etching is, however, not guaranteed because of the difficulty in etching through the oxidation layer that is often present on the surface of NiTiNOL. Through optical examination preceded by proper polishing and then followed by etching, the phase transformation, Austenite and Martensite, can be qualitatively analyzed. The preparation of austenitic samples is, however, difficult and etching Martensite using existing etching techniques is rather difficult. Existence of surface relief on the specimens is the only indication of the presence of Martensite in NiTiNOL.

Escher and Huhner (1990) have provided an etching technique suitable for observations of both Martensite and Austenite on optical microscopes. Use of concentrated hydrofluoric acid is avoided and hence is a good advantage of this method, thus giving very little chance for accidental spills of dangerous chemicals (hydrofluoric acid) during the etching process. Samples were cut off and ground on silicon carbide paper with a grit size of 1000, with water as the lubricant. Prepolishing was performed on 6 microns diamond slurry and followed by electrolytic polishing with Strues electrolyte A2 at 20 Volts for 25 seconds. The etchent consisted of the following: distilled water (120 ml), hydrochloric acid (15 ml), sodium disulfite (15g), potassium disulfite (10g), and ammonium hydrogen fluoride (2 g). An optimal etching time of 20 seconds provided acceptable results. Etching on mechanically polished surfaces resulted in poor or no etching due to several deformed layers.

Wick et al. (1995) have investigated the bending behavior of superelastic and shape memory NiTiNOL wire with circular and rectangular cross sections in three-point, four-point, and pure bending configurations. The results from pure bending were in good agreement with results from the four-point bending results. The stress-strain curves for the four-point bending and pure bending were also compared with uniaxial tensile stress results. The tensile data for superelastic beams were analyzed using modified plasticity, and good correlation was obtained with the results from pure bending. The test sample used was a standard NiTi alloy (50.8% Ni), both round and rectangular with a diameter of 1.54 mm for the round cross-section, and 1.33 mm by 1.35 mm for the rectangular cross-section. Influence of heat treatment on the stress-strain curves has also been investigated.

Differences between the upper plateau stress and spring-back strain in between the tensile and bending data in aged conditions were found, with the spring-back strain for all bending samples being greater than that for the samples in tension. This approach is practical and is useful in predicting different types of shape memory effects. Also cross verification between experimental and theoretical predictions has also been presented in a convincing manner.

Baz and Ro (1992) have investigated thermodynamic characteristics of SMA reinforced composite beams. The dynamics of the composite was controlled by heating sets of SMA (NiTiNOL) fibers embedded along the neutral axis of the beam. Activation of SME in the NiTiNOL fibers increased the elastic energy of the entire structure, thus resulting in increased stiffness. Undesirable vibrations can be avoided by fine tuning the vibration modes of the structure and thus preventing the modes from reaching resonance. Emphasis was laid upon the effect of intentional electrical heating of the SMA fibers on the overall dynamics of the composite. Finite element formulations have been utilized to describe interactions between thermal and dynamic characteristics of the composite structure as well as between intentional and unintentional electrical activation of the NiTiNOL fibers. Close agreement was obtained between theoretical and experimental results and the results clearly indicate the possibility of design of NiTiNOL reinforced composite structures and also means of predicting of the performance of such composite structures. Vibration tuning in particular can be useful in critical structures that operate in an autonomous fashion for long duration of time such as satellites, space structures, and defense vehicles as they encounter continuously changing operating conditions.

Baz et al. (1994) have developed a method for controlling the natural frequencies of NiTiNOL reinforced composite beams by activating optimal sets of SMA wires embedded along the neutral axis of the beam. Individual contributions of the fiberglass resin matrix, NiTiNOL wires, and SME, on the overall performance of the composite at different operating conditions were also investigated. The modes of vibrations of the composite with and without the NiTiNOL fibers were measured at various operating conditions. Results indicated that proper NiTiNOL reinforcement resulted in a decreased susceptibility to buckling due to increase in stiffness of the composite structure. Also the modes of vibrations of the activated NiTiNOL reinforced beams could be shifted to a higher frequency relative to those of the un-reinforced beams. A finite element model analysis indicated interaction between NiTiNOL wires and the fiberglass resin matrix. Close agreement was obtained between theoretical and experimental results. Issues concerning behavior of these composite smart structures have been dealt with emphasis on vibration control using SMA reinforcements.

Tobushi et al. (1992) have presented cyclic deformation and fatigue of NiTi wire subjected to rotating bending. Cyclic deformation and fatigue of a NiTi wire was studied under rotating-bending tests at various strain amplitudes, temperatures, and rotational speeds. Results obtained were categorized into two groups based on the phase of the SMA wire. For strain amplitudes in the rhombohedral phase transformation region, the fatigue life was longer than 10^7 cycles and deformation properties (e.g., shape recovery: SME) remained unchanged under cyclic deformation. The fatigue life was found to be shorter than 10^5 cycles for strain amplitudes in the martensitic regions, and also the

fatigue life decreased with an increase in temperature. The material used for the tests was a Ti-55.3 % by weight Ni SMA wire, with a diameter of 0.75 mm. The rotational speed was found to be of no effect on the fatigue life when the experiments were conducted in a water medium.

Hissaki et al. (1996) have presented experimental results on cyclic deformation properties of TiNi shape memory alloys under thermomechanical loading. Experimental investigations were carried out on thermomechanical properties of SME as a result of thermomechanical loading. The transformation stresses, the transformation line, and fatigue properties as a result of phase transformation have been investigated. For high cycle deformations, the R-phase transformation was most suitable. The material used in this particular study was a Ti-55.3wt % Ni SMA wire, 0.75 mm in diameter. Shape memory training was achieved for the samples by constraining at the desired shape at 400°C for 1 hour and followed by cooling in a furnace. The testing apparatus constituted a tensile tester and a heating-cooling device. The single specimen was heated by hot air and cooled by liquefied carbon dioxide. A rotating-bending machine was used for the fatigue testing. Experimentation tests for SME, superelasticity, and for fatigue life were conducted. From results obtained the following conclusions were drawn:

1) the martensitic transformation (MT) reverse transformation temperature increased with a corresponding decrease in the MT stress,
2) the variation in thermomechanical properties as a result of the R-phase transition was minimal,

3) the importance of including behavior of transformation lines under cyclic deformations,

4) the rotating-bending fatigue life of the wire is quite long in the R-phase transition region.

Tanaka (1986) presented a unified one-dimensional theory for materials that undergo thermoelastic MT. The thermomechanical constitutive equations for the transformation kinetics have also been derived. The theory was then applied to a one-dimensional tensile situation to describe superelasticity, ferroelasticity, and SME. The author has discussed the kinetics and transformation based on a thermomechanical approach. The material is considered to be a poly-crystal so that nucleation and growth of the martensitic plates can be understood as being governed by macroscopic transformations. The theory indicates that the Helmholtz free energy and the dissipation potential result in a series of equations: the thermomechanical constitutive equations and the equation that governs the transformation phenomenology. The stress-strain curves in tension are estimated by the theory for a simple model in order to explain the superelasticity, pseudoelasticity, ferroelasticity, and shape memory effect. The theory presented by Tanaka (1986), based on mathematical formulations, can be used in the verification of experimental results.

Pruski and Kihl (1992) have investigated the classical hysteretic behavior exhibited by NiTiNOL. In order to make strain control possible, the internal electrical resistance variation is used as the feedback variable. Copper-based shape memory alloys were investigated for which strain has the disadvantage of having a large hysteresis. The

paper discusses methods for removing hysteresis and some cases where controlled SMA behavior may be used. In most applications involving SMAs, electrical resistance is primarily present, and as a result of which, hysteresis is inevitable. Also the resistance of the two phases (Martensite and Austenite) is different and it is not always possible to determine strain from reading stress or temperature. This particular aspect constitutes the framework for this investigation. The study is focused on the materials electrical resistance in order to improve the accuracy of an internal feedback-controlled SMA actuator. Cu-Zn-Al SMA was used in this study and the authors state that this particular SMA has a lower performance than NiTiNOL pertaining to allowable shape memory stress and strain and also has a greater hysteretic behavior. Based on the results obtained the authors conclude that the hysteretic pattern (behavior) of a SMA is required for proper sensor/actuator design. As the hysteresis magnitude is known, it is then possible to add or subtract a constant value to the feed back information according to the variation of the reference. The authors suggest that results can be duplicated for the NiTi SMA system.

Boyd and Lagoudas (1995) have proposed a mathematical microthermodynamic analysis of SME in composite materials. The paper addresses SME and pseudoelasticity as a result of the phase transformation in SMA composites. The simulation is performed in two stages or procedures. First, phenomenological constitutive equations are proposed for the monolithic polycrystalline SMA material. A convex free energy function coupled with dissipation potential is used to generate a response of the generalized standard material. Second, a micromechanics analysis of a SMA composite material is performed

to derive its free energy, transformation strain rate, and the Clausius-Clayperon equation. Results for a NiTiNOL SMA fiber / elastomer matrix composite are presented.

Hornbogen and Kobus (1993) have presented a method for the characterization of SMAs by hardness indents. An indenter is harder than the material to be tested and as the indenter tip is pressed into the material the material deforms plastically at the indented zone and hence work hardens. For SMA the same is valid, but the only difference being that when the indent will partly or completely disappear as the temperature is increased. The test began when the SMA was in the martensitic condition (20°C) and with the formation of Austenite the hardness value was found to decrease with the lowest value at the end of complete austenitization. On subsequent cooling, Martensite started to form with a corresponding increase in the hardness value. Cooling of the SMA sample was achieved through the use of liquid nitrogen. Experiments were conducted on shape memory steel, then for a copper-based SMA, and they both exhibited similar transformation characteristics. One striking difference being in the fact that for the copper-based SMA, the Austenite was harder than Martensite. In addition, the path of change in hardness did not correspond with the calorimetrically measured path of the transformation. It was found that for the copper-based SMA the Martensite retained its low hardness until, in the stress free transformed condition, the re-transformation into the parent phase (Austenite) was complete. Similar measurements carried out on NiTi indicated that Martensite was soft and Austenite hard. The Martensite however showed an increase in hardness with increasing temperature, and a significant increase in hardness occurred before the re-transformation took place. The higher hardness value

remained unchanged until Martensite began to form. Over repeated cycles, the Martensite was found to get softer with each cycle and got even softer at temperatures lower than the room temperature. The hardness indentation yielded information regarding the phase transformation, transformation temperatures as well as pseudoelasticity, stress and strain induced transformation in the martensitic phase, pseudo-plasticity of the Martensite and true plasticity. The characterization of these unique behaviors can be obtained from an analysis of the shape and dimension indentation. This is a very useful technique to determine critical parameters like the transformation temperatures as well as allowable deformation and stress levels.

2. MARTENSITE AND SHAPE MEMORY EFFECT

2.1. Introduction

Shape memory refers to the ability of certain materials to "remember" a shape, even after extensive deformations. Once deformed in the low temperature phase (Martensite), these materials will stay deformed until heated, upon which they spontaneously return to their original, pre-deformation shape. This phenomenon is called shape memory effect (SME). The basis for SME is that materials can easily transform to and from Martensite. Even the elementary engineering aspects of SME cannot be understood without first familiarizing oneself with some basic principles of Martensite and its formation.

2.2. A microscopic perspective of Martensite

Solid state transformations are usually of two types: diffusional and displacive. Diffusional transformations are those in which the new phase can only be formed by moving atoms randomly over relatively long distances. This requires long range diffusion as the new phase that is formed is of a different chemical composition than the matrix from which it is formed. Since this type of a transformation requires atomic migration, the diffusional transformation is dependent upon both time and temperature. Displacive transformations, on the other hand, do not require, large atomic migration; in this case the atoms are rearranged into a new, more stable atomic structure in a cooperative fashion. This rearranging is done without changing the chemical nature of

the matrix. Since no atomic migration is involved, these displacive transformations progress in a time independent fashion, with the motion of the surface between the two phases being limited by only the speed of sound. These transformations are also referred to as *athermal* transformations. martensitic transformations are of the displacive type, and are formed upon cooling from a higher temperature phase called the parent phase, or Austenite. It is important to note that a precise definition for Martensite has never been agreed upon. The terms "Martensite" and "Austenite" were used to refer to phases of steel. However a more generalized definition for Martensite is based on the product of the phase transformation rather than a particular material is now more widely accepted.

Martensitic transformations are first order transformations. This means that heat is liberated when Martensite is formed. There is a hysteresis associated with the transformation and there is a temperature range over which Martensite and Austenite co-exist. Therefore it is possible to state that Martensite is formed upon cooling with the volume fraction of Martensite increasing as the temperature is reduced. It is important to note that the volume fraction is independent of time and is dependent solely on temperature.

In a crystallographic context, the phase transformation from Austenite to Martensite is thought of to occur in two parts: the *Bain strain* and the *lattice invariant shear*. These mechanisms in a crystallographic sense are quite complex. However, it is possible to explain them adequately in a quite simple fashion using a two-dimensional approach. The Bain strain, also referred to as lattice deformation, consists of all atomic movements that are needed to form the new structure (i.e., phase) from the old. Figure

2.1 illustrates the austenitic structure schematically in diagram (a), and the progression of the transformation to a fully martensitic structure is schematically illustrated by (b) through (d). It is important to note that the interface progresses through each atomic layer, each atom is required to move by only a very small amount (Fig. 2.1c). The end result of all these coordinated movements is the new martensitic structure. The movements that are required to produce the new structure are called Bain strain. In real materials, Bain strain generally consists of several atomic shuffles in addition to the movement illustrated in Fig. 2.1.

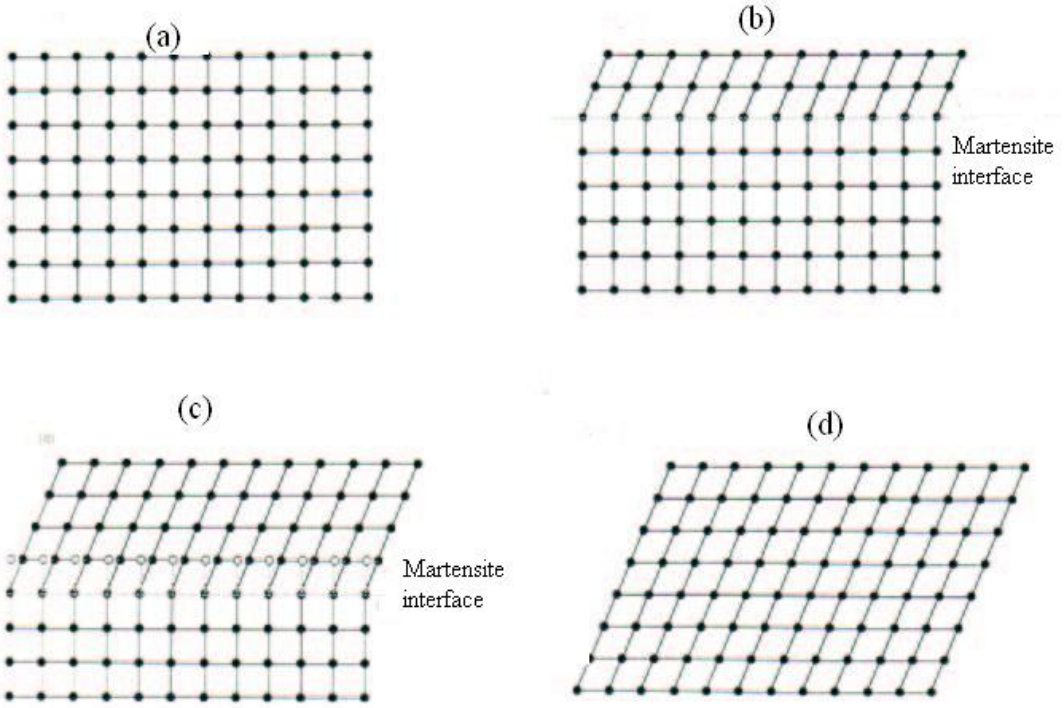

Fig. 2.1. Transformation from Austenite to Martensite in two-dimensions
(a) being completely austenitic and (d) being completely martensitic
(c) the interface advances, each layer of atoms is displaced only by a small distance.

The second part of a martensitic transformation is referred to as the *lattice invariant shear*. It is an accommodation step: the martensitic structure produced by the Bain strain is of a different shape, and often volume, than the surrounding Austenite (Figs 2.1a and 2.1d). Martensite in steel however involves both a volume change and a shape change, whereas shape memory alloys like NiTiNOL undergo only a shape change. Either the overall shape of the new phase, or the surrounding Austenite must be altered to accommodate the new structure. There are two mechanisms by which this is possible: slip (Fig. 2.2a) and twinning (Fig. 2.2b). In both cases, each individual cell, or parallelogram, has the new martensitic structure, but the overall shape is that of the original Austenite. Slip is a permanent process and is a common accommodation mechanism in many Martensites. Twinning is unable to accommodate volume changes, but can accommodate shape changes in a reversible way. For shape memory to occur to any significant extent, it is required that the accommodation be fully reversible or, stated alternately, that twinning be the dominant accommodation process. In Fig. 2.2, only two directions or variants of shear are required to restore the original, overall shape of the matrix; in three-dimensions the situation can be complicated: Cu-Zn-Al Martensites for example, require four Martensite variants for full, three-dimensional accommodation, and Ni-Ti Martensites require three.

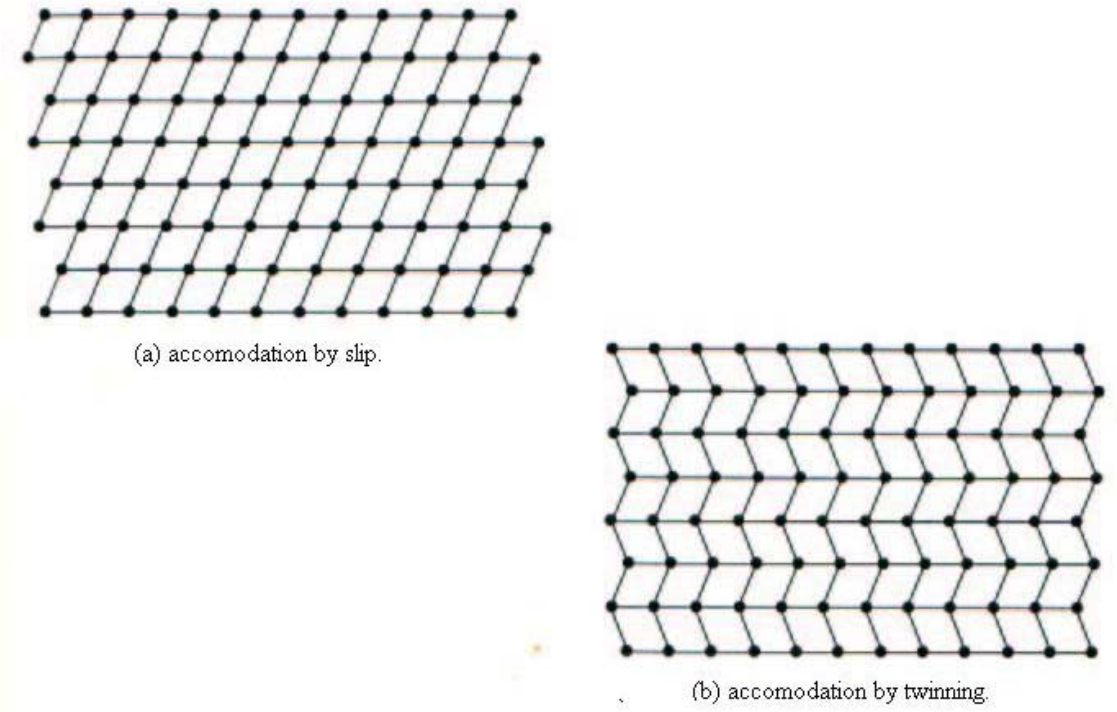

Fig. 2.2. Two mechanisms of accommodating the shape change due to the atomic shear of a martensitic transformation.

The twinning process of accommodation plays a key role in the shape memory effect and should be reviewed in more detail. As can be seen in Fig. 2.3, the twin boundary is a mirror plane: when positioned on the boundary, the view in one direction is a mirror image of the other. Atoms situated on that boundary see the same number and type of bonds in both directions. Some key properties of twin boundaries are that they are of a very low energy and they are quite mobile; thus the relative stability of a martensitic phase is not strongly affected by the number or location of these boundaries. By comparing edges of the structures shown in Figs 2a and 2b, one can see that slip accommodation requires that atomic bonds be broken, while all bonds remain intact in

the twinned structure. If a stress is applied to the structure shown in Fig. 2b, the twin boundaries will easily move, producing a shape that better accommodates the applied stress. The result of moving a twin boundary is to convert one orientation or twin variant into another. That variant will be chosen which is most favorably oriented to the applied stress. In the ideal case, a single variant of Martensite can be produced by straining a sufficient amount. This process of condensation of many twin variants into a single favored variant is called detwinning. In the foregoing discussion, only the twins within individual martensitic plates have been considered. However crystallographic analysis has shown that the boundaries between martensitic plates also behave as twin boundaries – i.e., the individual plates of Martensite themselves are twins with respect to adjoining plates. Therefore the term twin boundaries refers to the boundaries between Martensite plates as well as the boundaries within plates.

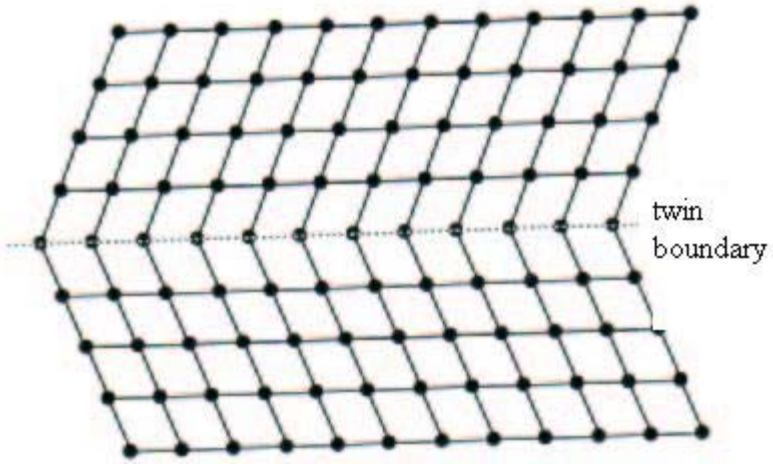

Fig. 2.3. Schematic view of a twin boundary.

In Figs 2.1 through 2.4, the atom types have not been identified. In an alloy, however, there exist several species of atoms. It is therefore important to identify the lattice site locations of these atoms. In steel, for example, these atoms are disordered, meaning that different elements are randomly distributed on the lattice sites. In NiTiNOL, however, the atoms are ordered, meaning that the Ni and Ti atoms are found on very specific sites (Fig. 2.4). During the course of a martensitic transformation, the Martensite takes on the same ordering as the Austenite. This is referred to as inherited ordering. Shape memory alloys are generally based on a BCC symmetry, some with the BCC structure, more often with the B2 structure, and some with an even more complex ordering called DO_3, still based on the BCC symmetry.

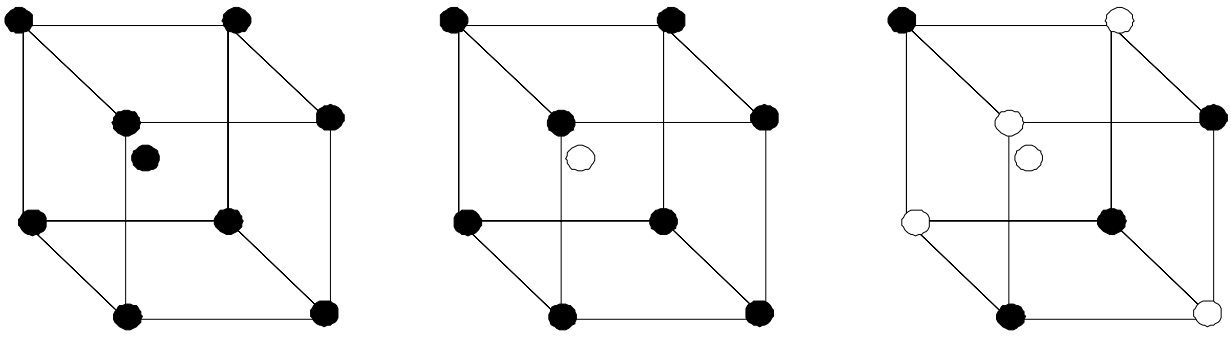

Fig. 2.4. Ordered and disordered structures commonly found in shape memory alloys: (a) disordered BCC structure, where different atom types are randomly distributed, (b) B2 structure, found mostly in NiTiNOL, where different atom types are found in specific locations, (c) higher order phase than (b) called DO_3 state found, for example, in Cu-Al-Ni alloys.

Martensite normally appears as plates, resting on complex crystallographic planes known as habit planes. In many shape memory alloys, the Martensite plates are easily

viewed through an optical microscope. NiTiNOL however exhibits fine plates that cannot be examined through an optical microscope. It is therefore important to prepare samples for NiTiNOL very carefully, since normal grinding and polishing can sometimes disturb the Martensite, or sometimes may even produce Martensite that did not exist to begin with.

2.3. A macroscopic perspective of Martensite

The physical properties of Austenite and Martensite are different. Therefore as the phase transformation progresses and the transformation point is passed, a variety of property changes occur. Any of these property changes can be used to follow the progression of the phase transformation. There are four significant temperatures that characterize the transformation from Martensite to Austenite and vice versa. Four temperatures indicated by M_s, M_f, A_s, and A_f (Fig. 2.5) refer to temperatures at which the transformation to Martensite starts and finishes, and the temperatures at which the reversion to Austenite starts and finishes, respectively. There is a hysteresis associated with this phase transformation (martensitic transformation). Stated alternatively, the transformation temperatures differ upon heating and cooling during the martensitic transformation. The magnitude of the hysteresis varies from one alloy system to another, and has typical values ranging from 20ºC to 40ºC. Microscopically, hysteresis can be attributed to friction associated with the movement of twin-related Martensite boundaries.

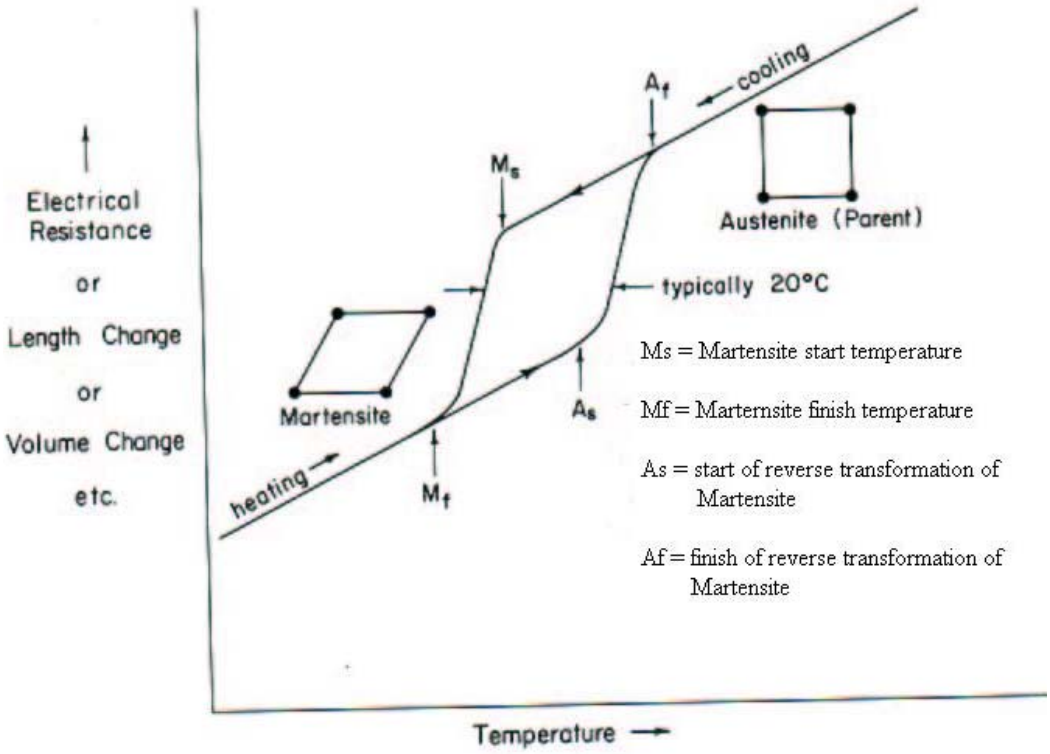

Fig. 2.5. Hypothetical plot of property change versus temperature for a martensitic transformation occurring in a SMA.

One of the many mechanical properties that change during the phase transformation is the yield strength. The martensitic structure deforms by moving twin boundaries. These twin boundaries are quite mobile. Martensite therefore has low yield strength. Austenite, on the other hand, deforms by dislocation generation and movement. Only a certain amount of Martensite can deform based on this twin movement process and once this limit is exceeded, the material will again deform elastically and eventually yield the second time by an irreversible process (movement of dislocations). The resulting unusual tensile behavior is indicated in Fig. 2.6. In Fig. 2.6, the plateau refers to

the thermal hysteresis, which means that both Martensite and Austenite are controlled by the frictional stress of the twin boundaries. It is the yield strength ratio between the Martensite and Austenite that controls the ratio of resistances to reversible and irreversible deformations (twin movement to slip). In shape memory alloys, it is important to have this ratio as high as possible in order to recover the most amount of the deformation. Typical values of these ratios are 0.1 to 0.2 (Duerig, 1990).

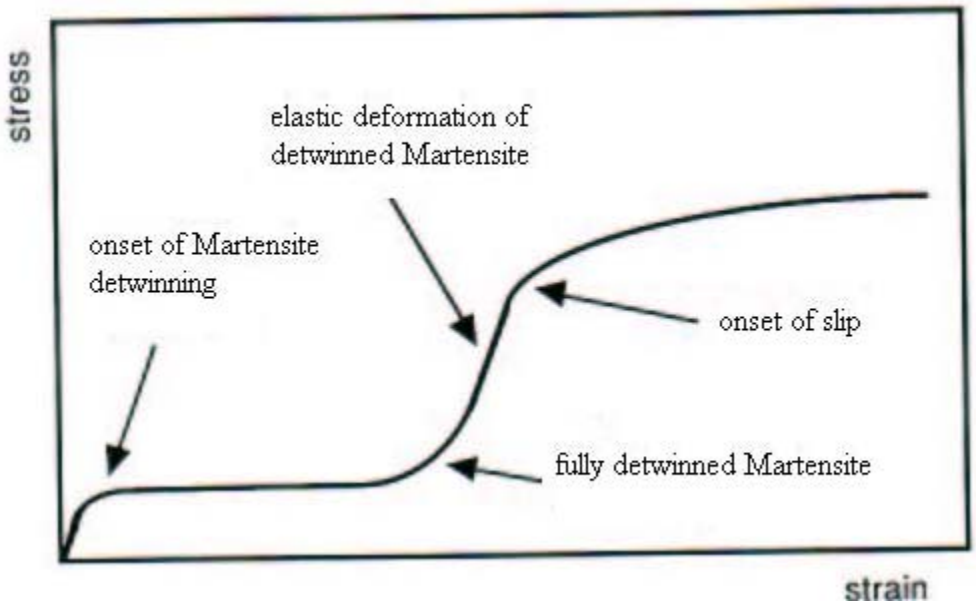

Fig. 2.6. Typical stress-strain curve for a twinned martensitic material.

2.4.The origin of shape memory effect

Martensite is generally of a lower symmetry phase than Austenite. Therefore there are several ways by which Martensite can be formed out of Austenite. However there is only one route by which the Martensite formed will revert back to Austenite.

Shape memory effect can be explained in a very simple manner by a 2D geometrical concept depicted in Fig. 2.7 (Duerig, 1990). Upon cooling from Austenite (Fig. 2.7a), the self-accommodating variants of Martensite (Fig. 2.7b) are formed. During the application of stress (deformation), the twin boundaries migrate and therefore result in a biased distribution of Martensite variants (Fig. 2.7c). It is however important to note that no matter what the distribution of Martensite is, there is only one possible austenitic structure that these variants can revert back to. Therefore the martensitic variants must return back to the original undeformed shape after reverting back to Austenite. Therefore the shape accommodation due to a twin boundary movement can only be supported by a low symmetrical martensitic structure, and when the more symmetric Austenite structure is returned, the twinning deformation must also disappear.

The shape memory effect can be described with reference to the cooling and heating curves, Fig. 2.8. There is no change in the shape of the specimen cooled from above A_f to below M_f. When the specimen is deformed below M_f it remains so deformed until it is heated. The shape recovery begins at A_s and is completed at A_f. At the inflection point, between A_s and A_f, about 50% of the original shape is recovered.

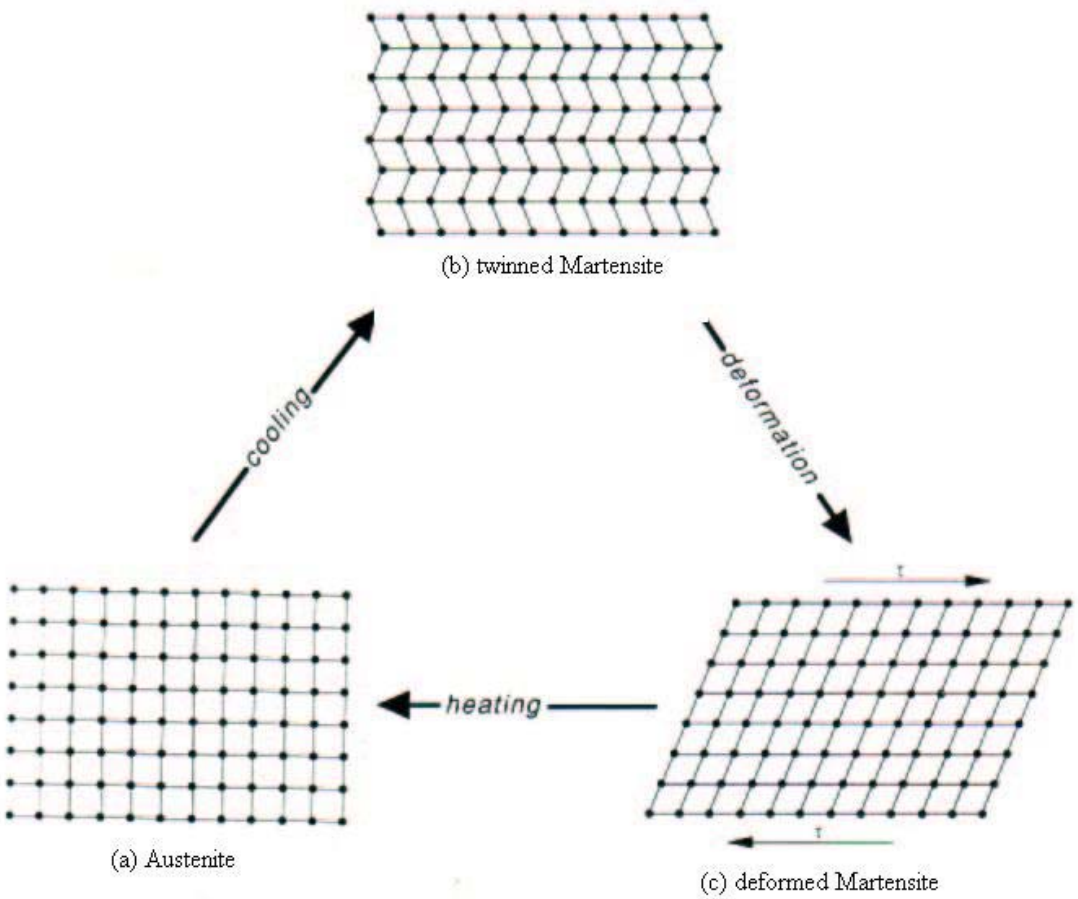

Fig. 2.7. Shape memory shown microscopically: Austenite (a) is cooled to form twinned Martensite (b) without undergoing a shape change, then is deformed by moving twin boundaries (c). Heating either state (b) or (c) will return the originally austenitic structure and shape.

Once the shape has recovered at A_f there is no change in shape when the specimen is cooled to below M_f and the shape memory can be reactivated only by deforming the martensitic specimen again. In other words, the shape memory effect is a one time only occurrence and therefore it is frequently referred to as the one-way shape memory effect. Typical recoverable strains for most SMAs are about 7%, while some of them can

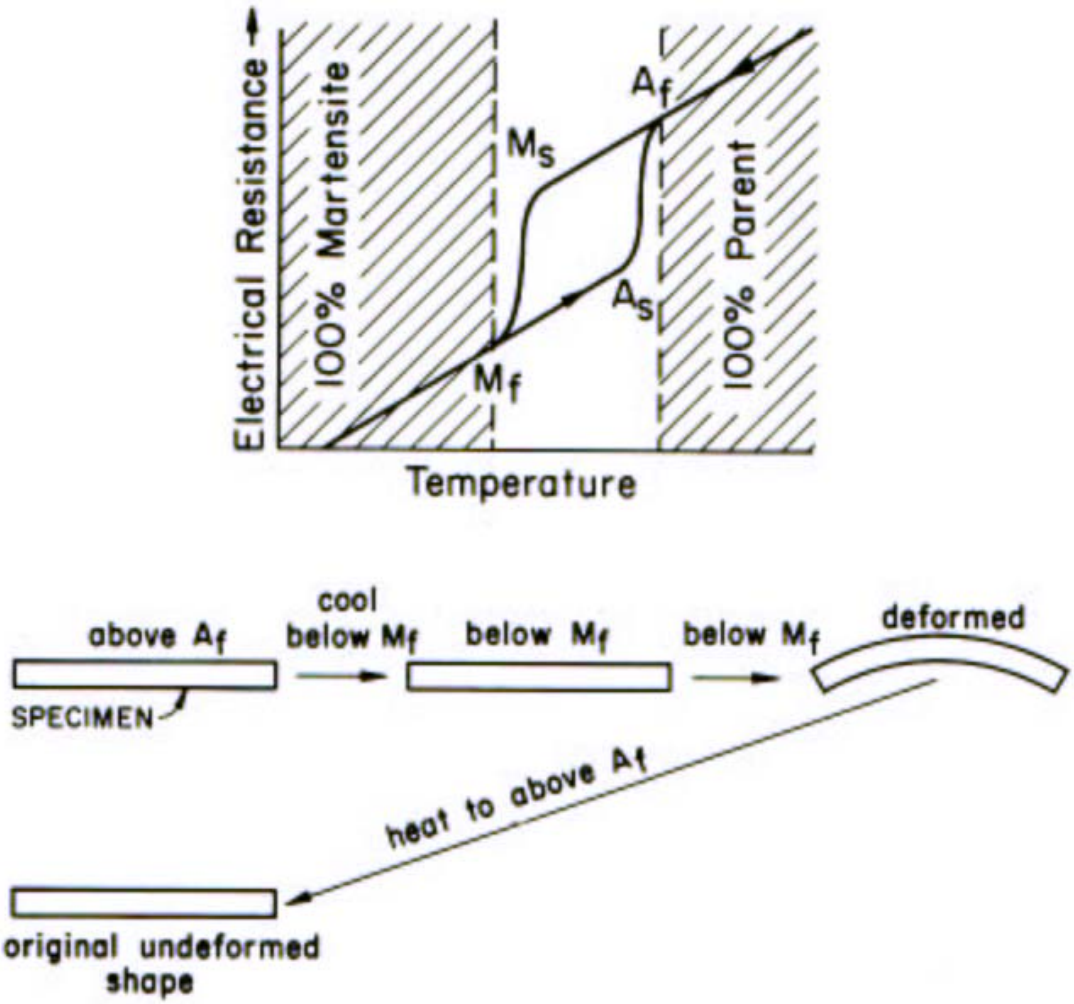

Fig. 2.8. The shape memory effect as described with reference to a plot of electrical resistance versus temperature.

recover strains up to 10%. Among the many alloys that exhibit SME, only the Cu-Zn-Al, Cu-Zn-Ni, and Ti-Ni alloys are presently of commercial importance.

2.5. Stress-induced Martensite and Superelasticity

So far shape memory effect has been considered to be both thermal and mechanical. The Martensite is initially formed during cooling and is then deformed below the M_f temperature, and then heated to above the A_f temperature to cause the shape to recover. This means that shape memory is caused by heating. There is also another type of shape memory that is dependent upon temperature, which is referred to as superelasticity. It is a known fact that the formation of Martensite is a thermoelastic process, which means that a decrease in temperature between M_s and M_f results in a slight growth of existing martensitic plates and the nucleation of new ones. However when the temperature is incrementally raised the newly nucleated plates disappear and those which grew slightly on incremental cooling correspondingly shrink back a little. Stated alternately, there is equivalence between temperature and stress: a decrease in temperature is equivalent to an increase in stress, and these both stabilize Martensite. The Martensite is also crystallographically reversible, which means that the reversion of a given plate upon heating is just the reverse of the formation process, i.e., the plates undergo a backward shear as it disappears. Normally, on cooling, the Martensite forms under M_s if a stress is applied and the so-formed Martensite is called as stress-induced Martensite (SIM). The driving force for the transformation is, in this case, mechanical rather than thermal. Above M_s the stress required to produce SIM increases with increasing temperature, as shown in Fig. 2.9.

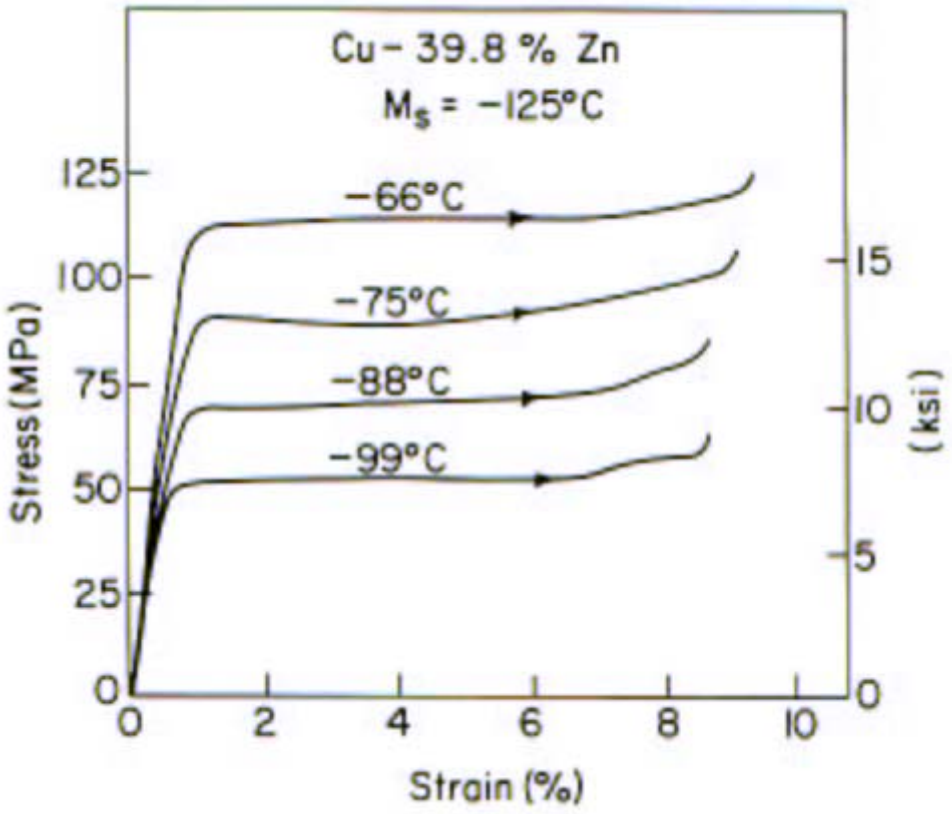

Fig. 2.9. Stress-strain curves for Cu-Zn single crystal loaded in tension above M_s.

The variation in stress required to produce SIM increases linearly with temperature above M_s, Fig. 2.10. Figure 2.10 shows that the extrapolated stress drops to zero at the temperature M_s. The linear variation of stress to induce Martensite as a function of temperature obeys the Clausius-Clayperon equation, and is written as

$$\frac{dP}{dT} = \frac{\Delta H}{T\Delta V} \quad , \tag{2.1}$$

where P is the pressure, T is the temperature, and ΔH is the transformation latent heat and ΔV is the volume change of the phase transformation. Equation 2.1 has been traditionally

used by chemists (Duerig, 1990), but metallurgists, on the other hand, use the Clausius-Clayperon in the following form:

$$\frac{d\sigma}{dM_s} = -\frac{\Delta H}{T\varepsilon_0} \quad , \tag{2.2}$$

where ΔH and T have the same interpretation as for Equation 2.1, and σ, M_s, and ε_0 are the applied stress, the shifted M_s temperature and the transformational strain resolved along the direction of the applied stress. The difficulty to stress induce Martensite continues to increase with temperature until M_d, above which the critical stress required to induce Martensite is greater than the stress required to move the dislocations. Therefore the temperature range for SIM is from M_s to M_d. For a number of SMA systems, the agreement in the temperature dependence of the stress to form SIM according to the Clausius-Clayperon equation is quite striking. The equation works equally well for the non-isothermal case, i.e., the case where temperature was held constant while the stress needed to form Martensite was measured.

Superelasticity occurs when a material is deformed above A_s, but still below M_d. In this range, Martensite can be made stable with the application of stress, but becomes unstable upon removal of stress. Figure 2.11 shows a superelastic stress-strain curve for a Cu-39.8%Zn SMA. The upper plateau corresponds to the formation of Martensite under stress whereas the lower plateau represents SIM when the load is released (Duerig, 1990). Note that 9% strain is fully recovered during unloading, and can be viewed as a mechanical shape memory effect. When the SIM is formed for a single crystal Cu-Zn shape memory alloy only a single variant is formed during the application of stress. This

results in an elongation (or shape change) which is fully recovered upon release of the applied stress. This situation is unlike the case of thermal Martensite, there is no overall net shape change accompanying the formation of various variants of Martensite.

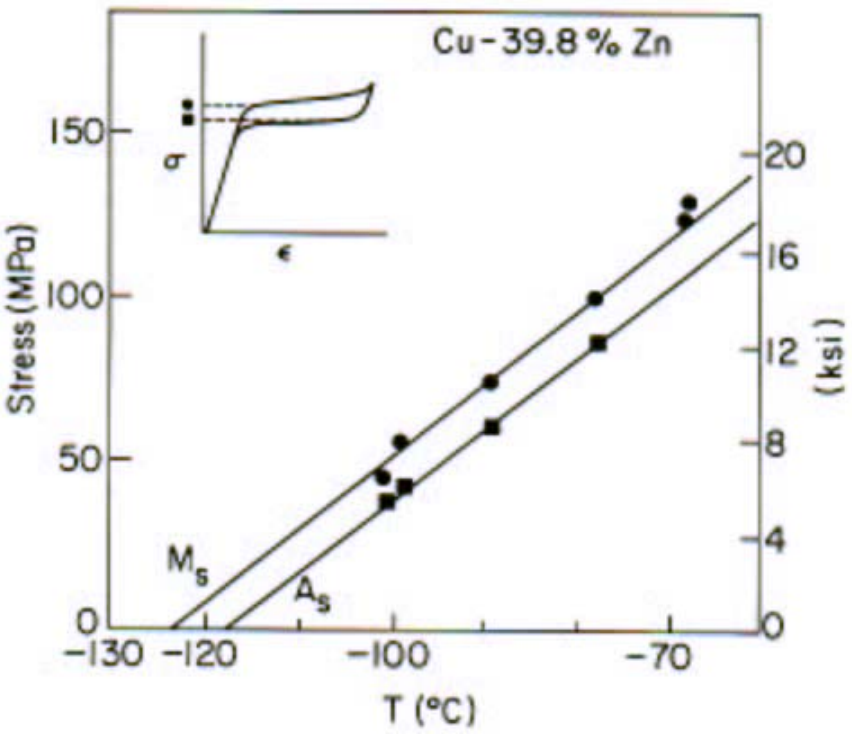

Fig. 2.10. Stress plateau as a function of temperature.

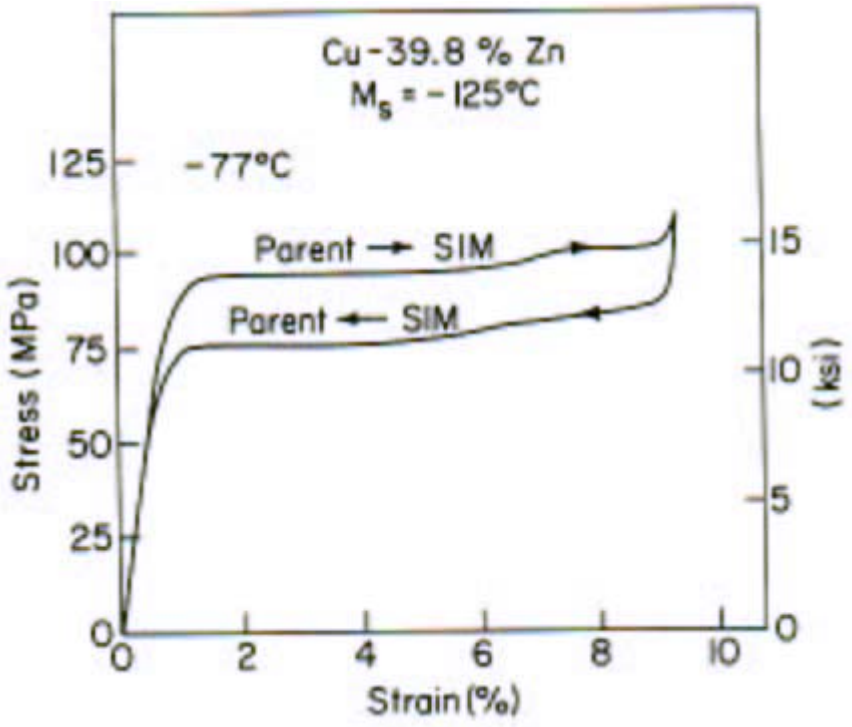

Fig. 2.11. Stress-strain curve for a Cu-Zn shape memory alloy, loaded above the A_s temperature and then unloaded, shows superelastic behavior.

2.6. Mathematical background for martensitic transformation

Experimental evidence from optical, SEM (Scanning Electron Microscope), and TEM (Transmission Electron Microscope) observations indicate that during a MT, a line and surface is converted to another line and surface. This conversion can be represented mathematically by a matrix operator. The parent (Austenite) and martensitic phases are of different microstructures. A coordinate transformation must be performed to mathematically explain the MT. Linear algebra is used to perform such a transformation. During a coordinate transformation, the mathematical operator will itself undergo a transformation.

Application of a coordinate transformation to a vector results in the transformation of the mathematical operator based on a similarity transformation. Wayman and Duerig (1990) have discussed the mathematics of the similarity transformation.

A martensitic crystal is formed from the parent phase through a diffusionless transformation. This type of a transformation is well explained for the FCC to BCT (Base Centered Tetragonal) transformation in steels, Fig. 2.12. Generally a FCC twin has a BCT lattice with an axial ratio of 1.414. Martensite in general has a ratio close to one. This is possible when the Z axis is contracted and X and Y axes are elongated, according to the mechanism first proposed by Bain. Even though the mechanism differs for different type of SMA systems. A Martensite can always be created from a parent phase by a combination of elongation, contraction and shear along certain directions (Otsuka, 1998). Since MT is a diffusionless transformation, there exists a one-to-one relation between the parent and the martensitic phase.

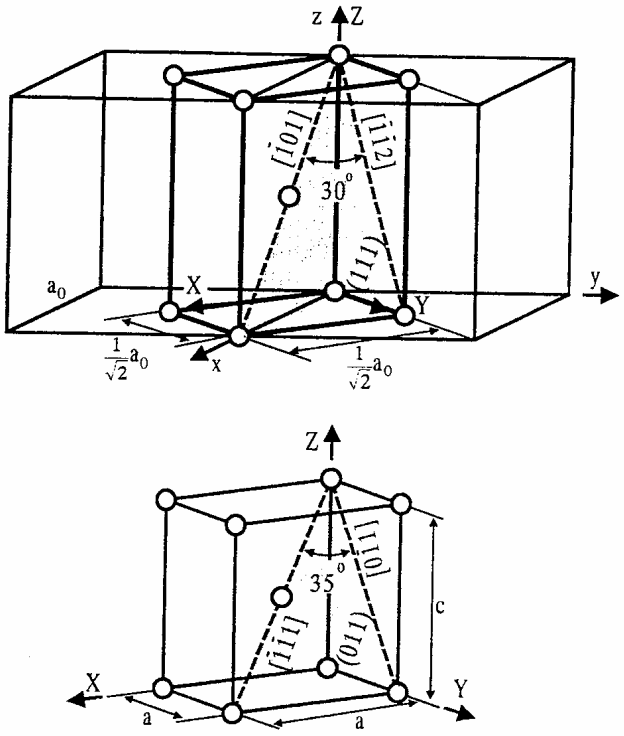

Fig. 2.12. Mechanism of FCC-BCT (or BCC) transformation Bain strain. *xyz* represent the crystal axes in the parent FCC lattice, while XYZ represent the axes in the BCT Martensite.

2.7. Phenomenological theory of the martensitic transformation

The crystallographic characteristics of the martensitic transformation are well understood by the phenomenological crystallographic theory. The theory requires that the MT consists of the following components:

1) a lattice deformation *B*, as a result of the formation of Martensite from the parent phase,
2) lattice invariant shear P_2 (as a result of twinning, slip, or faulting),
3) a lattice rotation *R*.

Theory requires that the shape memory strain produced by the MT consists of a lattice invariant strain and is homogeneous macroscopically. It consists of a shear strain parallel to the habit plane and an expansion or contraction normal to the habit plane. The shape memory strain can also be represented as follows (Wayman and Duerig, 1990):

The crystallographic theory has been so far successfully applied to Au-Cd, Fe-Pt, Fe-Ni-C and Fe-Al-C alloys with a good correlation between experimental and theoretical results. The theory when applied to other SMA systems, does not provide overall agreement between experiment and theory.

2.8. Thermodynamic aspects of the martensitic transformation

The MT can be explained based on a thermodynamic analysis, as it is driven either by stress or temperature. There is heat interaction between the SMA specimen and the surroundings and specific temperatures characterize the phase transition. Even though these temperatures can be determined by the DSC (Differential Scanning Calorimetry) methods, a thermodynamic analysis will provide an insight into characteristics unique to SME like hysteresis, superelasticity, one-way effect, rubber-elasticity, and two-way effect.

A gas can be liquefied by the application of a suitable pressure. Similarly, a phase transition from the parent phase to Martensite can be induced by the application of a stress. A thermodynamic analysis explains thermal and mechanical effects on the SME. Thermodynamics is a good tool to perform calculations on the thermal implications of the

stress induced phase transition. It also explains the reversibility of the phase transition in certain SMAs and highlights energy contributions that control the hysteresis phenomenon (Trochu,1996).

Gibbs theory of thermodynamic stability is used to describe the phase transition under the consideration that the alloy system is in equilibrium. Based on the above consideration it is evident that Gibbs theory is not suitable for systems not in equilibrium, for which fluctuations are amplified to generate new structures. An MT can be considered to be a succession of several equilibrium states and Gibbs approach based on free energy can be used. The thermodynamic analysis is based on work and methodology presented in the work on SMAs by Trochu (1996).

The MT is a solid state transformation and a thermodynamic analysis, based on internal variables such as the latent heat of the phase transformation, enthalpy, and entropy for a single crystal of SMA, is presented in this Section. Derivation of the classical Clausius-Clayperon equation that relates stress and temperature is also presented. The analysis is conducted for a single crystal of SMA, because this facilitates the investigation of the SMA specimen as a thermodynamic system with only one component.

2.8.1. Thermally induced phase transformation

In this particular case, the martensitic phase transformation is thermally induced. The SMA crystal has energy interactions with its surroundings in the form of heat and

work and this can result in an increase, or decrease, in the internal energy. The change in internal energy undergoing a heat transfer with its surroundings, or doing useful work, can be written in thermodynamic terms as follows:

$$dE = dQ + dW \quad , \tag{2.3}$$

where E is the internal energy, dQ is the heat exchange between the SMA crystal and its surroundings, and dW is the work accomplished as a result of dQ.

Assuming the phase transformation as a reversible heat transfer situation and using the second law of thermodynamics the following relation is obvious and valid:

$$dQ = TdS \quad , \tag{2.4}$$

where T is the temperature and dS is the change in entropy of the SMA crystal. According to thermodynamic convention, work done by a system is positive and energy transfer into the system is also positive. Keeping this in consideration and also from the assumption that that work done by the crystal is a hydrostatic work, an expression for the work done can be written as

$$dW = -pdV \quad , \tag{2.5}$$

where p is the pressure and dV is the change in volume.

From Eqs 2.4 and 2.5,

$$dE = TdS - pdV \quad . \tag{2.6}$$

All properties that are used in the thermodynamic analysis are extensive and refer to per unit mass basis of the SMA crystal. As E, S, and V are difficult to control during experimentation, additional thermodynamic potentials in the form of enthalpy H and the

Gibbs free energy G have to be introduced. They can be defined in terms of E, S, T and V as follows (Trochu, 1996):

$$H = E + pV \quad , \tag{2.7}$$

and

$$G = H - TS \quad . \tag{2.8}$$

Differentiating Eqs 2.7 and 2.8, and rearranging the results for dE and dG we have

$$dH = TdS + Vdp \quad , \tag{2.9}$$

$$dG = Vdp - SdT \quad . \tag{2.10}$$

The entropy S and the pressure p are natural variables that appear in the expression for the increment of enthalpy dH. At constant pressure, dH corresponds to the amount of heat transferred between the crystal and the surroundings. The temperature T and pressure p constitute natural variables in the expression for dG. These natural variables are easier to control during experimental procedures and hence are very useful in thermodynamic analyses of the phase transformation. Thermodynamic equilibrium is achieved when $dG = 0$. If the temperature T is altered at constant pressure, then a plot of the Gibbs free energy as a function of temperature T can be constructed and can be represented schematically, Fig. 2.13.

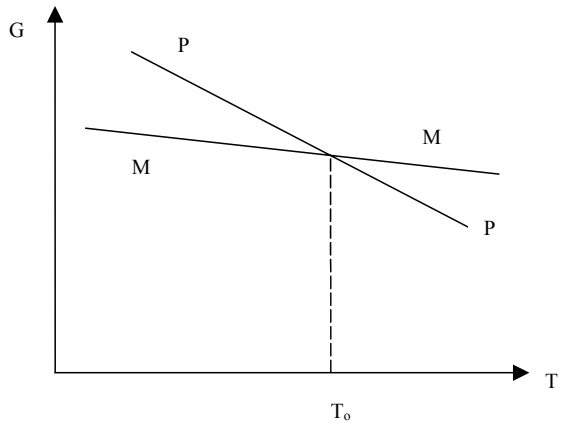

Fig. 2.13. Evolution of free energies for the parent and the martensitic phases at constant stress.

The slope of $G^P(T,p)$ represents the entropy of the parent phase and is a function of temperature. For small intervals of the temperature T, G^P can be considered to be a constant and the following relation between the enthalpy, temperature T, and entropy S can be written

$$G^P = H^P - TS^P \quad . \tag{2.11}$$

Similarly, an expression for the martensitic phase can also be written and is of the form:

$$G^M = H^M - TS^M \quad . \tag{2.12}$$

From Fig. 2.12 it can be noted that at a particular temperature $T=T_o$, phase transition from the parent phase to Martensite as well as the reverse transformation are possible without any hindrance. Also, at $T<T_o$, Martensite is stable and at temperatures $T>T_o$ Austenite is stable. Hence T_o is also called as the transition temperature and can be determined from the Gibbs free energies of the two phases. The expression for the transition temperature can be written as

$$T_o = \frac{\Delta H}{\Delta S} = \frac{H^P - H^M}{S^P - S^M} \quad . \tag{2.13}$$

In this particular analysis if the interaction between the two phases is to be taken into account, then an additional variable is to be considered. This variable, f_M, is the fraction of Martensite that has been transformed into Austenite. The entropy, S, in such a situation is given by the expression (Trochu, 1996)

$$S = (1 - f)S^P + fS^M \quad . \tag{2.14}$$

On multiplying Eq. 2.14 by Eq. 2.13 and differentiating the result with respect to *S*, we obtain

$$T_o dS = T_o (S^M - S^P) df = dQ \quad , \tag{2.15}$$

where dQ is the latent heat of the phase transformation and experimentally can be determined by the use of a DSC.

2.8.2. Stress induced phase transformation at constant temperature

When a stress is applied to a single crystal of SMA in the parent phase, it gives rise to a response that can be written mathematically as follows:

$$dW = V_o \sigma_{ij} d\varepsilon_{ij} \quad , \tag{2.16}$$

where V_o is the volume of the SMA crystal, dW is the mechanical work done as a result of the applied stress σ_{ij}, and ε_{ij} is the incremental macroscopic strain. The change in internal energy for such a system can be written as

$$dE = TdS + V_o \sigma_{ij} d\varepsilon_{ij} \quad , \tag{2.17}$$

and also an expression for the change in enthalpy *dH* can be written as

$$dH = TdS + V_o \sigma_{ij} d\varepsilon_{ij} \quad . \tag{2.18}$$

Equations 2.17 and 2.18 can be simplified for the one-dimensional case and rewritten as

$$dE = TdS + V_o \sigma d\varepsilon \quad , \tag{2.19}$$

$$dH = TdS + V_o \sigma d\varepsilon \quad , \tag{2.20}$$

respectively.

The pressure *p* is atmospheric and hence a constant and also the volume change is negligible for the martensitic transformation.

Similarly, an expression for *dG* can be written in the form

$$dG = -SdT + V_o \sigma d\varepsilon \quad . \tag{2.21}$$

Deformation is more difficult to control than stress and, therefore, it is necessary to introduce a generalized form of the Gibbs free energy G^* into Eq. 2.21, which becomes

$$G^* = G - V_o \sigma d\varepsilon \quad . \tag{2.22}$$

Differentiating Eq. 2.22 with respect to *G* we obtain

$$dG^* = dG - V_o \sigma d\varepsilon - V_o d\sigma\varepsilon \quad . \tag{2.23}$$

Substituting Eq. 2.21 into Eq. 2.23 and rearranging we get

$$dG^* = -SdT - V_o \varepsilon d\sigma \quad . \tag{2.24}$$

At constant temperature *T* and stress σ, thermodynamic equilibrium is characterized by

$dG^* = 0$. For a single crystal SMA specimen subjected to a uniaxial stress, the expressions for the Gibbs free energy for the parent and the martensitic phases can be written as

$$(G^*)^P = H^P - S^P T - V_o \varepsilon^P \sigma \quad , \tag{2.25}$$

$$(G^*)^M = H^M - S^M T - V_o \varepsilon^M \sigma \quad . \tag{2.26}$$

The stress and temperature imposed on the SMA are assumed to be the same for both of the phases, with the thermodynamic potential being different as a result of the phase transformation. An expression for a finite change in the Gibbs free energy can be then written as

$$\Delta G^* = \Delta H^* - T\Delta S - V_o \sigma \Delta \varepsilon \quad . \tag{2.27}$$

During phase transformation $\Delta G^* = 0$ is reached and the latent heat of phase transformation $Q(\sigma)$ can be defined as follows:

$$Q(\sigma) = TdS = \Delta H - V_o \sigma d\varepsilon \quad . \tag{2.28}$$

Rearranging terms in Eq. 2.28 the classical relation between stress and temperature as a result of the phase transformation can be written as follows:

$$\frac{d\sigma}{dT} = \frac{\Delta S}{V_o \Delta \varepsilon} \quad . \tag{2.29}$$

Equation 2.29 is also called as the Clausius-Clayperon equation and is of vital importance in thermomechanical analysis. Equation 2.29 relates stress and temperature during a phase transformation. In Eq. 2.29, ΔS and $\Delta \varepsilon$ are characteristic parameters for a given SMA. The Clausius-Clayperon equation shows a linear dependence between

stress and temperature when ΔS is independent of temperature. Figure 2.14 indicates the step wise change of stress induced deformation at constant temperature. When the stress reaches a critical value given by $\sigma_o(T)$, a volume change equal to $V_o d\varepsilon$ occurs.

An interaction between the parent and the martensitic phases was not taken into account in the previous analysis. That is, the parent and the martensitic phases are not independent. The transformation is discontinuous, is produced in a step by step with each individual step taking less time than the total time for the transformation to occur. Let f_M be the molar fraction of Martensite crystal during transformation. The variation of the internal energy of the transformed fraction increment df_M can be written as

$$\Delta E df_M = T\Delta S df_M + V_o \sigma d\varepsilon df_M \quad . \tag{2.30}$$

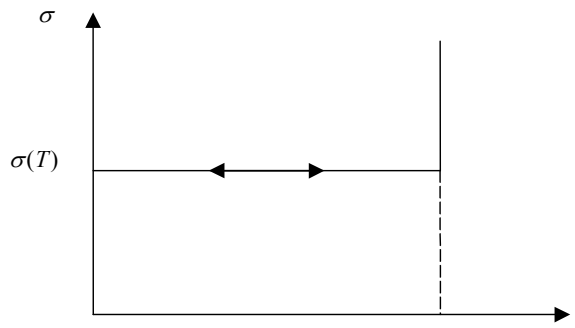

Fig. 2.14. Stepwise change of stress induced crystal deformation at constant temperature.

The crystal gains elastic energy and interfacial energy at the interface between the two phases during the parent to the MT. These energies can be restored during the

reverse transformation. The portion of heat loss due to the internal friction cannot be recovered and taking into considerations all these different energies, the change in internal energy can be written as follows:

$$dE = TdS - TdS_i - dE_{el} + V_o \sigma d\varepsilon \quad , \tag{2.31}$$

where dE_{el} is the reversible part of the interfacial and elastic deformation energies, TdS_i is the irreversible heat loss, $V_o \sigma d\varepsilon$ is always positive as it represents dissipated energy, and

$$dG^* = -SdT - V_o \sigma d\varepsilon - dE_{el} - TdS_i \quad , \tag{2.32}$$

$$dG^* = dG_c + dG_R + dW_i \quad , \tag{2.33}$$

where dG_c is the increment of absorbed or dissipated energy during the chemical reaction, dG_R is the reversible energy of non chemical nature associated with the transformation, and dW_i is the energy dissipated that represents irreversible energy loss.

2.9. Types of shape memory

Shape memory effect is broadly categorized into one-way shape memory, superelasticity, and two-way effect. In addition to the above there exists the R-phase transition. All of the above are primarily due to the martensitic phase transformation. This section provides an introduction with emphasis on advantages and disadvantages of each of the categories of SME.

.

2.9.1. One-way effect

In one-way shape memory effect, also known as Pseudoplasticity (PP), the material undergoes permanent deformation and then regains its undeformed shape when the SMA specimen is heated above the transition temperature (TT). As explained earlier, the TT depends on the stress level of the martensitic phase and hence increases in almost all SMAs with corresponding increase in stress. Typically plastic strains up to 8%, or even 11%, can be recovered in one-way SME. There is however a critical stress, above which permanent damage is caused to the SME. This critical stress (R_{PP}) is lower than the true yield stress of the SMA and defines the upper limit to which the SMA can be safely loaded without causing damage to the SME (Hornbogen, 1995). One-way SME is a one-time phenomenon and hence proper thermomechanical treatment is needed in order to obtain a complete cycle. Care however has to be taken neither to overload nor overheat the SMA specimen, which will lead to degradation in the shape memory effect.

2.9.2. Two-way shape memory effect

Two-way shape memory (TWSM) can be trained into a SMA by thermomechanical cycling. The process of training will generally result in the alloy remembering its low and high temperature shapes. TWSME depends solely on temperature, which means that change in temperature will cause changes in shape. The

SMA will also remember its intermediate shapes in addition to the shapes it assumes at the high and low temperatures.

In one-way shape memory effect after the completion of individual cycles of deformation and heating, the alloy must be re-deformed to repeat the SME. In TWSM only temperature must be varied to affect the change in shape. The amount of strain recovery is however lower in TWSM than in one-way SME. SMAs that have been trained are also referred to in general literature as *educated*. Thermomechanical fatigue is quite necessary for the completion of the education of the SMA. It can, however, have undesirable effects like elevation of the transformation temperatures, widening of the hysteresis loop, and an increase in the levels of residual strains.

Figure 2.14 shows a comparison between the one-way and two-way SME (Duerig, 1990). As illustrated in Fig. 2.15, a collapsed SMA spring (contracted) is recovered following heating to above A_f. The contracted spring remains when the specimen is again cooled to below M_f. This is the one-way shape memory behavior, which is a one time only deployment. In contrast, the TWSM is depicted in the lower half of Fig. 2.15, in which case a contracted spring extends when heated to above A_f, but now spontaneously contracts when cooled again below M_f and this can be repeated indefinitely.

It is important to note that special thermomechanical treatment is required to train a SMA in TWSME mode. The following TWSME training methods are most commonly used and are explained in Sections 2.9.2.1 through 2.9.2.5.

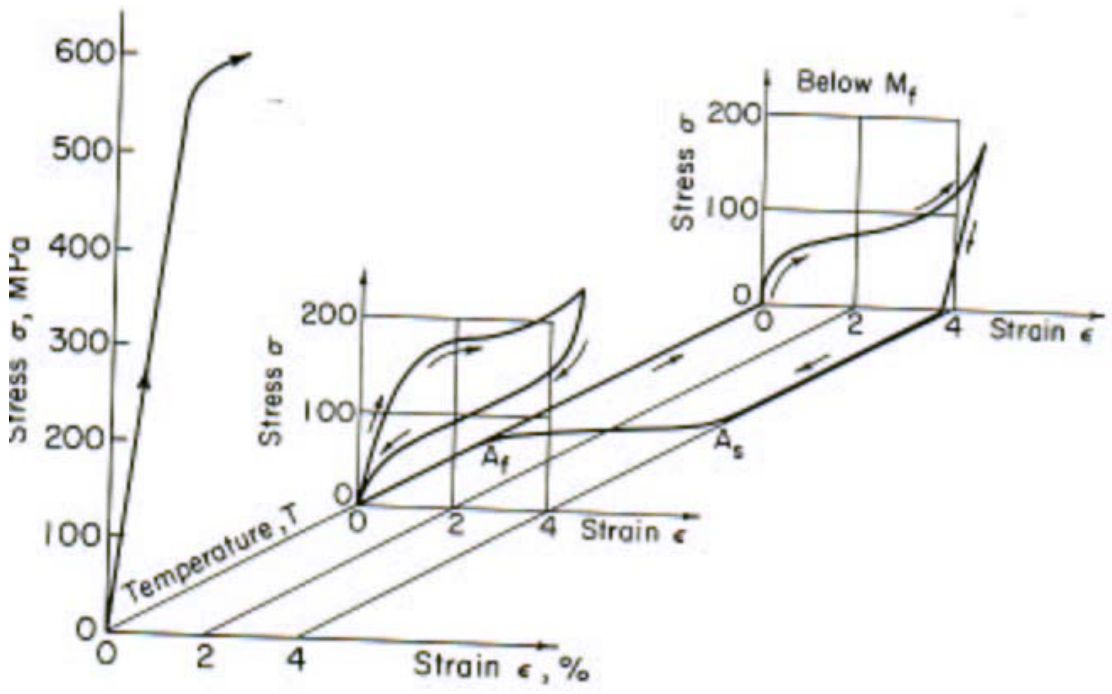

Fig. 2.15. Three-dimensional stress-strain-temperature diagram showing the deformation and shape memory behavior of a Ni-Ti alloy.

2.9.2.1. TWSM training by overdeformation while in the martensitic condition

The alloy is cooled below M_f and while in the martensitic state is severely bent (deformed), to well beyond the normal (usual) strain limit for completely recoverable shape memory. When reheated to the parent phase (Austenite), the SMA will not completely recover its deformed shape due to the excessive deformation of the Martensite. By exceeding the shape memory strain limit (SMSL), a partial loss of shape memory occurs. If the SMA is cooled again to the martensitic state, the alloy will, in a spontaneous manner, revert back toward the overdeformed shape.

2.9.2.2. Training by shape memory cycling

This procedure consists of repeatedly carrying out shape memory cycles until the two-way behavior begins. A typical first shape memory cycle consists of the component being cooled to below M_f, deformed to a level below the SMSL, and then heated to recover the original high temperature undeformed shape. After a number of such cycles (10-15 in number) have been carried out, the component will begin to spontaneously change shape upon cooling, moving in the direction in which the component was consistently deformed during the training cycles. The amount of spontaneous shape change during cooling will be significantly less than that which was being induced in the shape memory deformation. The spontaneous shape change will usually be $1/5$ to $1/4$ of the training strain. For example, if the training strain was 6%, the spontaneous TWSM strain is likely to be no more than 1 or 2%.

2.9.2.3. Training by Pseudoelastic cycling

This method consists of repeatedly stress-inducing Martensite by loading and unloading the parent phase (Austenite) above the A_f temperature, but below the M_d where pseudoelastic (or superelastic) behavior is expected.

2.9.2.4. TWSM training by combined SME/PE training

The component is first deformed in the parent phase condition (Austenite) to stress induce a certain amount of stress biased Martensite, then cooled to below M_f while holding the induced strain in the component, then heating up to recover the original undeformed shape. When this routine is repeated a number of times, TWSM behavior will be obtained on subsequent heating and cooling. This particular method for training a SMA to perform in the TWSM mode is more involved than the ones described in the preceding sections.

2.9.2.5. TWSM training by constrained temperature cycling of deformed Martensite

This is probably the most commonly used training method at present. In this method the sample is deformed below M_f, thus producing a stress-biased martensitic microstructure. The sample is then constrained in the deformed condition and heated to above A_f. The sample is typically cycled from below M_f to above A_f a number of times, with the sample constrained in the original deformed shape, to complete the training routine. This training method proves to be particularly effective and is relatively straightforward to carry out.

2.9.2.6. Limitations on the use of two-way shape memory

The four foremost limitations on the application of TWSME are:

1. **The strain limit:** There is a limit to the amount of reversible strain which can be recovered. Typically this is in the neighborhood of 2%.
2. **Hysteresis**: The inherent temperature hysteresis between the heating and cooling transformations is present.
3. **Low transformation forces on cooling**: This means that one can push much better with the SMA on heating than on cooling.
4. **Upper temperature limit**: If too high a temperature is used during training then the memory may be most due to annealing.

2.9.3. All-Round Shape Memory Effect

The all-round shape memory effect (ARSME) behavior was discovered and named by Honma et al. (1981) in Japan. It is essentially TWSM with the high and low temperature shapes being exact inverses of each other. Stated alternately, the SMA sample deflects one way when heated and the other way when cooled. The metallurgical criteria driving ARSME are different than for TWSM and are presently under further research (Perkins, 1975). Also the training method for ARSME is quite different than for TWSM and can be attained only in certain Ni-Ti alloy systems (those with greater than 50.5 atomic % of Ni). Aging of the alloy at 400°C for about 50 hours has to be conducted and during the aging process, a precipitation reaction occurs (Nishida and

Honma, 1984). The precipitation reaction results in particles that create a back stress and this stress causes a deflection away from the constrained shape when the applied stress is released and cooled. Figure 2.16 shows a schematic representation of the all-round SME

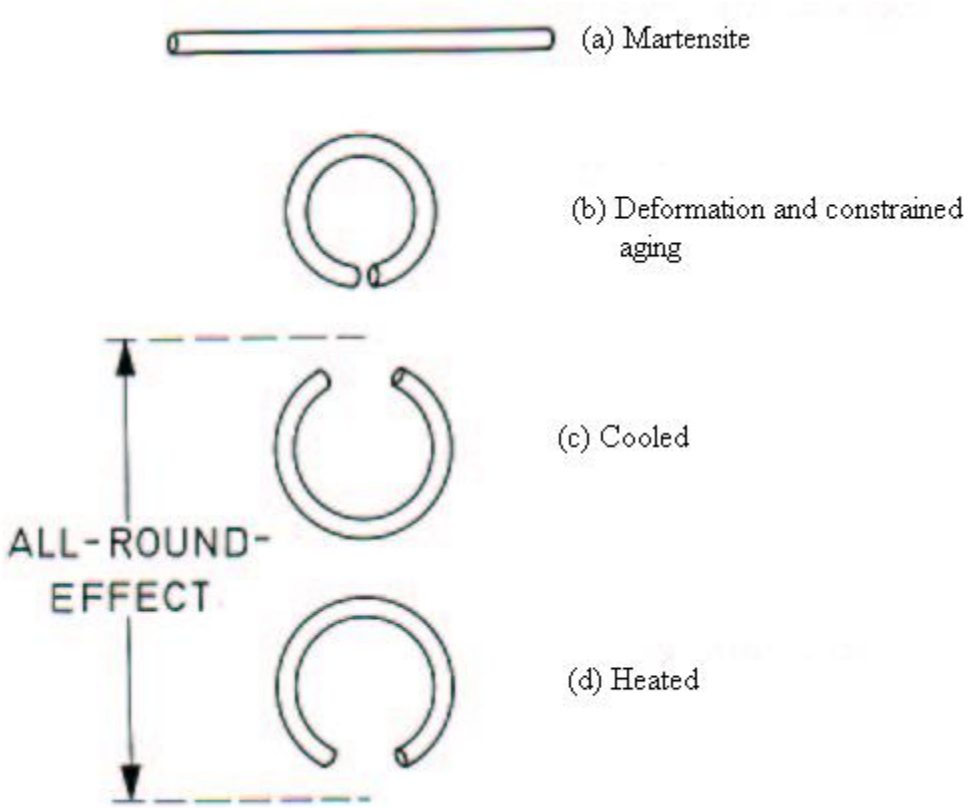

Fig. 2.16. Schematic representation of all-round SME.

2.9.4. Rubber-like behavior (PseudoElasticity, PE)

In conventional alloys elasticity is reversible and results from applied stress. Elastic strain may be either independent of, or dependent on, time and also may be linear or non-linear. On removal of the stress, the atoms return to a position of minimum free energy. Numerous elastic anomalies are known to exist. In monophase alloys these

anomalies are related to the movement of zero to three-dimensional defects (Hornbogen, 1995). Diffusional hops of atoms into new positions under tension result in additional strains and are seen in interstitial alloys.

Shape memory alloys also show elastic anomalies caused by reversible stress-induced phase transformations and have been described in iron, nickel, and copper based alloys. Pseudoelasticity, also known as rubber-like behavior, is accompanied with large deformations with no considerable increase in stress. It is, therefore, very non-linear in comparison with the one-way and TWSM effects. Another distinguishing nature of PE is that it is entirely isothermal. Stated alternately, any non-linearity occurring in the stress strain curve during unloading, can be termed pseudoelasticity.

2.10. Applications of shape memory alloys

SMAs present unique properties in comparison with other structural materials that make them good candidates in various engineering and biomedical applications. Superelasticity, or SME, is usually utilized in the design of SMA components. SMA components are capable of large deformation recovery up to 15%. However, there is a critical strain level when a higher reliability is required and no residual strain is to be present. The critical strain is a function of various processing parameters and also the service environment. The critical strain depends on factors such as the geometric attributes of the component, nature of loading and the number of loading cycles (Gandhi and Thompson, 1995). Determination of the critical strain is not straightforward and

recommended values for the most commonly used SMAs is 6% for NiTiNOL and 2% for CuZnAl.

At present, ten basic SMA systems are in use for industrial and engineering applications. With addition of alloying elements and by various permutations of the basic systems, the number of useable SMA systems can be increased drastically. Reliability is an important issue in engineering design. For components incorporating SMAs, that require great amount of reliability, NiTiNOL is usually used. The other most commonly used SMA is CuZnAl, usually for less reliable component systems. Typical applications of SMAs are diverse and encompass both engineering and biomedical systems. Typical examples are electrical switches, actuators and sensors, safety devices, temperature switches, fire alarms, artificial limbs, catheters, and many others.

2.10.1. Continuum applications: structures and machine systems

Shape memory alloy based smart structures are fabricated with reinforced composite materials, with SMA fibers being embedded either into the matrix material or as in a laminated fiber reinforced composite structure as shown in Fig. 2.17. By changing the temperature beyond the point of phase transition, the shape and material characteristics of the SMA, and hence the shape and global mechanical characteristics of the smart structure are changed too.

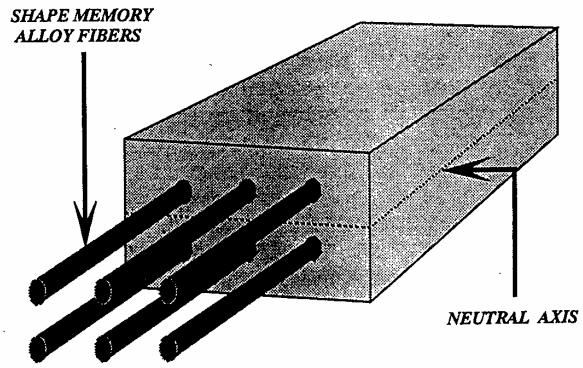

Fig. 2.17. Shape-memory-alloy based smart structure

In a typical beam, shell and plate-like smart structures, the SMA fibers, or films, are embedded in symmetric pairs of neutral axis/surface in order to control the geometry of the structure. Prior to the fabrication of the smart structure, the SMA fibers are plastically deformed and are constrained in a configuration that is different than their memory configuration at the end of the curing cycle. The fibers are electrically heated and once the phase transition temperature is reached, the SMA fibers tend to regain their memory configuration. This process results in a shear force along the length of the fibers.

Steady-state vibration control can also be accomplished with SMA reinforced composites by employing active modal modification. The modal response of a structure can be tuned by heating the SMA fibers to change the stiffness of all, or portions, of the structure. The SMA fibers are placed in, or on, the structure in such a way that that when activated, there will be no resulting deflections, but instead the structure will be placed in

a state of residual state of strain. The resulting stored strain energy changes the energy balance of the structure and modifies the elastodynamic response. This is referred to as 'Active Strain Energy Tuning'.

2.10.2. Discrete applications

SMA devices have applications discrete in nature with typical applications in switching and actuation. A typical application of this kind involving a temperature fuse is shown in Fig. 2.18. Shape memory actuators can be moved or rotated either by heating or through other means of control. Electrical energy is typically used for heating purposes. SMA actuators are not affected by enviornmental factors like humidity and therefore have a distinct advantage over other traditional actuators and/or switches. SMA actuators can therefore be employed as positioning devices for scanning electron microscopes, in reaction vessels, nuclear reactors, and in chemical plants.

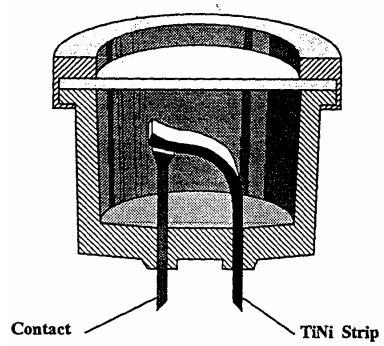

Fig. 2.18. Temperature fuse employing a SMA.

SMA actuators for robots have been developed, and based on operating principles, they are called biased or differential. Biasing uses a coil spring to generate the bias force that opposes the unidirectional force of the SMA. In a differential type, the spring is replaced with another SMA and the opposing forces control the actuation. The assembly of a micro-robot actuated by SMAs is schematically shown in Fig. 2.19 (Gandhi and Thompson, 1995). This micro-robot features five degrees of freedom corresponding to the capabilities of the human fingers, wrist, elbow, and shoulder. The robotic maneuvers and operations are coordinated by activating the SMA (NiTiNOL) wires in the wrist and shoulders.

NiTiNOL sheets and rods twisted into cones and volute springs have been investigated for use in satellite antenna applications. Once the satellite is launched and a stable orbit is reached, the antenna can be deployed from the coiled up state by employing electrical heating or alternatively using diffuse sunlight to provide the required thermal energy.

Several applications of SMAs have been explored in the field of medicine. In medical applications, in addition to mechanical characteristics, highly reliable biological and chemical characteristics are also important. Furthermore, the material must be biocompatible and not result in cytotoxicities, such as abnormalities, for example. NiTiNOL materials, therefore, are the only SMAs suitable for medical applications. NiTiNOL SMAs have been employed in the development of artificial joints including femoral heads and sockets. A typical application of SMAs in prototype filters for

trapping blood clots from moving through the vena cava is shown in Fig. 2.20 (Gandhi and Thompson, 1995).

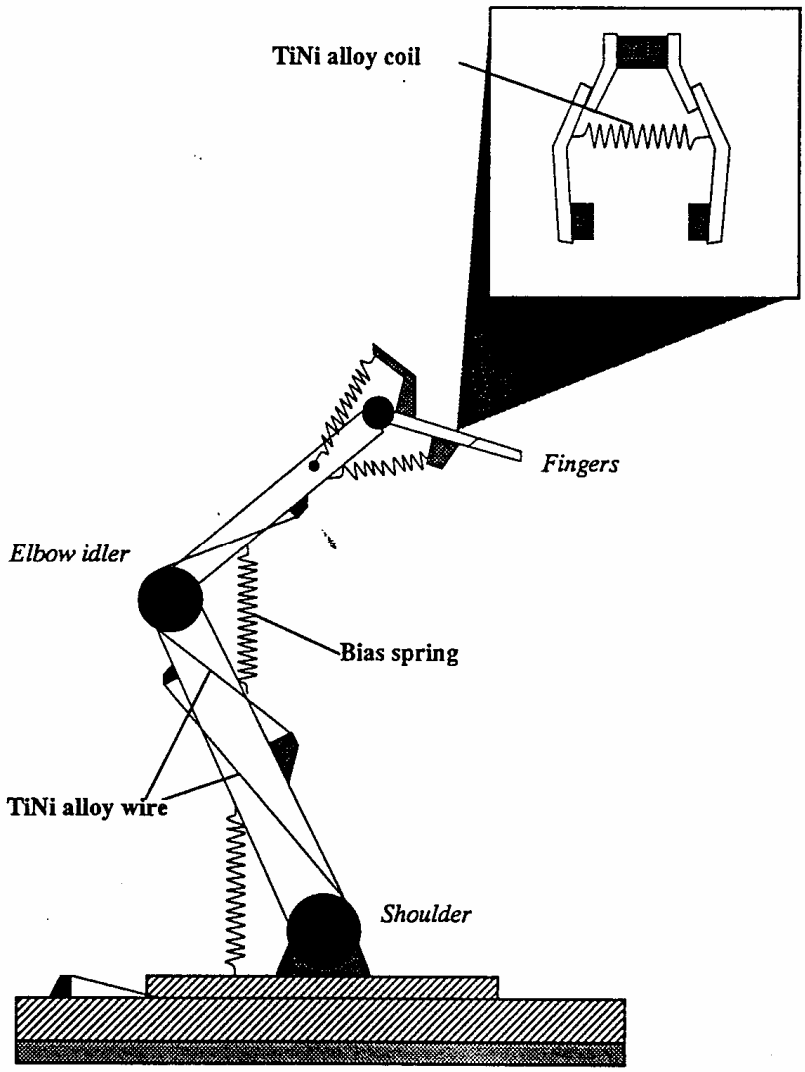

Fig. 2.19. Micro-robot actuated by SMAs.

The SMA wire is inserted into the vena cava through a catheter. Once inside the vena cava, the NiTiNOL wire is heated to the temperature of the blood in the biological

tubular vessel. The change in temperature triggers the reversion of the wire to a complicated memorized shape for a blood filter.

In addition, NiTiNOL SMAs have also been employed for bone plates, and marrow pins for healing fractures in the femur, tibia, and superelastic NiTiNOL wires have been used for connecting broken bones. It is therefore evident that SMAs have potential applications in various fields and it is important that SME be better understood and modeled for maximum usage of this unique phenomenon in engineering and other applications.

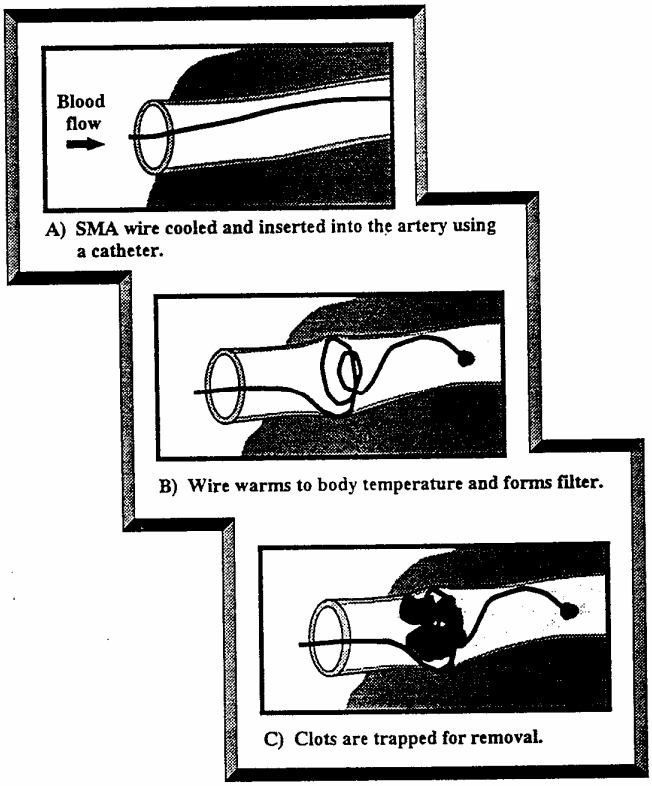

Fig. 2.20. Shape-memory-alloy blood clot filter.

3. NiTi BASED SHAPE MEMORY ALLOYS

Shape memory alloys based on Nickel and Titanium have to date provided the best combination of material properties for most commercial applications. Rapid growth for shape memory alloys was initiated with the discovery of shape memory properties in NiTi system in the 1960's (Duerig, 1990). The discovery took place at NOL, the Naval Ordinance Laboratory and hence the acronym NiTi-NOL.

3.1. Metallurgy of Ni-Ti alloys

NiTi SMAs are ordered intermetallic compounds based on the equiatomic composition. Based on the phase diagram for Ni-Ti (Wasilewski et al., 1974) this compound exists as the stable phase down to room temperature. In contrast to copper based alloys, there is no necessity for betatising and quenching to prevent the decomposition of NiTi into other phases at intermediate temperatures. At low temperatures the stoichiometric range of NiTi is very narrow and therefore the alloys often contain precipitates of a second intermetallic phase. The microstructure is thus primarily single phase, with small amounts of other phases mixed in the matrix. In the molten state, Titanium is very reactive and this results in some oxygen being present in the matrix. This fact is often overlooked. From the Ni-Ti-O phase diagram (Chattopadhyay et al., 1983), oxygen decreases the stoichiometric range of the NiTi compound and can unexpectedly result in compositions within a three phase field. This Ni_3Ti can be present for example in a Titanium rich alloy. Furthermore, the oxide

Ti_4Ni_2O is isostructural with the intermetallic Ti_2Ni, which can make unique phase identification difficult. If the composition of the alloy deviates from stoichiometry, then larger precipitates are present, as seen for Ti-rich alloy. These larger second phase particles can have a marked effect on the hot workability of NiTi, particularly on the Titanium rich side where they are brittle and often result in cracking.

3.2. Mechanical properties

Like most SMAs, NiTi alloys show marked differences in mechanical behavior depending upon whether they are tested in the martensitic or austenitic state. The martensitic stress-strain curve can be divided into three well defined regions, Fig. 3.1. An initial low plateau results from the stress induced growth of one martensitic orientation at the expense of the adjacent. At higher stresses there is a second region that is linear, although not purely elastic. The deformation mechanism in this state is a mixture of elastic deformation on the detwinned Martensite, together with the formation of new orientations of Martensite, which intersect those already present and which provide additional heat recoverable strain.

The transition to the third region is a result of the onset of irreversible plastic deformation, as in the case of yielding of all conventional metals. Therefore the maximum amount of heat recoverable, or memory strain, is obtained by initially deforming the sample to the end of the second stage. If larger deformation strains are

used, then the reversible martensitic deformation processes and the dislocations resulting from plastic flow interact and the memory strain will decrease.

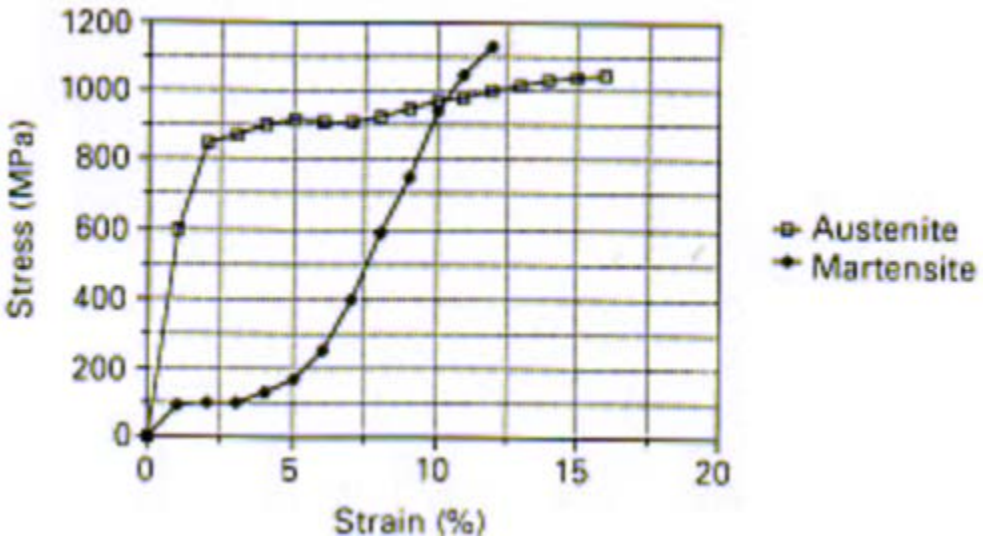

Fig. 3.1. Stress-strain curve for a Ni-Ti-10% Cu alloy in the austenitic and martensitic conditions.

The length of the martensitic plateau in the stress-strain curve extends typically to around 5%-6%. However, depending on the details of the alloy and its prior thermomechanical history, the plateau can vary from a continuous curve with an inflection point to a clear horizontal plateau with a sharp yield point (Wayman and Duerig, 1990).

3.3. Effects of thermomechanical processing

In 1965, four years after the memory effect in NiTi was discovered, a process claiming cold working in the Martensite as a way of increasing the yield strength of the

alloy was formulated (Duerig, 1990). Since that time, the combination of cold working in the Martensite followed by a subsequent anneal has been extensively explored as a way of improving the SMA characteristics (Duerig, 1990). Cold working alone without the annealing step, destroys the martensitic plateau on the stress-strain curve. Thus a material cold worked 20% in the Martensite has a very high yield strength, but poor shape memory properties. Annealing will restore the memory effect, but decrease the yield strength.

The choice of amount of cold work and the annealing temperature dictate the trade off in these two properties. Cold work introduces a high density of random dislocations that impede the mobility of the twin boundaries. Annealing rearranges these dislocations into cells of relatively dislocation free areas within which the Martensite twins can be mobile. Figure 3.2 indicates the affect of cold working followed by annealing on the austenitic yield strength of a 50.6at.%Ni.

3.4. Corrosion behavior of NiTi

In the galvanic series of metals, NiTi based alloys as a family are slightly nobler than stainless steel, and therefore show comparable corrosion behavior. This better resistance is provided by a naturally formed thin oxide coating known as a passive film. The film is very stable and therefore the NiTi alloys are resistant to many forms of corrosive attacks. However in some aggressive conditions, such as highly acidified chloride solutions, breakdown of this passive film can occur. Such corrosive

environments are very severe for most engineering materials; nevertheless if NiTi is to be used in these conditions, some form of protective coating is advisable.

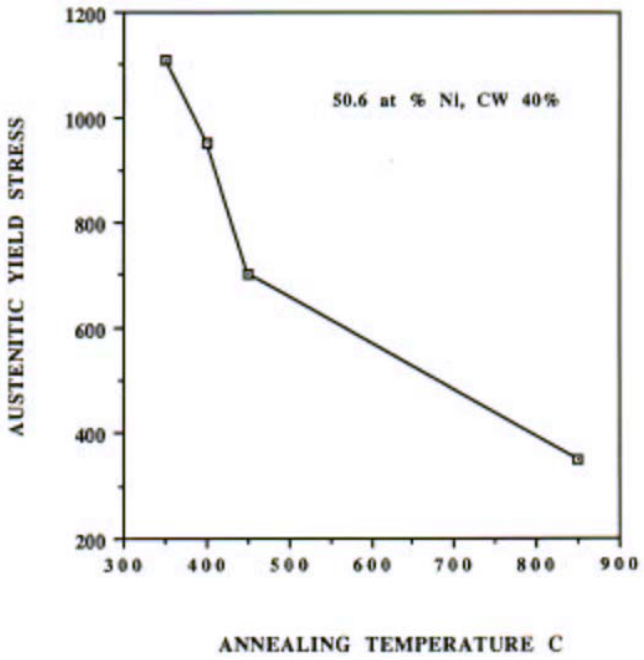

Fig. 3.2. Austenitic yield strength of a 50.6at.%Ni alloy cold worked followed for 30 minutes of annealing.

Electrochemical measurements show that NiTi based alloys have a good resistance to pitting in a chloride environment (Vicentini et al., 1986; Rondelli et al., 1988). However data obtained from a scratch test indicated that the healing of the passive film may be a difficult and relatively slow process (Schwenk and Huber, 1974; Eckelmeyer, 1976). Comparing with other commercially available SMAs, NiTi is by far the most corrosion resistant. For applications such as actuators, electrical connectors and

fasteners, NiTi has a superior corrosion behavior than the other components of the assembly, and therefore is a better candidate in such applications. In the case of coupling applications, corrosion resistance is more than adequate except in very severe operating conditions, where protection is advisable. As a general rule, if no corrosion protection is deemed necessary for the pipes and tubes, then none is required for the NiTi used to join them.

3.4. Effect of alloying elements

The addition of a third or fourth element to NiTi can be a powerful tool for controlling its properties, and can be used to:

1) control transformation temperatures,
2) increase the stability of Ms with respect to thermal history,
3) control the hysteresis width,
4) increase austenitic strength,
5) reduce or increase the martensitic strength,
6) improve corrosion resistance,
7) suppress the R-phase.

Some of the additions giving particularly useful combinations of properties are copper, niobium, and precious metals.

4. METHODOLOGY

4.1. ACES methodology

Methodology that is used relates to the engineering tools that are employed in an investigation and has a direct impact on the end results. The ACES methodology (Pryputniewicz, 1997), an acronym for Analytical Computational and Experimental Solutions, is used in this Dissertation. Using this methodology a hybrid optimal solution is sought that may not be possible using other methodologies. Also later in this chapter uncertainty analysis are discussed as pertaining to critical variables affecting SME for NiTiNOL (Pryputniewicz, 1993; Mizar, 1999). This analysis is very useful in setting tolerances for design parameters. As such, it facilitates proper operation and may prevent premature failure.

In this Dissertation an approach, based on the ACES methodology is used to arrive at an optimal solution. The NiTi sample after appropriate heat treatment at 400°C for two hours (recommended by the manufacturer), are subjected to experimentation and the modulus of elasticity as a function of temperature is determined from measured resonant frequencies of the specific samples.

Figure 4.1 indicates a typical flow chart for the ACES methodology as used in engineering practice (Pryputniewicz, 1997). Design of very complex engineering systems is very difficult to arrive at through a trial and error based approach (Macek and Pitarresi, 1993; Pryputniewicz, 1994b). Complexity in design can arise as a result of an increased number of design variables, and also restrictions on geometry of the components. In the analysis of such complex components, both experimental and

theoretical models are of equal importance, and equally indispensable for the design of a viable, reliable, and low cost products (Suhir, 1989). Each of these methodologies can complement each other thus minimizing the effects of errors in design.

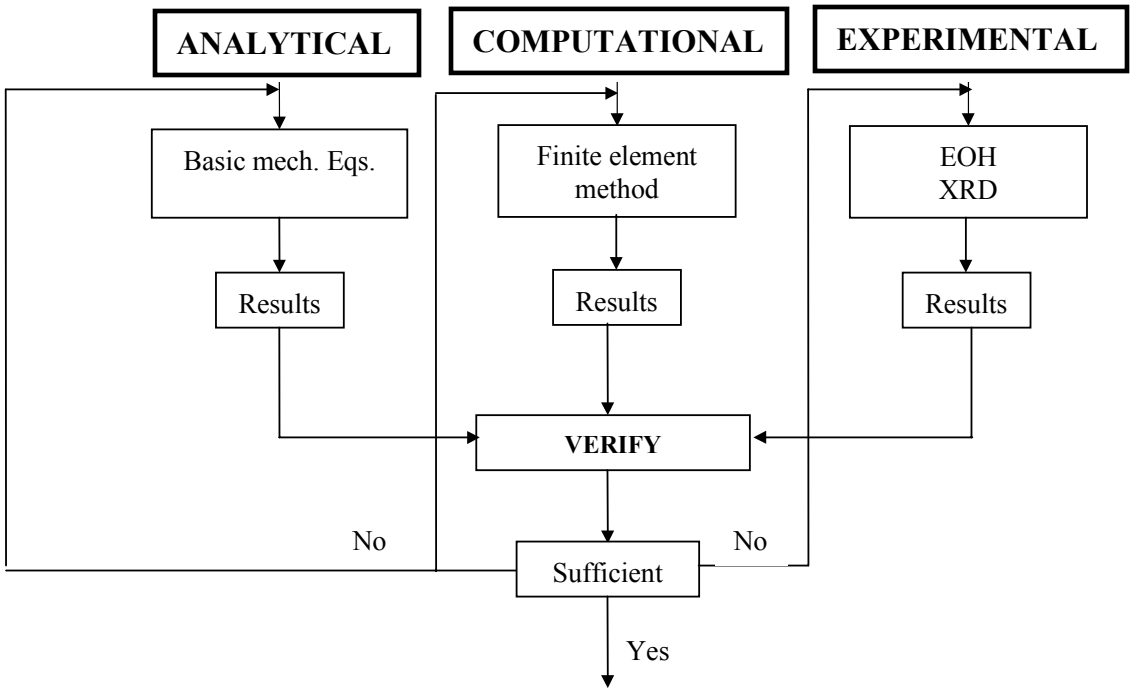

Fig. 4.1. A flow-chart representation of ACES methodology.

4.1.1. Analytical modeling

Analytical solutions pertain to the use of equations from mechanics to investigate the problem at hand in order to obtain some preliminary results. This analytical investigation provides information that can be utilized to design experimental or computational procedures for that particular problem. The equations that are used in

modeling a system do not sometimes model the actual component, but rather approximate it. An analytical approach provides information on any computational and experimental works that have to be conducted (Pryputniewicz, 1997).

Analytical modeling can predict experimental results in less time, providing proper analytical models are being used. Also, initial analytical modeling can ensure proper experimental planning and may help in devising proper computational models. Analytical modeling is indeed a very valuable tool for preliminary investigation of a problem. Analytical modeling for non-linear models can be approached from a practical approach that is by the use of linear theory. Any uncertainties will be evident in computation and experimentation. Therefore analytical modeling of complex systems is not always sufficient and, therefore, computational and experimental methodologies should be used in conjunction with analytical modeling.

4.1.1.1. Uncertainty analysis

Experimental data may have inherent errors. Specific analysis must be, therefore, performed on the data to take into account the errors in measurements.

In general, experimental results are validated through analysis of data to determine errors and precision. In this Dissertation a method of estimating the effect of errors and tolerances (uncertainty) in interpretation of results, originally proposed by Kline and McClintock (Mizar, 1999), is used. This method is based on specifications of the uncertainties in the variables (Pryputniewicz, 1993). The uncertainty of the calculated result is determined based on the uncertainties in the measurements. Suppose

the result *R* is a known function of the independent variables $x_1, x_2, x_3 \cdots\cdots x_n$. Mathematically a fundamental equation representing this can be written as

$$R = R(x_1, x_2, x_3, \cdots\cdots, x_n) \quad . \tag{4.1}$$

Let δ_R be the uncertainty in the result and $\delta_1, \delta_2, \delta_3, \cdots\cdots, \delta_n$ be the uncertainties in the independent variables. Provided the uncertainties in all of the independent variables are predetermined and, therefore, known, the uncertainty in the result, that is, δ_R, can be determined by the following equation (Pryputniewicz, 1993):

$$\delta_R = \left[\left(\frac{\partial R}{\partial x_1} \delta_1 \right)^2 + \left(\frac{\partial R}{\partial x_2} \delta_2 \right)^2 + \left(\frac{\partial R}{\partial x_3} \delta_3 \right)^2 + \cdots\cdots + \left(\frac{\partial R}{\partial x_n} \delta_n \right)^2 \right]^{\frac{1}{2}} , \tag{4.2}$$

where $\frac{\partial R}{\partial (\ )}$ represents partial derivatives of *R* with respect to the independent variables, one at a time.

It is important to take into account the fact that the uncertainty propagation in the result δ_R based on Eq. 4.2 depends on the square of the sum of the squares of the products of the partial derivatives of *R* with respect to the independent variables with the corresponding uncertainties in these variables. As such, the uncertainty represented by Eq. 4.2 is also known as root-sum-square-uncertainty (or RSS-uncertainty) (Pryputniewicz, 1993). So if the uncertainty of one variable is significantly greater than the other variables it is the larger uncertainty that predominates and the others have a less significant contribution.

In this Dissertation, the modulus of elasticity was determined from the resonant frequency. The modulus of elasticity for NiTi is non-linear with temperature as a result

of the phase transformation from Martensite to Austenite. This thermomechanical dependence makes it essential for determination of tolerances for values for the modului of elasticity for Martensite and Austenite. Based on analytical considerations, the modulus of elasticity can be expressed as

$$E = E(f_R, h, L_{eff}, \rho) \quad , \tag{4.3}$$

where E is the modulus of elasticity, f_R is the resonance frequency, h is the thickness of the SMA (NiTi) ribbon, L_{eff} is the effective length of the SMA (NiTi) ribbon when mounted as a cantilever beam, and ρ is the density of the SMA (NiTi) ribbon.

It is important to note that if non-linear theory is used, then the modulus of elasticity would be a function of temperature in addition to the above mentioned variables. The uncertainties in the independent variables namely, f_R, h, L_{eff}, and ρ are predetermined and, therefore, the uncertainty in the modulus of elasticity can be written in the following form:

$$\delta E = \left[\left(\frac{\partial E}{\partial f_R} \delta f_R \right)^2 + \left(\frac{\partial E}{\partial h} \delta h \right)^2 + \left(\frac{\partial E}{\partial L_{eff}} \delta L_{eff} \right)^2 + \left(\frac{\partial E}{\partial \rho} \delta \rho \right)^2 \right]^{\frac{1}{2}} \quad . \tag{4.4}$$

Based on the uncertainty in the modulus of elasticity determined from Eq. 4.4, the tolerance levels for the modulus of elasticity can be written as

$$E_{act} = E \pm \delta E \quad . \tag{4.5}$$

Equation 4.5 gives the range over which the modulus of elasticity can vary as a result of uncertainties in its independent variables. The uncertainty in the modulus of

elasticity can be controlled (reduced or increased) by controlling the uncertainties of the independent variables. Manufacturing limitations are one classical factor that is utilized in controlling the variables relating to the dimensions of the NiTi samples.

Similarly, a dynamic response of composite materials that incorporated NiTi fibers was also investigated in this Dissertation. Stiffness of a composite that includes NiTi as reinforcements, based on analytical considerations, is

$$D_{11} = D_{11}(E_L, E_T, h, \mu_{LT}) \quad , \tag{4.6}$$

where D_{11} is the dynamic stiffness, E_L is the modulus of elasticity in the longitudinal direction of the composite, E_T is the modulus of elasticity in the transverse direction of the composite, h is the thickness, and μ_{LT} is the Poisson's ratio for the composite. Therefore, based on Eq. 4.6 the RSS-uncertainty in the stiffness can be written as

$$\delta D_{11} = \left[\left(\frac{\partial D_{11}}{\partial E_L} \delta E_L \right)^2 + \left(\frac{\partial D_{11}}{\partial E_T} \delta E_T \right)^2 + \left(\frac{\partial D_{11}}{\partial h} \delta h \right)^2 + \left(\frac{\partial D_{11}}{\partial \mu_{LT}} \delta \mu_{LT} \right)^2 \right]^{\frac{1}{2}} \quad . \tag{4.7}$$

The tolerance in the stiffness based on the uncertainty given by Eq. 4.6 can be written as

$$D_{11_{act}} = D_{11} + \delta D_{11} \quad . \tag{4.8}$$

4.1.2. Computational modeling

Computational modeling has become popular in solving problems in conjunction with analytical and experimental methodologies. With proper understanding of material properties, computational modeling can be used to predict material behaviors under

simple as well as complex loading situations and display results in a timely manner. Various computational techniques have been developed, with the most popular being the Finite Difference Method (FDM), the Finite Element Method (FEM) and the Boundary Element Method (BEM).

FEM is mostly used in the regimes of engineering design and analysis. As with any computational technique, FEM provides accurate results when utilized appropriately, and can predict responses very accurately. Common difficulties in computational techniques are, but are not limited to, geometry definition, application of boundary conditions, and sufficient knowledge of material properties.

4.1.3. Experimental modeling

Barishpolsky (1980) has stated that experimentation relies on the perfection of measurement methods and increasing the accuracy of these measurements.

Experimentation is carried out on a point by point basis on a component and results are obtained. Values at points other than those measured can be determined through interpolation from known values. The results from experimental investigations usually indicate combined effects of various factors affecting the component. Therefore in design optimization, the affect of various factors must be taken into consideration.

Testing often shows the “negative bad” points and not the “negative good” points. By this we mean that testing can show us an insufficient/weak joint or other parameter, “negative bad”. On the other hand testing does not indicate areas of "over design" in the

form of excessive volumes or elevated safety margins (Suhir, 1989). Over designing a component adds additional costs and increases production times. It is therefore essential to optimize designs so that production and costs are minimal.

It is therefore necessary for analytical, computational, and experimental methodologies to be used in unison to arrive at an optimal solution of a component, that will keep production costs down and also satisfactorily perform its intended function.

The values obtained from the three methodologies have to be compared and corrected if necessary, so that results converge to an optimal solution for the NiTiNOL sample being investigated. Detailed analytical, computational, and experimental considerations are discussed in Chapters 5, 6, and 7, respectively.

5. ANALYTICAL INVESTIGATIONS

This chapter addresses analytical solutions used in the Dissertation. Microstructural changes as a result of the phase transformation are neglected in the determination of material properties. Also the SMA is characterized by itself and the approach is extended to composite structures that incorporate the SMAs. Beam theory and energy methods are used to formulate dynamic behavior of the SMA and SMA based composites. Section 5.1 discusses mechanics of vibration of anisotropic plates, and Section 5.2 discusses mechanics of vibration of cantilever beams.

5.1. Free vibration of rectangular anisotropic plates

The Ritz method provides a convenient method for obtaining approximate solutions to boundary value problems (Whitney and Ashton, 1987). This approach is equally applicable to bending, buckling, and free vibration problems. Each of these problems is governed by an energy condition and can be written in the following form:

$$\Pi\left(u^0, v^0, w\right) = \text{stationary value} \quad , \tag{5.1}$$

where

$$\Pi = U + W \qquad \text{(transverse bending)} \quad , \tag{5.2}$$

$$\Pi = U + W + T \qquad \text{(buckling)} \quad , \tag{5.3}$$

$$\Pi = U + W + V - T \qquad \text{(free vibration)} \quad . \tag{5.4}$$

where Π represents the energy condition of an elastic body, U is the strain energy, W is the potential energy of external loads, V is the potential energy due to inplane loads, and T is the kinetic energy.

For a free vibration time can be removed from Eq. 5.4 by considering displacement fields of the form

$$u^0(\mathrm{t}) = u^0 \mathrm{e}^{\mathrm{i}\omega \mathrm{t}} \quad , \tag{5.5}$$

$$v^0(\mathrm{t}) = v^0 \mathrm{e}^{\mathrm{i}\omega \mathrm{t}} \quad , \tag{5.6}$$

$$w(\mathrm{t}) = w \mathrm{e}^{\mathrm{i}\omega \mathrm{t}} \quad , \tag{5.7}$$

where u, v, and w are displacement fields of a plate, ω is the angular frequency of vibration, and t represents time.

Under the assumed displacements given by Eqs 5.5 to 5.7, the potential energy T can be written as

$$T = \frac{1}{2} \int\int \rho \omega^2 \left[\left(u^0 \right)^2 + \left(v^0 \right)^2 + (w)^2 \right] dx\, dy \, , \tag{5.8}$$

where ρ represents the density of the plate. Equation 5.8 allows the free vibration problem to be solved as a static problem by considering the kinetic energy to be simply additional energy.

In Ritz method a solution is sought of the form

$$\begin{aligned} u^0 &= \sum_{m=1}^{M_1} \sum_{n=1}^{N_1} A_{mn} U_{mn}(x, y) \quad , \\ v^0 &= \sum_{m=1}^{M_2} \sum_{n=1}^{N_2} B_{mn} V_{mn}(x, y) \quad , \\ w &= \sum_{m=1}^{M_3} \sum_{n=1}^{N_3} C_{mn} W_{mn}(x, y) \quad , \end{aligned} \tag{5.9}$$

where A_{mn}, B_{mn}, and C_{mn} are undetermined coefficients. The functions U_{mn}, V_{mn}, and W_{mn} are known and usually chosen in the variables separate form $X_m(x)$ and $Y_n(y)$. The geometric boundary conditions must be satisfied by these conditions. In addition they should be continuous through at least the same order derivative as required in the corresponding differential equations. Substitution of Eqs 5.9 into the energy condition given by Eq. 5.1 leads to a minimization problem relative to the undetermined coefficients. In particular, Π is a function of A_{mn}, B_{mn}, and C_{mn} only and the conditions given by Eq. 5.1 reduce to the equations

$$\begin{aligned}
&\frac{\partial \Pi}{\partial A_{mn}} = 0 \quad \begin{cases} m = 1, 2, \cdots, M_1 \\ n = 1, 2, \cdots, N_1 \end{cases} , \\
&\frac{\partial \Pi}{\partial B_{mn}} = 0 \quad \begin{cases} m = 1, 2, \cdots, M_2 \\ n = 1, 2, \cdots, N_2 \end{cases} , \\
&\frac{\partial \Pi}{\partial C_{mn}} = 0 \quad \begin{cases} m = 1, 2, \cdots, M_3 \\ n = 1, 2, \cdots, N_3 \end{cases} .
\end{aligned} \tag{5.10}$$

For the formulation presented by Eq. 5.10, Π is always in the undetermined coefficients. Thus, the conditions given by Eq. 5.10 lead to a $\sum_{i=1}^{3} M_i \times N_i$ set of linear simultaneous equations. For buckling and free vibration problems, Eq. 5.10 leads to a classic eigenvalue problem, that is, buckling loads and free vibration frequencies are chosen such that the determinant of the coefficients of A_{mn}, B_{mn}, and C_{mn} vanish.

Strain energy of an elastic body in terms of *x*, *y*, and *z* coordinate system is given by the relationship (Whitney and Ashton, 1987).

$$U = \frac{1}{2} \int\int\int \left(\sigma_x \varepsilon_x + \sigma_y \varepsilon_y + \sigma_z \varepsilon_z + \sigma_{xz} \varepsilon_{xz} + \sigma_{yz} \varepsilon_{yz} + \sigma_{xy} \varepsilon_{xy} \right) dx\, dy\, dz \quad , \tag{5.11}$$

where the triple integration is performed over the volume of the body. Taking into account the basic assumptions of laminated plate theory, i.e., $\varepsilon_z = \varepsilon_{xz} = \varepsilon_{yz} = 0,$ along with the stress-strain relations, we can rewrite Eq. 5.11 as

$$U = \frac{1}{2}\int\int\int \left(Q_{11}^{(k)}\varepsilon_x^2 + 2Q_{12}^{(k)}\varepsilon_x\varepsilon_y + 2Q_{16}^{(k)}\varepsilon_x\varepsilon_{xy} + 2Q_{26}^{(k)}\varepsilon_y\varepsilon_{xy} + Q_{22}^{(k)}\varepsilon_y^2 + Q_{66}^{(k)}\varepsilon_{xy}^2 \right) dx \;\; dy \;\; dz \;\; . \tag{5.12}$$

Equation 5.12 can be expressed in terms of the laminate displacements by substituting the strain-displacement relations given by

$$\begin{aligned} \varepsilon_x &= \frac{\partial u^0}{\partial x} - z\frac{\partial^2 w}{\partial x^2} \quad , \\ \varepsilon_y &= \frac{\partial v^0}{\partial y} - z\frac{\partial^2 w}{\partial y^2} \quad , \\ \varepsilon_{xy} &= \frac{\partial u^0}{\partial y} + \frac{\partial v^0}{\partial x} - 2z\frac{\partial^2 w}{\partial x \partial y} \quad . \end{aligned} \tag{5.13}$$

On substituting Eq. 5.13 into Eq. 5.12 and integrating with respect to *z*, the following is obtained:

$$U=\frac{1}{2}\int\int\left\{\begin{array}{l}A_{11}\left(\frac{\partial u^0}{\partial x}\right)^2+2A_{12}\frac{\partial u^0}{\partial x}\frac{\partial v^0}{\partial y}+A_{22}\left(\frac{\partial v^0}{\partial y}\right)^2\\+2\left(A_{16}\frac{\partial u^0}{\partial x}+A_{26}\frac{\partial v^0}{\partial y}\right)\left(\frac{\partial u^0}{\partial y}+\frac{\partial v^0}{\partial x}\right)+A_{66}\left(\frac{\partial u^0}{\partial y}+\frac{\partial v^0}{\partial x}\right)^2\\-B_{11}\frac{\partial u^0}{\partial x}\frac{\partial^2 w}{\partial x^2}-2B_{12}\left(\frac{\partial v^0}{\partial y}+\frac{\partial^2 w}{\partial x^2}+\frac{\partial u^0}{\partial x}+\frac{\partial^2 w}{\partial y^2}\right)\\-B_{22}\frac{\partial v^0}{\partial y}\frac{\partial^2 w}{\partial y^2}-2B_{16}\left[\frac{\partial^2 w}{\partial x^2}\left(\frac{\partial u^0}{\partial y}+\frac{\partial v^0}{\partial x}\right)+2\frac{\partial u^0}{\partial x}\frac{\partial^2 w}{\partial x\partial y}\right]\\-2B_{26}\left[\frac{\partial^2 w}{\partial y^2}\left(\frac{\partial u^0}{\partial y}+\frac{\partial v^0}{\partial x}\right)+2\frac{\partial v^0}{\partial y}\frac{\partial^2 w}{\partial x\partial y}\right]\\-4B_{66}\frac{\partial^2 w}{\partial x\partial y}\left(\frac{\partial u^0}{\partial y}+\frac{\partial v^0}{\partial x}\right)+D_{11}\left(\frac{\partial^2 w}{\partial x^2}\right)^2+2D_{12}\frac{\partial^2 w}{\partial x^2}\frac{\partial^2 w}{\partial y^2}\\+D_{22}\left(\frac{\partial^2 w}{\partial y^2}\right)^2+4\left(D_{16}\frac{\partial^2 w}{\partial x^2}+D_{26}\frac{\partial^2 w}{\partial y^2}\right)\frac{\partial^2 w}{\partial x\partial y}\\+4D_{66}\left(\frac{\partial^2 w}{\partial x\partial y}\right)^2\end{array}\right\}\quad, \tag{5.14}$$

where A_{ij}, B_{ij}, and D_{ij} are defined as

$$\left(A_{ij},B_{ij},D_{ij}\right)=\int_{-\frac{h}{2}}^{\frac{h}{2}}Q_{ij}^{(k)}\left(1,z,z^2\right)\,dz\quad, \tag{5.15}$$

and

$$Q_{ij}=c_{ij}-\frac{c_{i3}c_{j3}}{c_{33}}\quad, \tag{5.16}$$

where the coefficient c_{ij} represents the general plate stiffness based on the Hooke's law. The strain energy expression, given by Eq. 5.14, contains coupling between the inplane displacements u^0, v^0 and the transverse displacement w, due to the presence of products of these terms. The bending-stretching coupling is because of the B_{ij} stiffness terms. For

symmetric laminates the B_{ij} terms are identically zero, and Eq. 5.14 uncouples and reduces to the following:

$$U = \frac{1}{2}\int\int \left\{ \begin{array}{l} A_{11}\left(\frac{\partial u^0}{\partial x}\right)^2 + 2A_{12}\frac{\partial u^0}{\partial x}\frac{\partial v^0}{\partial y} + A_{22}\left(\frac{\partial v^0}{\partial y}\right)^2 \\ +2\left(A_{16}\frac{\partial u^0}{\partial x} + A_{26}\frac{\partial v^0}{\partial y}\right)\left(\frac{\partial u^0}{\partial y} + \frac{\partial v^0}{\partial x}\right) + A_{66}\left(\frac{\partial u^0}{\partial y} + \frac{\partial v^0}{\partial x}\right)^2 \\ +D_{11}\left(\frac{\partial^2 w}{\partial x^2}\right)^2 + 2D_{12}\frac{\partial^2 w}{\partial x^2}\frac{\partial^2 w}{\partial y^2} \\ +D_{22}\left(\frac{\partial^2 w}{\partial y^2}\right)^2 + 4\left(D_{16}\frac{\partial^2 w}{\partial x^2} + D_{26}\frac{\partial^2 w}{\partial y^2}\right)\frac{\partial^2 w}{\partial x \partial y} \\ +4D_{66}\left(\frac{\partial^2 w}{\partial x \partial y}\right)^2 \end{array} \right\} . \qquad (5.17)$$

In Eq. 5.17 the first term on the right hand side contains only the inplane displacements u^0 and v^0, while the second term contains only the transverse displacement *w*. Thus, for pure bending problems the first expression can be considered an arbitrary constant and the strain energy for transverse bending of a laminated plate can be written as

$$U = \frac{1}{2}\int\int \left\{ \begin{array}{l} D_{11}\left(\frac{\partial^2 w}{\partial x^2}\right)^2 + 2D_{12}\frac{\partial^2 w}{\partial x^2}\frac{\partial^2 w}{\partial y^2} \\ +D_{22}\left(\frac{\partial^2 w}{\partial y^2}\right)^2 + 4\left(D_{16}\frac{\partial^2 w}{\partial x^2} + D_{26}\frac{\partial^2 w}{\partial y^2}\right)\frac{\partial^2 w}{\partial x \partial y} \\ +4D_{66}\left(\frac{\partial^2 w}{\partial x \partial y}\right)^2 \end{array} \right\} dx \;\; dy + C \quad , \qquad (5.18)$$

where C is an arbitrary constant. Equation 5.18 is identical to the expression found for the bending strain energy of a homogeneous anisotropic plate (Whitney and Ashton, 1987).

The kinetic energy T of an elastic body in terms of x, y, and z coordinate system can be written in the form

$$T = \frac{1}{2}\int\int\int \rho_0 \left[\left(\frac{\partial u}{\partial t}\right)^2 + \left(\frac{\partial v}{\partial t}\right)^2 + \left(\frac{\partial w}{\partial t}\right)^2 \right] dx\, dy\, dz\,, \tag{5.19}$$

where ρ_0 is the density of the material and the triple integration is performed over the volume of the body. The displacement fields can be written as

$$\begin{aligned} u &= u^0 - z\frac{\partial w}{\partial x} \quad , \\ v &= v^0 - z\frac{\partial w}{\partial y} \quad , \end{aligned} \tag{5.20}$$

where w is independent of z. Substituting Eq. 5.20 in Eq. 5.19 the kinetic energy of the laminated plate becomes

$$T = \frac{1}{2}\int\int\int \rho_0^{(k)} \left[\left(\frac{\partial u^0}{\partial t} - z\frac{\partial^2 w}{\partial x \partial t}\right)^2 + \left(\frac{\partial v^0}{\partial t} - z\frac{\partial^2 w}{\partial y \partial t}\right)^2 + \left(\frac{\partial w}{\partial t}\right)^2 \right] dx\ \ dy\ \ dz \quad , \tag{5.21}$$

where $\rho_0^{(k)}$ denotes the density of the k^{th} layer. Integrating Eq. 5.21 with respect to z and neglecting time derivatives of plate slopes we have

$$T = \frac{1}{2}\int\int \left[\rho \left(\frac{\partial u^0}{\partial t}\right)^2 + \left(\frac{\partial v^0}{\partial t}\right)^2 + \left(\frac{\partial w}{\partial t}\right)^2 \right] dx\ \ dy \quad , \tag{5.22}$$

where ρ is the integral of the density through the thickness of the plate.

Also, it is important to consider the potential energy due to transverse loads and inplane loads. For transverse bending, loads generated by applying normal tractions to the top and bottom surfaces of the plate lead to the potential energy equation given by

$$W = -\int\int \left[\sigma_z \left(\frac{h}{2} \right) - \sigma_z \left(-\frac{h}{2} \right) \right] w \; dx \; dy \quad . \tag{5.23}$$

Equation 5.23 can be rewritten as

$$W = -\int\int qw \; dx \; dy \quad . \tag{5.24}$$

The potential energy V of inplane loads due to deflection w is

$$V = \int\int \left(N_x^i \varepsilon_x^{'} + N_y^i \varepsilon_y^{'} + N_{xy}^i \varepsilon_{xy}^{'} \right) \; dx \; dy \quad , \tag{5.25}$$

where N_x^i, N_y^i, N_{xy}^i are initial inplane force resultants applied to the plate in a pre-buckled state and $\varepsilon_x^{'}$, $\varepsilon_y^{'}$, $\varepsilon_{xy}^{'}$ are the midplane strains due to the deflection w. These strains are usually associated with the large deflection analysis. In the context of linear elasticity theory these strains are applied for the purpose of determining critical buckling loads. These strains are of the following form:

$$\begin{aligned} \varepsilon_x^{'} &= \frac{1}{2} \left(\frac{\partial w}{\partial x} \right) \quad , \\ \varepsilon_y^{'} &= \frac{1}{2} \left(\frac{\partial w}{\partial y} \right) \quad , \\ \varepsilon_{xy}^{'} &= \frac{\partial w}{\partial x} \frac{\partial w}{\partial y} \quad , \end{aligned} \tag{5.26}$$

respectively.

Equation 2.25 therefore takes the form

$$V = \frac{1}{2}\int\int\left(N_x^i\left(\frac{\partial w}{\partial x}\right)^2 + N_y^i\left(\frac{\partial w}{\partial y}\right)^2 + N_{xy}^i\frac{\partial w}{\partial x}\frac{\partial w}{\partial y}\right)\, dx\ \ dy \quad . \tag{5.27}$$

The dynamic analysis was conducted based on the assumption that the composite was a symmetric orthotropic plate. The equation of motion (EOM) for such a plate can be written in the form (Rogers, 1988)

$$D_{11}\frac{\partial^4 w}{\partial x^4} + 2\left(D_{12} + 2D_{66}\right)\frac{\partial^4 w}{\partial x^2 \partial y^2} + D_{22}\frac{\partial^4 w}{\partial y^4} = 0 \quad , \tag{5.28}$$

where D_{ij} is a function of the effective moduli in the transverse and longitudinal directions of the composite. The frequency of vibration of the plate, based on Eq. 5.28 was solved by Mizar and Pryputniewicz (2004).

In the case where one edge is clamped and the other free (cantilever configuration) it is possible to express the deflection by the beam function given by Eqs 5.29 and 5.30.

For the edge $x=0$ clamped and the edge $x=a$ free

$$X_m(x) = \cos\frac{\lambda_m x}{a} - \cosh\frac{\lambda_m x}{a} - \gamma_m\left(\sin\frac{\lambda_m x}{a} - \sinh\frac{\lambda_m x}{a}\right) \quad , \tag{5.29}$$

For the edge $y=0$ clamped and the edge $y=b$ free

$$Y_n(y) = \cos\frac{\lambda_n y}{b} - \cosh\frac{\lambda_n y}{b} - \gamma_n\left(\sin\frac{\lambda_n y}{b} - \sinh\frac{\lambda_n y}{b}\right) \quad , \tag{5.30}$$

where λ_m, λ_n, γ_m, and γ_n have nontrivial solutions given by

$$\cos\lambda_i \cosh\lambda_i = -1 \quad . \tag{5.31}$$

It is important to note that if the beam functions defined by Eqs 5.28 through 5.31 satisfy the boundary conditions exactly at the free ends of a beam then they satisfy the boundary conditions only approximately in the case of a plate (Whitney and Ashton, 1987). The frequency of resonance using the Ritz's method as discussed earlier in this Section can be approximated to be equal to (Whitney and Ashton, 1987)

$$f_i = \frac{1}{2\pi} K_i \frac{1}{ab} \sqrt{\frac{D_{11}}{0.70\rho}} \quad , \tag{5.32}$$

and D_{11} can be obtained to be

$$D_{11} = \frac{E_L}{1-\mu_{LT}^2 \frac{E_T}{E_L}} \frac{t^3}{12} \quad , \tag{5.33}$$

where h is the thickness of the composite, the subscripts L and T represent the longitudinal and transverse directions, respectively, while

$$\mu_{LT} = -\mu_f V_f - \mu_m \left(1 - V_f\right) \quad , \tag{5.34}$$

where V represents the volume, and the subscripts f and m represent the fiber and matrix, respectively, μ_{LT} represents the Poisson's ratio for the NiTiNOL based composite as defined. The values of K_i equal 5.429 for the first mode, and 15.108 for the second mode (Mizar and Pryputniewicz, 2004). The modulus of elasticity for the polycarbonate matrix material was determined based on the resonant frequencies of a cantilever configuration of the material of the matrix.

5.2. Free lateral vibration of a prismatic cantilever beam

Consider a prismatic beam undergoing free lateral vibrations. The vibration occurs in one of the principle planes of flexure; the cross-sectional dimensions are small in comparison to the effective length of the beam. The term effective length refers to the active length of the beam undergoing free vibrations. The forces included are the external loading, the internal bending moment, which is the resultant moment of the normal stress distribution, and the internal shear force, which is the resultant of the shear stress distribution. From beam theory, the differential equation for the deflection can be written as

$$YI\frac{d^2u}{d^2y} = -M \quad , \tag{5.35}$$

where YI represents the flexural rigidity of the prismatic beam, I is the area moment of inertia, u is the displacement in the x-direction, and M is the moment.

The normal modes of vibrations are of primary interest and for a prismatic beam the deflection at any location can be represented by the following harmonic equation (Mizar, 1999):

$$y = X[A\cos(pt) + B\sin(pt)] \quad , \tag{5.36}$$

where $X = X(y)$ determines the shape of the normal mode of vibration under consideration and is called a normal function. Substituting Eq. 5.36 in Eq. 5.35 the partial differential equation can be rewritten as the following ODE:

$$\frac{d^4Y}{dy^4} = \frac{p^2}{a^2}X \quad , \tag{5.37}$$

where

$$\frac{p^2}{a^2} = \frac{p^2 A\rho}{YIg} = k^4 \quad , \tag{5.38}$$

and $\sin(ky)$, $\cos(ky)$, $\sinh(ky)$ and $\cosh(ky)$ represent particular solutions to Eq. 5.35 such that the general solution can be written as (Mizar, 1999)

$$X = C_1 \sin(ky) + C_2 \cos(ky) + C_3 \sinh(ky) + C_4 \cosh(ky) \quad . \tag{5.39}$$

In Eq. 5.39, the constants C_1, C_2, C_3, C_4 can be determined based on the conditions at the ends of the prismatic beam. Superimposing all possible normal modes, the general expression for the free lateral vibration can be written as (Mizar, 1999)

$$y = \sum_{i=1}^{i=\infty} X_i [A_i \cos(p_i t) + B_i \sin(p_i t)] \quad . \tag{5.40}$$

Applying appropriate boundary conditions for a cantilever beam, the non-trivial solution for Eq. 5.40 can be shown to be (Mizar et al., 1999)

$$\cos(k_i L)\cosh(k_i L) = -1 \qquad \text{for} \qquad i = 1, 2, \cdots \infty \quad . \tag{5.41}$$

The first four roots of Eq. 5.41, listed in Table 5.1, represent the first four bending modes of a prismatic beam, even though the number of roots to Eq. 5.41 are not limited to four (Mizar, 1999).

Table 5.1. Roots of the equation for the resonance frequencies.

i	$k_i L = \beta_i$
1	1.875
2	4.694
3	7.855
4	10.996

The frequencies of vibration of the modes of equation $k_i L = \beta_i$ are given by (Mizar, 1999)

$$f_i = \frac{\omega_i}{2 \cdot \pi} = \frac{a \cdot k_i^2}{2 \cdot \pi} \quad , \tag{5.42}$$

and

$$k_i = \frac{k_i \cdot L}{L} = \frac{\beta_i}{L} \quad . \tag{5.43}$$

The period of vibration is given by

$$\tau_i = \frac{1}{f_i} \quad . \tag{5.44}$$

Combining Equations 5.42 and 5.43 the resonant frequency for the first bending mode can be written as

$$f = \frac{1}{2\pi} \frac{h}{L^2} \sqrt{\frac{35\,E}{33\,\rho}} \quad , \tag{5.45}$$

where f is the resonant frequency of the NiTiNOL sample, h is the thickness, L is the active length, E is the modulus of elasticity, and ρ is the density. From Eq. 5.45 it is possible to obtain the modulus of elasticity, based on measured values of resonance frequency, as

$$E = \frac{132\pi^2 f^2 L^4 \rho}{35h^2} \quad . \tag{5.46}$$

A similar approach can be applied to a NiTiNOL based composite, in which NiTiNOL is used as the reinforcement in a metal or polymer matrix. However the mechanics is quite different and different analysis procedure has to be used.

SMA based composites refer to composites in which NiTiNOL fibers are embedded in a matrix material. The NiTiNOL fibers are placed in such a fashion that the stiffness of the composite material can be altered by addition of heat. One of the possible combinations is when the NiTiNOL fibers are placed on either side of the neutral axis of the matrix material. If the active strain energy tuning method (ASETM) is used to modify the dynamic characteristics of the structure, then the NiTiNOL fibers must be plastically elongated and placed in such a manner that they will be constrained from regaining their unstretched position upon application of heat. The fibers are heated by passing a current through them; as the fibers try to contract to their "normal" length, a uniformly distributed shear force is generated along the length of the fibers. This shear load affects bending of the composite structure in a predetermined fashion. However for the active modal modification technique (AMMT), the NiTiNOL need not be prestretched as a change in temperature will result in a change in stiffness of the composite. Transient and steady-state vibration control as well as active-buckling control are some of the many applications for SMA based composite materials. In this study, the NiTiNOL based composite manufactured at WPI, Fig. 5.1, was investigated for changes in its dynamic properties due to SME resulting from thermal activation of the NiTiNOL composite (Mizar and Pryputniewicz, 2003; 2004).

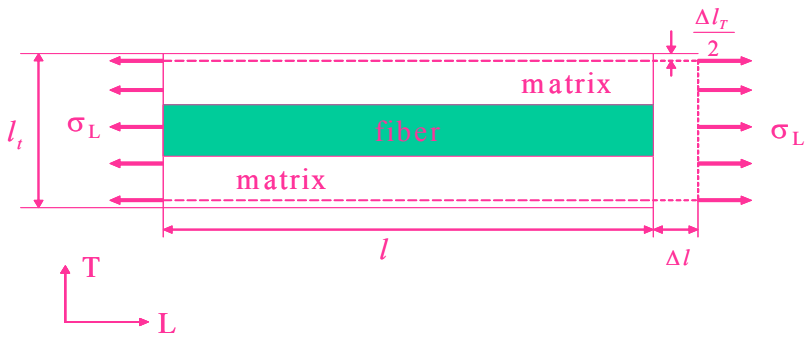

Fig. 5.1. Cross section of the NiTiNOL composite.

As shown in Fig. 5.1, NiTiNOL ribbons were embedded in a polymer matrix. To make this composite, slots were machined in the matrix material and the NiTiNOL ribbons with cross sectional dimensions of 0.84 mm by 0.17 mm were placed into them. The composite was clamped with boundary conditions of a cantilever plate. Using state-of-the-art OEH method, resonant frequency of the composite structure was determined. Using the analytical model temperature dependence of modulus of elasticity was determined in the tangential and longitudinal directions of the composite. The modulus of elasticity for the matrix material was also determined using the OEH method. The experimental measurements were used to monitor how the resonant frequency of the composite material changed as the NiTiNOL ribbons underwent phase transformation as the temperature increased. Analytical modeling focused on prediction of temperature dependence of the modulus of elasticity of the composite.

6. COMPUTATIONAL INVESTIGATIONS

6.1. Finite element method

The finite element method (FEM) is a computational method to solve engineering problems of various levels of complexity and diversity. In the FEM the volume of the component to be analyzed is discritized into a finite number of elements. The elements provide an approximation to the actual geometry of the component. The FEM constitutes standard steps for any engineering problem that can be listed as follows (Mizar, 1999):

1) *finite element discretization***:** the domain (geometry) is represented as a collection of a finite number of subdomains, namely elements. The collection of these finite elements is called the *finite element mesh*. The connectivity of the elements is achieved through *nodes*. When all the elements are of equal size, the mesh is of uniform size, otherwise the mesh is called a *non-uniform mesh*.
2) *element equations*: a typical element is isolated and its required (essential) properties are computed by some suitable predetermined means. Over each finite element, the physical process is approximated by functions of desired type, and algebraic equations relating physical quantities at specific nodes of the element are developed.
3) *assembly of element equations and solution*: assembly of element equations in an appropriate manner results in an accurate determination of the approximate solution sought. The degree of accuracy depends on the type of element(s)

used, the mesh density, and also on accurate input of essential properties of the elements constituting the mesh.

4) *convergence and error estimate*: an error associated with approximation of the domain is estimated by proving that the FEM solution converges to the actual solution (if known) in the limit $n \to \infty$, where *n* are the number of elements used in the finite element (FE) mesh. As the number of elements is increased, the approximation improves, i.e., the error in the approximation decreases. Increasing the number of elements results in an increase of the computational time and is very critical in solving complex, in particular non-linear engineering problems.

6.2. Finite element modeling of NiTi for modal analysis

The NiTiNOL ribbon investigated in this Dissertation has a rectangular cross section. Modeling for dynamic modal analysis consists of the following steps:

1) defining geometry of the specimen,
2) defining element groups, material properties, and boundary conditions,
3) meshing of the geometry of the specimen,
4) performing a check to determine any errors in input, before modal analysis,
5) modal analysis,
6) interpretation of results of the analysis.

Computational time for different mesh densities was determined to obtain optimal mesh density. Material properties determined from OEH were used as input, in particular, the modulus of elasticity. A 3D quadratic Langrange element was used for meshing the NiTiNOL specimen. This particular element was chosen based on convergence criteria. Modeling was conducted using FEMLAB® 3.2. (FEMLAB®, 2005) A mesh size of 360 elements was found appropriate by the convergence analysis, Fig. 6.1. The FEMLAB® code, developed in this Dissertation is listed in Appendix A. Resonance frequencies generated from the FEM analysis were compared to those from the OEH. The FEM analysis was conducted for three different lengths of the NiTi samples, and also at different temperatures ranging from -20ºC to 200ºC. Agreement between the FEM determined frequencies and those measured using OEH is good with differences well within the uncertainty limits. Figure 6.2 shows the meshed NiTiNOL sample of effective length of 29 mm for Eigenfrequency analysis in FEMLAB® 3.2.

6.3. Convergence of the FEM results

FEM is a computational technique and accuracy of the results obtained depends primarily on the input variables (geometry, material constants, type of mesh used, etc.). It is always possible to discretize a component by using more elements than needed. The results obtained in such a case will indeed be accurate, but will involve considerable computational times. It is, therefore, necessary for a convergence test to be performed to obtain the optimal mesh size for discretization of the component. In this Dissertation two

types of elements were used to test for convergence. Thin 4-noded shell elements and 8-20 noded, 3-dimensional solid elements. Results are presented for both types of elements for the first to fourth bending modes as a function of the number of elements used. Figure 6.1 gives the convergence plot using the 4-noded thin shell element for the first bending mode. A modulus of elasticity of 46.4 GPa and an effective length of 28.85 mm were used in the computational analysis. Results from all the four bending modes as a function of number of elements for shell and solid elements are summarized in Tables 6.1 and 6.2, respectively.

Similarly, FEM modeling was conducted for the NiTiNOL sample with an effective length of 28.82 mm and for a modulus of elasticity of 46.4 GPa using a solid element. The results obtained are indicated in Fig. 6.1.

From the convergence considerations, a mesh size of 360 elements was chosen for the computational analysis. As the sample was of uniform thickness, the mesh was constructed using thin shell 4-noded elements. Figure 6.2 shows the meshed object with appropriate boundary conditions, with the mesh comprising of 360 elements.

Table. 6.1. Summary of convergence test results for NiTiNOL using 4-noded shell elements.

ELEMENTS	10	40	90	160	250	360	490	640	810	1000
B1 (FEM)	290.8	291.3	291.3	291.2	291.2	291.2	291.2	291.2	291.2	291.2
B2 (FEM)	1818.9	1821.2	1821.2	1821	1821	1821	1820.5	1820.4	1820.3	1820.3
B3 (FEM)	5127.2	5094.7	5088.2	5085.2	5083.5	5082.5	5082	5081.3	5081	5081
B4 (FEM)	10220.1	9984.2	9946.6	9931.8	9924.5	9920.2	9917.4	9915.6	9914.2	9913.3

Table. 6.2. Summary of convergence test results for NiTiNOL using 8-noded solid elements.

ELEMENTS	10	40	90	160	250	360	490	640	810	1000
B1 (FEM)	290.8	291.3	291.3	291.2	291.2	291.2	291.2	291.2	291.2	291.2
B2 (FEM)	1818.9	1821.2	1821.2	1821	1821	1821	1820.5	1820.4	1820.3	1820.3
B3 (FEM)	5127.2	5094.7	5088.2	5085.2	5083.5	5082.5	5082	5081.3	5081	5081
B4 (FEM)	10220.1	9984.2	9946.6	9931.8	9924.5	9920.2	9917.4	9915.6	9914.2	9913.3

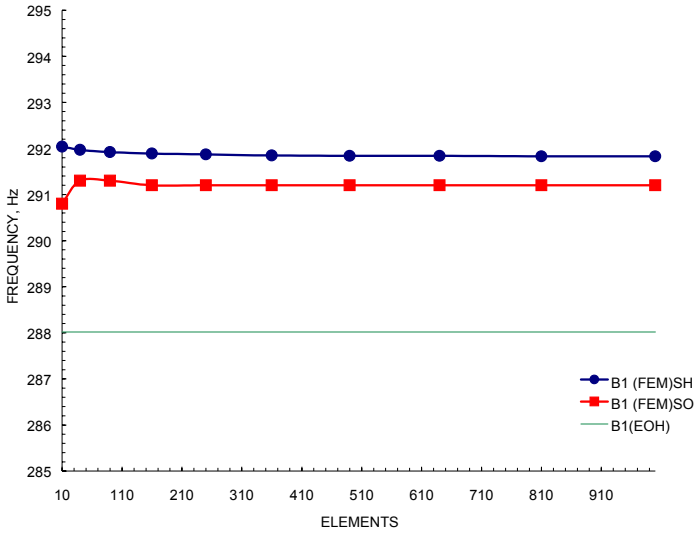

Fig. 6.1. Convergence test for NiTiNOL for the first bending using shell and solid elements.

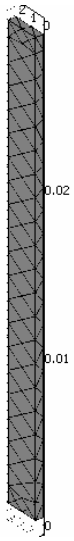

Fig. 6.2. Meshed NiTiNOL component with mesh size of 360 solid elements.

7. EXPERIMENTAL INVESTIGATIONS

7.1. Experimental considerations

The goal of this Dissertation was to experimentally detect phase transformation in the NiTiNOL sample by monitoring resonance frequency as a function of temperature for the first four bending modes. The NiTiNOL samples were heat treated to the temperature of 400°C for two hours (per recommendation by the manufacturer) in order to remove stresses, which were produced as a result of cold working of the material. Dynamic experiments were then conducted on the heat treated samples to obtain variation of the resonance frequencies of the first four bending modes as a function of temperature. The modulus of elasticity was determined from the measured frequencies.

7.2. Annealing techniques for NiTiNOL

A series of experiments were conducted to anneal the NiTiNOL samples at around 400ºC in steps of 3ºC to 4ºC. The purpose of the experiments was to determine the annealing temperature at which the NiTiNOL SMA was able to undergo the maximum SME and also to ensure that the TT was around 60ºC.

The apparatus for these measurements consisted of NiTiNOL samples in the form of strips 2.25 mm wide, 0.5 mm thick, and 25.4 mm long, a thermometer capable of accurately measuring temperatures above 150ºC, furnace to heat the NiTiNOL samples from 300ºC to 500ºC, a stainless steel slab with a groove to hold the deformed NiTiNOL samples while in the furnace, digital voltmeter, and a J type thermocouple to monitor

temperature.

The alloy was placed into a groove in the stainless steel slab. The sample as obtained from the manufacturer assumed a straight shape upon heating. The furnace temperature was set at 400ºC. The reading of the furnace was calibrated using a J type thermocouple. Then, the stainless steel slab was inserted into the furnace and was annealed for about 25 minutes. This time was necessary for steady-state conditions to be reached in the furnace. The NiTiNOL alloy would glow a dull red color once steady-state conditions have been reached within the furnace. The furnace was turned off after 25 minutes and allowed to cool with the door open. Also, the stainless steel slab was allowed to cool, and this process of cooling took about 2.5 hours.

After the NiTiNOL sample was cooled enough it was removed from the groove in the stainless steel slab. Pressure was put on the tip of the sample using pliers in order to bend it into the shape of an arc. Next, the NiTiNOL sample was heated using a heat gun to approximately 60ºC to make sure that the SMA had come back to its undeformed (straight) shape. In this particular case, the sample recovered only about 80% of the deformation imposed.

7.3. Measurement system

7.3.1. Fundamentals of holography

Holography is a technique which allows recording of the entire wavefront on a suitable recording medium. Recording the amplitude of the waves poses no problem

because the photosensitive media record amplitude by converting it to the corresponding variations in opacity of the 'sensing films'. The phase information is recorded by using the principle of interferometry (Vest, 1979; Pryputniewicz, 1996).

7.3.2. Techniques of hologram interferometry

Interferometry is a process in which two waves emitted from the same source, at the same time, interact with each other because of differences in their path lengths. As a result of this interaction, a pattern of alternating bright and dark fringes (bands) can be observed. These fringes relate directly to changes in the optical path lengths of either, or both, of the beams. Unfortunately, the coherence and monochromaticity of the light sources used in standard interferometers, prior to 1960, were poor. As a result of this, classical interferometry was limited to measurements of small path length differences of optically polished and specularly reflecting flat surfaces.

In the early 1960's, with the advent of a laser, holography has permitted to circumvent this shortcoming, in a very elegant manner, without any alterations, of course, of the fundamental principles. The method, based on the ability of a hologram to record the phase and amplitude of any wave at different states and to produce, during reconstruction, interference fringes relating to changes in these states, is known as *hologram interferometry* (Pryputniewicz, 1996). Hologram interferometry has allowed the extension of (classical) interferometry to three-dimensional diffusely reflecting objects with nonplaner surfaces.

There are three basic variations of hologram interferometry, each possessing certain advantages over the others in particular test situations:

1) *double-exposure hologram interferometry*,

2) *real-time hologram interferometry*, and

3) *time-average hologram interferometry*.

The time-average method can be further subdivided into

1) *stroboscopic time-average hologram interferometry*, and

2) *continuous time-average hologram interferometry*.

In *double-exposure technique*, two exposures of the object are made with the state of the object's stress changed between the two exposures. As a result of this, the object is slightly different during the second exposure when compared with its configuration during the first exposure. During reconstruction of the double-exposure hologram, the two object beams are faithfully reconstructed in phase and amplitude. Therefore, two three-dimensional images of the object are formed, corresponding to its initial and final positions, respectively.

Since both of these images are reconstructed in coherent light they are capable of interference with each other. Thus, in any region of space where the two reconstructed beams overlap, an image of the object is seen covered by a set of alternating bright and dark interference fringes - these are "frozen" fringes in that the fringe pattern is fixed and cannot be altered once it has been recorded. These fringes are called *cosinusoidal* because their brightness varies cosinusoidally across the image. The fringes seen during reconstruction of a hologram are a direct measure of the changes in the object's position

and/or shape, which has occurred between the two exposures. Obviously, a unique deformation of the object, for a given illumination and observation, does produce a unique three-dimensional interferogram within the hologram reconstruction. The only problem that now remains is to "decode" the information contained in the fringe pattern.

The *real-time method* consists of taking a single-exposure of an object in an unstressed state, processing the medium in place using the so-called liquid gate plate holder (or a photothermoplastic camera), and reconstructing a hologram using the identical coherent reference beam to the one used in the construction process. The reconstructed image is now superimposed onto the original object, which is also illuminated with the same light as when the hologram was recorded. Interference fringes can now be seen if the object is even slightly displaced. The interferometric comparison between the original state of the object, i.e., holographically reconstructed image, and the new state of the object is made at the instant it occurs. This comparison is manifested by a fringe pattern which is "live" in that it changes as the object's state of stress is changed. The particular advantage of the real-time method is that different types of motions, static as well as dynamic, can be studied with a single holographic exposure rather than having to make a hologram for each new position of the object.

The *stroboscopic time-average method* is really an extension of the double-exposure method, where the continuous wave (CW) laser beam is "chopped" into short pulses synchronized with the object vibration frequency. To effectively use this method, object vibration must be monitored continuously to assure proper characteristics of the illumination beam. This synchronization must be maintained over many vibration cycles,

to provide for sufficient exposure of the medium. Although interference fringes produced during reconstruction of stroboscopic holograms are cosinusoidal and are straightforward to analyze, the electronic apparatus, needed to produce good quality images may be complex and expensive, depending on the specific application.

In the *continuous time-average method* a single holographic recording of an object undergoing a cyclic vibration is made. With the (continuous) exposure time long in comparison to one period of the vibration cycle the hologram effectively records an ensemble of images corresponding to the time-average of all positions of the object during its vibration. While reconstructing such a hologram, the interference occurring between the entire ensemble of images, with the images recorded near zero velocity (i.e., maximum displacement) contributing most strongly to the reconstruction process, produces an interference pattern corresponding to the vibratory motion of the object. This fringe pattern is characterized by fringes of unequal brightness. In fact, they vary according to the square of the zero order Bessel function of the first kind (Pryputniewicz, 1987a). Therefore, fringes observed during reconstruction of the continuous time-average holograms are known as Bessel fringes.

7.3.3. Opto-electronic Holography (OEH)

Recent advances in the phase step hologram interferometry, speckle metrology, and computer technology allowed development of a system for direct electronic recording of holograms and transmission of holographic interferograms by television

systems for real-time display of interference fringes (Pryputniewicz, 1986, 1992). This opto-electronic holography (OEH) system, in addition to other electronic and optical components, consists of a modified speckle interferometer, which produces speckles large enough to be resolved by a TV camera. The output of the TV camera is fed to a system that computes and stores the magnitude and phase, relative to the reference beam, of each picture element in the image of the illuminated object (Pryputniewicz, 1990).

Any of the usual phenomena that generate characteristic fringes in hologram interferometry will do so in this process also, and the characteristic fringe functions will be impressed on the magnitudes of the values stored.

7.3.4. Fundamentals of OEH

Measurements of displacements of objects undergoing static and dynamic loads have been solved in a number of ways (Pryputniewicz, 1980, 1996). Recently, this problem has been addressed using advances in phase step hologram interferometry, speckle metrology, and computer technology. One of these ways is based on the method of OEH (Pryputniewicz, 1991).

Today, the displacement/deformation analysis of objects undergoing their static or dynamic loads are, to a great extent, satisfied by application of the finite element method (FEM) (Pryputniewicz, 1985). In these applications, the FEM is used to solve problems for which exact solutions do not exist, or are very difficult to obtain. Also, the FEM provides the only means to analyze complex three-dimensional structures, for which

response to the applied loads cannot be predicted by any other computational method. However, results obtained by the FEM depend on boundary conditions, rely greatly on accurate knowledge of material properties, depend on accurate representation of the structure's geometry, and are sensitive to the shape and the size of elements employed in modeling of the structure. All of the information necessary to run the finite element models can be obtained, directly or indirectly, from experimental studies (Kardestuncer and Pryputniewicz, 1987).

Currently, there are a number of experimental methods used to study displacement/deformation of objects. These methods are primarily based on the use of mechanical probes, strain gauges, and accelerometers and, in general, are invasive because they may affect the object's response to the load. In 1965, however, the method of hologram interferometry was invented (Powell and Stetson, 1965) and provided means by which holograms of objects could be readily recorded. However, quantitative interpretation of interference fringes has traditionally been tedious and prone to considerable inaccuracy. This has led to the use of heterodyne and phase step methods to read out the interferometric fringes produced during reconstruction of holograms of vibrating objects. Although these methods (Ineichen and Mastner, 1980; Stetson, 1970, 1982; Hariharan and Oreb, 1986; Pryputniewicz, 1988) allowed high accuracy, 1/1000 to 1/100 of one fringe, in measurements of local phase differences, they still required physical recording of a permanent hologram in some type of a photosensitive medium, which required lengthy processing. Therefore, these methods, which require lengthy processing, do not qualify for fully automated hologram analysis (Pryputniewicz, 1987b).

Recently, an automated method for processing of vibration fringes has been developed (Stetson and Brohinsky, 1988). In this method, measurements of irradiances produced by mutual interference of the object and reference fields are made electronically by a detector array. Processing of this interferometric information and display of the computational results are carried out concomitantly with measurements of irradiation. Because this method does not depend on recording of holograms in a conventional media, but rather relies on electronic acquisition, processing and display of optical interference information, it is called OEH, also referred to as electronic holography, or TV holography (Pryputniewicz, 1990). In the following sections, application of OEH to dynamic measurements is described.

The OEH method allows automated processing of fringes of statically and dynamically loaded objects (Stetson and Brohinsky,1987; Pryputniewicz and Stetson, 1989; Pryputniewicz, 1991). In this method, measurements of irradiances produced by mutual interference of the object and the reference fields are made electronically by a CCD camera, Fig. 7.1. Processing of this interferometric information and display of the computational results are carried out concomitantly with measurements of irradiation. The OEH method does not depend on recording of holograms in conventional media, but rather relies on electronic acquisition, processing, and display of optical interference information.

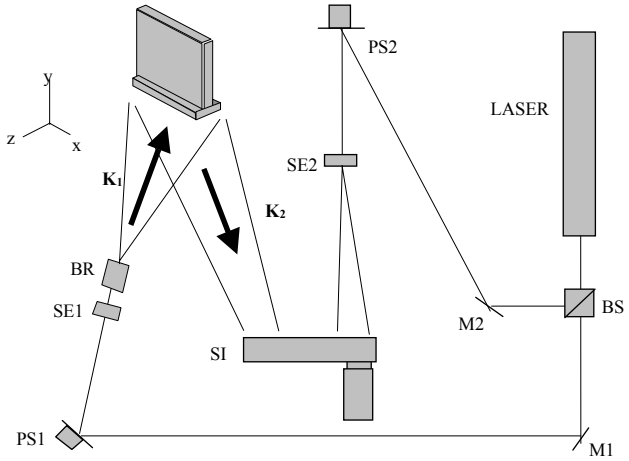

Fig. 7.1. The OEH system: BS is the beamsplitter, M1 and M2 are the mirrors, PS1 and PS2 are the phase steppers, SE1 and SE2 are the spatial filter beam expander assemblies BR is the object beam rotator, SI is the speckle interferometer, and $\mathbf{K_1}$ and $\mathbf{K_2}$ are the directions of illumination and observation vectors, respectively.

7.3.5. Electronic processing of holograms

The OEH system is capable of performing either static or dynamic measurements (Pryputniewicz, 1991, 1996). In the discussion that follows, static measurements are implemented using the double-exposure interferometry method, while dynamic measurements are implemented by the time-average method (Pryputniewicz, 1992, 1994b, 1996).

7.3.5.1. Static measurements

Static measurements are characterized by recording "single-exposure" holograms of an object at different states of stress. As a result of interference between a set of two

"single-exposure " holograms, fringes form, if there are any optical path differences between the corresponding points on the object as recorded in the two holograms.

In OEH, this process is carried out by recording sequential frames of images of the object corresponding to the two states of stress. Typically, four sequential frames are recorded, with a finite phase step-imposed on the reference beam - between each frame, for every single-exposure image of the object. In the following discussion, in order to simplify derivation of equations describing the OEH process for static measurements, the object will be initially unstressed; results would be the same if the object was stressed initially, but mathematics would be much more complicated (Pryputniewicz, 1994b).

The image of an unstressed (i.e., unloaded) object can be described by the irradiance distribution for the *n-th* sequential frame, $I_n(x,y)$, at the detector array of a CCD camera in the OEH system setup, as

$$I_n(x,y) = I_o(x,y) + I_r(x,y) + 2A_o(x,y)A_r(x,y)\cos\left[\Delta\phi(x,y) + \Delta\theta_n\right] \quad , \qquad (7.1)$$

while the corresponding image of the stressed (i.e., loaded) object can be described by the irradiance distribution, $I_n(x,y)$, as

$$I_n'(x,y) = I_o'(x,y) + I_r'(x,y) +$$

$$+2A_o'(x,y)A_r'(x,y)\cos[\Delta\phi(x,y) + \Omega(x,y) + \Delta\theta_n] \quad . \qquad (7.2)$$

In Eqs 7.1 and 7.2, *x* and *y* identify coordinates of the detectors in the array, I_o and I_r are the object and reference illumination fields, respectively, $\Delta\theta_n$ is the finite phase step imposed on the reference beam between the sequential frames recording

individual images, and Ω is the fringe-locus function, constant values of which define fringe loci on the surface of the object.

Since I and $I^{'}$ are measured at known coordinates *x* and *y*, Eqs 7.1 and 7.2 contain four unknowns, that is, irradiances (which are squares of the amplitudes) of the two fields, the phase difference between these fields, and the fringe-locus function. The goal of the analysis is to determine Ω because it is related directly to displacements and deformations of the object.

In OEH, $\Delta\phi$ is eliminated by recording sequentially four TV frames with an introduction of a 90^0 phase step between each frame. That is, $\Delta\theta_n$ appearing in Eqs 7.1 and 7.2 takes on the values of $0^0, 90^0, 180^0,$ and 270^0. This process can be represented by two sets of four simultaneous equations corresponding to Eqs 7.1 and 7.2, respectively, that is,

$$I_1 = I_o + I_r + 2A_oA_r\cos(\Delta\phi + 0^0) \quad , \tag{7.3}$$

$$I_2 = I_o + I_r + 2A_oA_r\cos(\Delta\phi + 90^0) \quad , \tag{7.4}$$

$$I_3 = I_o + I_r + 2A_oA_r\cos(\Delta\phi + 180^0) \quad , \tag{7.5}$$

$$I_4 = I_o + I_r + 2A_oA_r\cos(\Delta\phi + 270^0) \quad , \tag{7.6}$$

and

$$I_1^{'} = I_o^{'} + I_r + 2A_o^{'}A_r\cos(\Delta\phi + \Omega + 0^0) \quad , \tag{7.7}$$

$$I_2^{'} = I_o^{'} + I_r + 2A_o^{'}A_r\cos(\Delta\phi + \Omega + 90^0) \quad , \tag{7.8}$$

$$I_3^{'} = I_o^{'} + I_r + 2A_o^{'}A_r\cos(\Delta\phi + \Omega + 180^0) \quad , \tag{7.9}$$

$$I_4^{'} = I_o^{'} + I_r + 2A_o^{'}A_r \cos(\Delta\phi + \Omega + 270^0) \quad , \tag{7.10}$$

where the arguments (x, y) were omitted for simplification. Evaluation of Eqs 7.3 to 7.10 yields

$$I_1 = I_o + I_r + 2A_oA_r \cos\Delta\phi \quad , \tag{7.11}$$

$$I_2 = I_o + I_r + 2A_oA_r \sin\Delta\phi \quad , \tag{7.12}$$

$$I_3 = I_o + I_r - 2A_oA_r \cos\Delta\phi \quad , \tag{7.13}$$

$$I_4 = I_o + I_r - 2A_oA_r \sin\Delta\phi \quad , \tag{7.14}$$

and

$$I_1^{'} = I_o^{'} + I_r + 2A_o^{'}A_r \cos(\Delta\phi + \Omega) \quad , \tag{7.15}$$

$$I_2^{'} = I_o^{'} + I_r + 2A_o^{'}A_r \sin(\Delta\phi + \Omega) \quad , \tag{7.16}$$

$$I_3^{'} = I_o^{'} + I_r - 2A_o^{'}A_r \cos(\Delta\phi + \Omega) \quad , \tag{7.17}$$

$$I_4^{'} = I_o^{'} + I_r - 2A_o^{'}A_r \sin(\Delta\phi + \Omega) \quad . \tag{7.18}$$

It should be noted that systems of equations similar to Eqs 7.11 to 7.14 and Eqs 7.15 to 7.18 could be obtained using any value of the phase step, however, use of the 90^0 phase step results in the simplest computations.

Subtracting Eqs 7.11 and 7.13 as well as Eqs 7.12 and 7.14 we obtain, for the unstressed object, the following set of two equations:

$$\left(I_1 - I_3\right) = 4A_oA_r \cos\Delta\phi \quad , \tag{7.19}$$

and

$$\left(I_2 - I_4\right) = 4A_oA_r \sin\Delta\phi \quad . \tag{7.20}$$

Following the above procedure and subtracting Eqs 7.15 and 7.17 and Eqs 7.16 and 7.18, a set of two equations is obtained for the stressed object, that is,

$$\left(I_1^{'} - I_3^{'}\right) = 4A_o^{'}A_r \cos(\Delta\phi + \Omega) \quad , \tag{7.21}$$

and

$$\left(I_2^{'} - I_4^{'}\right) = 4A_o^{'}A_r \sin(\Delta\phi + \Omega) \quad . \tag{7.22}$$

Addition of Eqs 7.19 and 7.21 yields

$$\left(I_1 - I_3\right) + \left(I_1^{'} - I_3^{'}\right) = 4A_oA_r \cos\Delta\phi + 4A_o^{'}A_r \cos(\Delta\phi + \Omega) \quad . \tag{7.23}$$

Because object displacements and deformations are small, it can be assumed that $A_o^{'} \approx A_o$. Therefore, Eq. 7.23 becomes

$$\left(I_1 - I_3\right) + \left(I_1^{'} - I_3^{'}\right) = 4A_oA_r\left[\cos\Delta\phi + \cos(\Delta\phi + \Omega)\right] \quad . \tag{7.24}$$

Recognizing that $\cos(\Delta\phi + \Omega) = \cos\Delta\phi\cos\Omega - \sin\Delta\phi\sin\Omega$, Eq. 7.24 can be written as

$$D_1 = \left(I_1 - I_3\right) + \left(I_1^{'} - I_3^{'}\right) = \tag{7.25}$$

$$= 4A_oA_r\left[\left(1 + \cos\Omega\right)\cos\Delta\phi - \sin\Delta\phi\sin\Omega\right] \quad .$$

In a similar way, addition of Eqs 7.20 and 7.22 simplifies to

$$D_2 = \left(I_2 - I_4\right) + \left(I_2^{'} - I_4^{'}\right) =$$

$$= 4A_oA_r\left[\left(1 + \cos\Omega\right)\sin\Delta\phi + \cos\Delta\phi\sin\Omega\right] \quad . \tag{7.26}$$

Finally, addition of the squares of Eqs 7.25 and 7.26 yields

$$D_1^2 + D_2^2 = \left\{4A_oA_r\left[\left(1 + \cos\Omega\right)\cos\Delta\phi - \sin\Delta\phi\sin\Delta\phi\right]\right\}^2 +$$

$$+\left\{4A_oA_r\left[\left(1+\cos\Omega\right)\sin\Delta\phi+\cos\Delta\phi\sin\Omega\right]\right\}^2 \quad , \tag{7.27}$$

which reduces to

$$D_1^2+D_2^2=16A_o^2A_r^2\left[\left(1+\cos\Omega\right)^2+\sin^2\Omega\right] \quad . \tag{7.28}$$

From Eq. 7.28 we obtain

$$D_1^2+D_2^2=32A_o^2A_r^2\left(1+\cos\Omega\right) \quad . \tag{7.29}$$

Furthermore, recognizing that $\left(1+\cos\Omega\right)=2\cos^2\left(\frac{\Omega}{2}\right)$, Eq. 7.29 can be reduced to

$$\sqrt{\left(D_1^2+D_2^2\right)}=8A_oA_r\cos\left(\frac{\Omega}{2}\right) \quad , \tag{7.30}$$

which represents the static viewing image displayed by the OEH. In Eq. 7.30, Ω is the fringe-locus function corresponding to the static displacements and/or deformations of the object. The fringe-locus function can be determined by processing the sequential OEH images as described below.

In order to obtain data from the OEH images, we will again employ Eqs 7.19 to 7.22 and follow the procedure used to derive Eq. 7.29. The result of this procedure is

$$D_3=\left(I_1-I_3\right)-\left(I_1^{'}-I_3^{'}\right)=$$

$$=4A_oA_r\left[\left(1-\cos\Omega\right)\cos\Delta\phi+\sin\Delta\phi\sin\Omega\right] \quad , \tag{7.31}$$

$$D_4=\left(I_2-I_4\right)-\left(I_2^{'}-I_4^{'}\right)=$$

$$=4A_oA_r\left[\left(1-\cos\Omega\right)\sin\Delta\phi-\cos\Delta\phi\sin\Omega\right] \quad , \tag{7.32}$$

and

$$D_3^2 + D_4^2 = 32 A_o^2 A_r^2 \left(1 - \cos\Omega\right) \quad . \tag{7.33}$$

Subtracting Eq. 7.33 from Eq. 7.29 we obtain

$$D = \left(D_1^2 + D_2^2\right) - \left(D_3^2 + D_4^2\right) =$$

$$= 32 A_o^2 A_r^2 \left(1 + \cos\Omega\right) - 32 A_o^2 A_r^2 \left(1 - \cos\Omega\right) \quad . \tag{7.34}$$

or

$$D = 64 A_o^2 A_r^2 \cos\Omega \quad . \tag{7.35}$$

Starting with Eqs 7.19 to 7.22, we can also determine

$$N_1 = \left(I_1 - I_3\right) + \left(I_2^{'} - I_4^{'}\right) =$$

$$= 4 A_o A_r \left[\left(1 + \sin\Omega\right)\cos\Delta\phi + \sin\Delta\phi\cos\Omega\right] \quad , \tag{7.36}$$

$$N_2 = \left(I_2 - I_4\right) + \left(I_1^{'} - I_3^{'}\right) =$$

$$= 4 A_o A_r \left[\left(1 + \sin\Omega\right)\sin\Delta\phi - \cos\Delta\phi\cos\Omega\right] \quad , \tag{7.37}$$

$$N_3 = \left(I_1 - I_3\right) + \left(I_2^{'} - I_4^{'}\right) =$$

$$= 4 A_o A_r \left[\left(1 - \sin\Omega\right)\cos\Delta\phi - \sin\Delta\phi\cos\Omega\right] \quad , \tag{7.38}$$

$$N_4 = \left(I_2 - I_4\right) + \left(I_1^{'} - I_3^{'}\right) \quad ,$$

$$= 4 A_o A_r \left[\left(1 - \sin\Omega\right)\sin\Delta\phi + \cos\Delta\phi\cos\Omega\right] \quad , \tag{7.39}$$

$$N_1^2 + N_2^2 = 32 A_o^2 A_r^2 \left(1 + \sin\Omega\right) \quad , \tag{7.40}$$

$$N_3^2 + N_4^2 = 32 A_o^2 A_r^2 \left(1 - \sin\Omega\right) \quad , \tag{7.41}$$

and

$$N = \left(N_1^2 + N_2^2\right) - \left(N_3^2 + N_4^2\right) = 64 A_o^2 A_r^2 \sin\Omega \quad . \tag{7.42}$$

Finally, dividing Eq. 7.42 by Eq. 7.35, we obtain

$$\frac{N}{D} = \frac{64 A_o^2 A_r^2 \sin\Omega}{64 A_o^2 A_r^2 \cos\Omega} \tag{7.43}$$

from which it follows that

$$\Omega = \tan^{-1}\left(\frac{N}{D}\right) \quad . \tag{7.44}$$

It should be noted that Ω, computed from Eq. 7.44, is a spatial function that depends on coordinates *x* and *y*. Therefore, its values are determined for every coordinate pair *(x,y)* in the object space. Once the values of Ω are determined, they can be used to compute object displacements (Pryputniewicz, 1994b).

7.3.5.2. Dynamic measurements

In this section, application of OEH to dynamic measurements is made based on time-average hologram interferometry. To facilitate this presentation, time-average recording of a sinusoidally vibrating object will be considered (Pryputniewicz and Stetson, 1989). For this case, the irradiance distribution for the *n*-th sequential frame, I_{tn}, can be represented by a relationship similar to those shown in Eqs 7.1 and 7.2 (Pryputniewicz, 1996), that is,

$$I_{t_n} = I_{t_o} + I_r + 2 A_{t_o} A_r \cos\left(\Delta\phi_t + \Delta\theta_n\right) M\left(\Omega_t\right) \quad . \tag{7.45}$$

In Eq. 7.45, the arguments *(x,y)* were omitted for simplification, subscript *t* indicates time varying parameters, *M* is the characteristic function that modulates the interference of the two fields due to the motion of the object, Ω_t is the fringe-locus function defining fringe loci on the surface of a vibrating object, and other parameters are as defined for Eqs 7.1 and 7.2.

Equation 7.45, like Eqs 7.1 and 7.2, has four unknowns: I_{t_o} and I_r, which are squares of A_{t_o} and A_r, respectively, $\Delta\phi_t$, and Ω_t. The goal of the analysis is to determine Ω_t because it relates directly to the displacements of the vibrating object (Pryputniewicz, 1994b).

In order to determine Ω_t from the electronic holograms of a vibrating object, four sequential frames are recorded with the phase steps equal to multiples of 90^0 imposed on the reference beam between each frame. This process can be represented by the following set of four simultaneous equations:

$$I_{t_1} = I_{t_o} + I_r + 2A_{t_o}A_r \cos\left(\Delta\phi + 0^0\right) M\left(\Omega_t\right) \quad , \tag{7.46}$$

$$I_{t_2} = I_{t_o} + I_r + 2A_{t_o}A_r \cos\left(\Delta\phi + 90^0\right) M\left(\Omega_t\right) \quad , \tag{7.47}$$

$$I_{t_3} = I_{t_o} + I_r + 2A_{t_o}A_r \cos\left(\Delta\phi + 180^0\right) M\left(\Omega_t\right) \quad , \tag{7.48}$$

$$I_{t_4} = I_{t_o} + I_r + 2A_{t_o}A_r \cos\left(\Delta\phi + 270^0\right) M\left(\Omega_t\right) \quad . \tag{7.49}$$

Following the procedure used to derive Eqs 7.19 and 7.20 and operating on Eqs 7.46 to 7.49, we obtain

$$I_{t_1} = I_{t_o} + I_r + 2A_{t_o}A_r \cos\left(\Delta\phi_t\right) M\left(\Omega_t\right) \quad , \tag{7.50}$$

$$I_{t_2} = I_{t_o} + I_r + 2A_{t_o}A_r \sin\left(\Delta\phi_t\right) M\left(\Omega_t\right) \quad , \tag{7.51}$$

$$I_{t_3} = I_{t_o} + I_r - 2A_{t_o}A_r \cos\left(\Delta\phi_t\right) M\left(\Omega_t\right) \quad , \tag{7.52}$$

$$I_{t_4} = I_{t_o} + I_r - 2A_{t_o}A_r \sin\left(\Delta\phi_t\right) M\left(\Omega_t\right) \quad . \tag{7.53}$$

Then, from Eqs 7.50 to 7.53, it follows that

$$I_{t_1} - I_{t_3} = 4A_{t_o}A_r \cos\left(\Delta\phi_t\right) M\left(\Omega_t\right) \quad , \tag{7.54}$$

and

$$I_{t_2} - I_{t_4} = 4A_{t_o}A_r \sin\left(\Delta\phi_t\right) M\left(\Omega_t\right) \quad . \tag{7.55}$$

If the viewing mode is selected, then, based on the input described by Eqs 7.54 and 7.55, the OEH system produces an image that can be represented by

$$\sqrt{\left(I_{t_1} - I_{t_3}\right)^2 + \left(I_{t_2} - I_{t_4}\right)^2} = 4A_oA_rM\left(\Omega_t\right) \quad . \tag{7.56}$$

The image represented by Eq. 7.56 is displayed live on a TV monitor and can be stored in the processor memory (Pryputniewicz, 1994b).

This storage can be of two types. If the image is to be recalled in the future for visual observation, then an 8-bit image is stored and occupies approximately one-quarter megabyte of memory - this is the *image storage*. If the image is to be processed quantitatively, then the lookup table for the data mode is loaded into the operating system and produces a data image which can be represented by

$$\left(I_{t_1} - I_{t_3}\right)^2 + \left(I_{t_2} - I_{t_4}\right)^2 = 16I_oI_rM^2\left(\Omega_t\right) \quad . \tag{7.57}$$

The result shown in Eq. 7.57 is stored as a 16-bit data image and occupies one-half megabyte of memory – this is the *data storage*. Either type of image may then be downloaded to the host computer's memory for further processing.

Equations 7.56 and 7.57 indicate that the viewing and the data images are proportional to the characteristic function and to the square of the characteristic function, respectively. The characteristic function is determined by the temporal motion of the object, and for sinusoidal vibrations, assuming that the vibration period is much shorter than the TV framing time,

$$M\left[\Omega_t(x,y)\right] = J_o\left[\left|\Omega_t(x,y)\right|\right] \quad , \tag{7.58}$$

where J_o is the zero-order Bessel function of the first kind. Therefore, Eqs 7.56 and 7.57 become

$$\sqrt{\left(I_{t_1} - I_{t_3}\right)^2 + \left(I_{t_2} - I_{t_4}\right)^2} = 4A_o A_r J_o\left[\left|\Omega_t(x,y)\right|\right] \quad , \tag{7.59}$$

and

$$\left(I_{t_1} - I_{t_3}\right)^2 + \left(I_{t_2} - I_{t_4}\right)^2 = 16A_o A_r J_o^2\left[\left|\Omega_t(x,y)\right|\right] \quad , \tag{7.60}$$

respectively. Equation 7.59 results in a viewed image that is modulated by a system of fringes described by the zero-order Bessel function of the first kind, while Eq. 7.60 shows that the data image is modulated by the square of this function (Pryputniewicz, 1994b). Thus, centers of the dark fringes are located at those points on the surface of the object where $J_o\left[\left|\Omega_t\right|\right]$ equals zero, as shown in Fig. 7.2. This figure indicates that the zero-order fringe is much brighter than the other J_o fringes. Since the zero-order fringes represent

the stationary points on the vibrating object they allow easy identification of nodes (Pryputniewicz, 1987a). The brightness of other fringes decreases with increasing fringe orders and can be directly related to the mode shapes (Pryputniewicz, 1996). It should be noted that higher order zeros are nearly equally spaced giving the J_o function an almost periodic nature that is utilized in quantitative interpretation of images recorded by the OEH system.

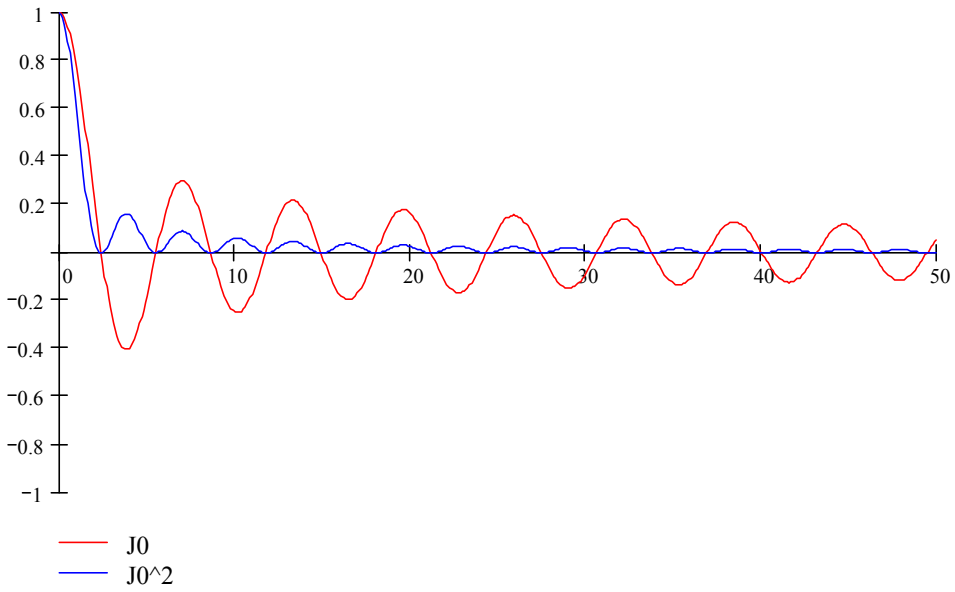

Fig. 7.2. The zero order Bessel function and its square, defining locations of centers of dark fringes seen during reconstruction of the time-average holograms of vibrating objects.

In the OEH system, the data provided by the CCD camera are processed to produce results represented by Eq. 7.59, for every pixel in the image frame, at the rate of 30 frames per second (fps). Each frame contains 512*480 8-bit numbers so that each

image consists of 245,760 points. For visual examination of the vibration modes, time-average hologram images corresponding to Eq. 7.59 are displayed on a TV monitor. These images are generated concomitantly by the pipeline processor of the OEH system. To produce data suitable for quantitative analysis of time-average holograms, 16-bit images represented by Eq. 7.60 are stored. These data are stored in two 8-bit bytes per pixel and produce a frozen image that can be displayed on the TV monitor one byte at a time, that is, either as a high-byte image or a low-byte image.

7.3.5.3. Determination of the fringe-locus function for a vibrating object

To interpret electronically recorded time-average holograms quantitatively, the argument of the J_o^2 function, appearing in Eqs 7.59 and 7.60, must be determined. One method to determine this argument, suitable for the time-average holograms recorded by OEH, was developed by Stetson and Brohinsky (1988). This method uses the fact that it is possible to shift J_o fringes in a manner similar to that in which phase modulation shifts cosinusoidal fringes in conventional double-exposure hologram interferometry. In time-average holography, this is done by modulating the phase of either the object or the reference beams sinusoidally at the same frequency and phase as the object vibration. Such a process is represented mathematically by addition of a phasor bias B, to the argument of the Bessel function, resulting in the characteristic function

$$M\left[\Omega_t(x,y),B\right]=J_o\left[\left|\Omega_t(x,y)-B\right|\right] \quad . \tag{7.61}$$

For purposes of analysis, the object must be made to vibrate in only one vibration mode at a time so that the motions of its various parts are either in or out of phase with one another. If the phase of the sinusoidal beam modulation is adjusted to coincide with that of the object vibration, the phasor bias becomes a simple additive term within the argument of the Bessel function, that is,

$$M\left[\Omega_t(x,y),B\right]=J_o\left[\left|\Omega_t(x,y)-B\right|\right] \quad . \tag{7.62}$$

Therefore, Eq. 7.60 becomes

$$\left[I_1(x,y)-I_3(x,y)\right]^2+\left[I_2(x,y)-I_4(x,y)\right]^2=$$

$$=16I_o(x,y)I_r(x,y)J_o^2\left[\left|\Omega_t(x,y)-B\right|\right] \quad . \tag{7.63}$$

For comparison, general equation representing the irradiance, I_{h_t}, of an image reconstructed from a time-average hologram is

$$I_{h_t}(x,y)=I_{a_t}(x,y)+I_{m_t}(x,y)J_o^2\left[\left|\Omega_t(x,y)-B\right|\right] \quad , \tag{7.64}$$

where I_{a_t} represents local average background irradiance from scattered light and I_{m_t} is the local maximum irradiance. Therefore, Eq. 7.63 is the special case of Eq. 7.64 with

$$I_{h_t}(x,y)=\left[I_1(x,y)-I_3(x,y)\right]^2+\left[I_2(x,y)-I_4(x,y)\right]^2 \quad , \tag{7.65}$$

$$I_{a_t}(x,y)=0 \quad , \tag{7.66}$$

and

$$I_{m_t}(x,y)=16I_o(x,y)I_r(x,y) \quad . \tag{7.67}$$

Output of the processor in the data mode, I_{h_t}, is stored in the host computer for different values of B, while I_{a_t}, I_{m_t}, and Ω_t constitute three unknowns, and the goal of the analysis is to determine Ω_t. Unfortunately, the Bessel function is not separable in terms of Ω_t and B, so a straightforward solution is not possible. However, the nearly periodic nature of the J_o function allows an approximate solution for the fringe locus function. This approximate solution recognizes that Eq. 7.64 is similar to the general equation for the irradiance distribution I_h for an image constructed from a conventional double-exposure hologram with cosinusoidal fringes, that is,

$$I_h(x,y) = I_a(x,y) + I_m(x,y)\cos^2\left[\Omega(x,y) - B\right] \quad , \tag{7.68}$$

where J_o^2 in Eq. 7.64 has been replaced by $\cos^2$, and Ω_t^2 has been replaced by Ω.

Examination of Eq. 7.68 shows that it, just like Eq. 7.65, also has three unknowns: I_a, I_m, and Ω. However, the $\cos^2\left[\Omega(x,y) - B\right]$ term, appearing in Eq. 7.68, unlike the $J_o^2\left[\left|\Omega_t(x,y) - B\right|\right]$ term of Eq. 7.65, is separable in its component arguments. To facilitate solution for Ω, Eq. 7.64 in rewritten as

$$I_h(x,y) = I_a(x,y) + I_m(x,y)\cos\left[2\Omega(x,y) - 2B\right] \quad , \tag{7.69}$$

where

$$I_a(x,y) = I_a(x,y) + \frac{I_m(x,y)}{2} \quad , \tag{7.70}$$

and

$$I_m(x,y) = \frac{I_m(x,y)}{2} \quad . \tag{7.71}$$

With three values of B, three simultaneous equations of the type of Eq. 7.69 can be solved uniquely for Ω. The three simultaneous equations are

$$I_{h_1}(x,y) = I_a(x,y) + I_m(x,y)\cos\left[2\Omega(x,y)\right] \quad , \tag{7.72}$$

$$I_{h_2}(x,y) = I_a(x,y) + I_m(x,y)\cos\left[2\Omega(x,y) - 2B\right] \quad , \tag{7.73}$$

and

$$I_{h_3}(x,y) = I_a(x,y) + I_m(x,y)\cos\left[2\Omega(x,y) + 2B\right] \quad , \tag{7.74}$$

corresponding to the zero, positive, and negative shifts, respectively. Solution of Eqs 7.72 to 7.74 yields (Pryputniewicz, 1996)

$$\Omega(x,y) = \frac{1}{2}\tan^{-1}\left\{\left[\frac{1-\cos(2B)}{\sin(2B)}\right]\frac{I_{h_3}(x,y) - I_{h_2}(x,y)}{2I_{h_1}(x,y) - I_{h_2}(x,y) - I_{h_3}(x,y)}\right\} \quad . \tag{7.75}$$

If the three irradiance distributions $I_{h_{t1}}(x,y)$, $I_{h_{t2}}(x,y)$, and $I_{h_{t3}}(x,y)$, corresponding to the three time-average holograms, are substituted into Eq. 7.75 the result is $\Omega_{t_{approx}}(x,y)$. This value of $\Omega_{t_{approx}}(x,y)$ differs from the correct argument, Ω_t, of the J_o function, because of inequality between the J_o^2 and $\cos^2$ functions, and should be expressed as

$$\Omega_{t_{approx}}(x,y) = \Omega_t(x,y) + \varepsilon(x,y) \quad . \tag{7.76}$$

Equation 7.76 yields values of $\Omega_{t_{approx}}$ modulo 180º. By adding or subtracting 180º, depending on the sign of the numerator in Eq. 7.75, whenever the denominator is negative $\Omega_{t_{approx}}$ can be obtained modulo 360^0. The image can be searched by the computer to locate discontinuities to define areas where the missing multiples of the

360^0 should be added to unwrap function $\Omega_{t_{approx}}$. By further identifying pixels within the zero-order fringe, an overall level shift can be applied to make those pixels have values between $\pm 180^0$ (Pryputniewicz, 1996).

Errors ε can be computed for any value of Ω_t for specific values of B to generate a lookup table. This lookup table is used to correct the values computed from Eq. 7.75 that have been unwrapped and level shifted. In this way, vibratory deformations can be obtained from time-average hologram reconstructions with little more mathematical computation than is required for static deformations. Once the correct values of Ω_t are determined, they can be used in any one of the equations for quantitative interpretation of time-average holograms.

7.3.5.4. Generation of a lookup table

A lookup table is computed from Eqs 7.75 and 7.76. First, three values of I_{h_t} are computed by using Eq. 7.64 for three values of B, for example, 0 and $\pm\frac{\pi}{3}$, that is,

$$I_{h_{t1}}(x,y) = I_{a_t}(x,y) + I_{m_t}(x,y) J_o^2\left[\left|\Omega_t(x,y)\right|\right] \quad , \tag{7.77}$$

$$I_{h_{t2}}(x,y) = I_{a_t}(x,y) + I_{m_t}(x,y) J_o^2\left[\left|\Omega_t(x,y)\right|\right] \quad , \tag{7.78}$$

$$I_{h_{t3}}(x,y) = I_{a_t}(x,y) + I_{m_t}(x,y) J_o^2\left[\left|\Omega_t(x,y)\right|\right] \quad . \tag{7.79}$$

Substitution of the values of Eqs 7.77, 7.78, and 7.79 into Eq. 7.75 yields

$$\Omega_{t_{approx}}(x,y)=\frac{1}{2}\tan^{-1}\left\{\left[\frac{1-\cos(2B)}{\sin(2B)}\right]\frac{J_0^2(\Omega_t+B)-J_0^2(\Omega_t-B)}{2J_0^2(\Omega_t)-J_0^2(\Omega_t-B)-J_0^2(\Omega_t+B)}\right\} \quad . \tag{7.80}$$

To construct the lookup table corresponding to a specific value of *B*, Eq. 7.80 is used to compute $\Omega_{t_{approx}}$ for a designed range of values of Ω_t. Tabulating Ω_t versus $\Omega_{t_{approx}}$ produces the lookup table for the given value of the bias vibration. If the magnitude of phase modulation of the bias vibration changes new lookup table must be constructed.

7.3.6. OEH system and procedure

7.3.6.1. Description of the system

The electronic and optical configurations of the OEH system are shown in Figs 7.1 and 7.3, respectively.

In the OEH system, the laser output is divided into two beams by means of a continuously variable beamsplitter, Fig. 7.1. One of these beams is directed via a piezoelectrically driven mirror and is shaped by the spatial filter beam expander assembly to illuminate the object uniformly; this mirror can be driven at the same frequency as the object excitation to provide bias vibration. The other beam, also spatially filtered and expended, is directed toward the reference input of the speckle interferometer by another piezoelectrically driven mirror that introduces 90^0 phase steps between consecutive

frames. The speckle interferometer combines the object beam with the reference beam and directs them collinearly toward the detector array of the CCD camera.

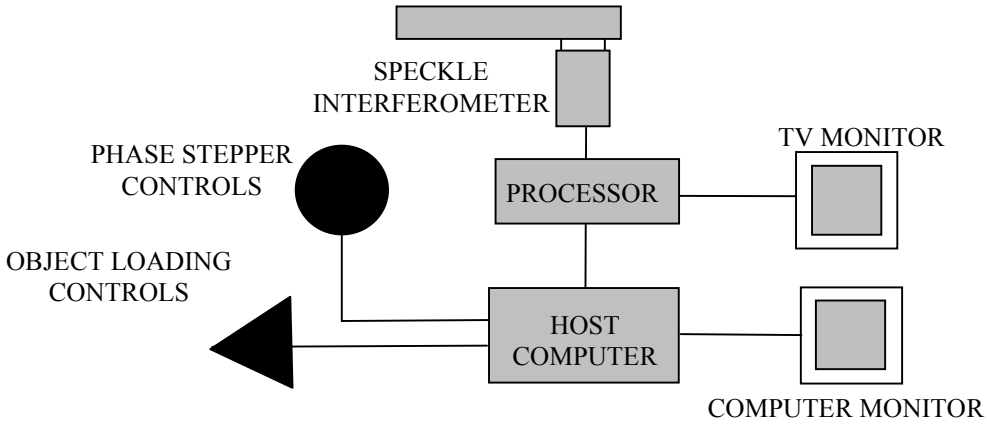

Fig. 7.3. Electronic configuration of the OEH system.

In the OEH system, the CCD camera detects the interference pattern and sends it to the pipeline processor, Fig 7.3. All computations are done in a pipeline processor, which operates under control of a host computer. The host computer also controls excitation of the object, coordinates it with the bias vibration imposed on the object, and keeps track of the 90^0 phase stepping between the frames.

By operating on each input image and its three predecessors, the pipeline processor produces a hologram, and this hologram is viewed concomitantly on the TV monitor. Such holograms are produced for the zero, as well as the positive and negative bias vibration, for each resonance frequency of the object. The three resulting electronic holograms are then processed by the host computer to determine spatial distribution of the displacement vectors that can be viewed directly on the computer monitor.

7.3.7. Configuration of the system

Configuration of the OEH system used in this Dissertation is shown in Fig. 7.4. In the OEH system, the laser output is divided into two beams by means of a continuously variable beamsplitter, Fig. 7.4. One of these beams is directed via a piezoelectrically (PZT) driven mirror and is shaped by the spatial filter beam expander (SFBE) assembly to illuminate the object uniformly. The other beam, also spatially filtered and expended, is directed toward the reference input of the speckle interferometer by another piezoelectrically driven mirror that introduces 90^0 phase steps between consecutive frames. The speckle interferometer combines the object beam with the reference beam and directs them collinearly toward the detector array of the CCD camera.

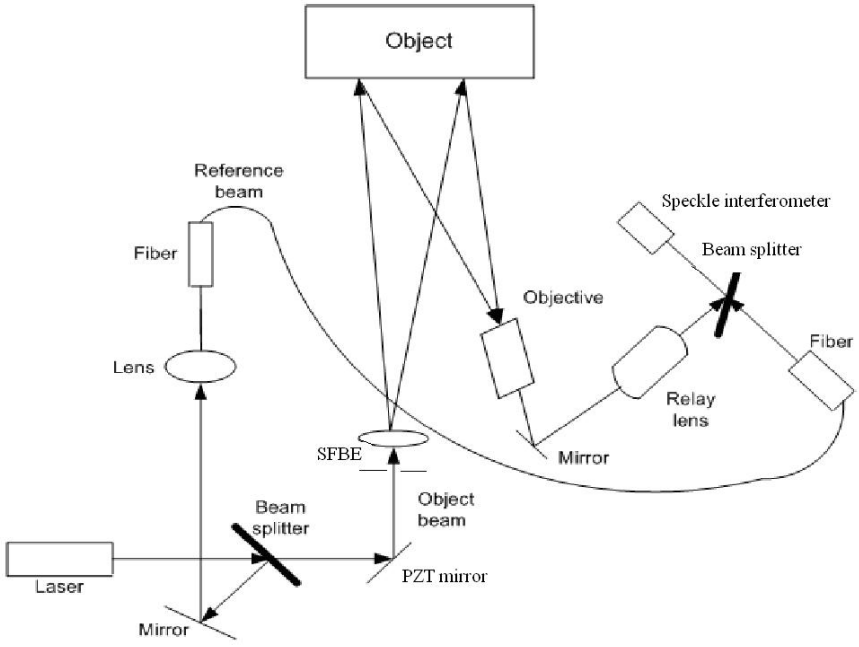

Fig. 7.4. Configuration of the OEH system used in this Dissertation.

In the OEH system, the CCD camera which is a part of the speckle interferometer assembly, detects the interference pattern and sends it to a processor. In the processor, the sequential frames are processed. All computations are done in the processor, which operates under control of a host computer. The host computer also controls excitation of the object, coordinates it with the bias vibration imposed on the object, and keeps track of the 90^0 phase stepping between the frames.

The phase shifted images recorded by the camera are stored in the computer. The computer performs the mathematical operations and the wrapped image that contains the phase and deformation information is displayed. After applying appropriate unwrapping algorithms, the resultant unwrapped image can be obtained. After appropriate scaling, it is possible to obtain deformation of the object under either static or dynamic loading conditions (Pryputniewicz and Stetson, 1989; Pryputniewicz, 1991).

7.3.8. OEH investigations

OEH was used for the determination of the modulus of elasticity of NiTiNOL from the resonance frequencies measured. Using this method, the mode shapes corresponding to the first four bendings were visualized and the corresponding frequencies recorded. The NiTi samples mounted in a cantilever configurations, were excited using a PZT shaker. Care was taken to use a base that consisted of flat surfaces, to ensure “fixed“ boundary conditions. Three different lengths were used in the experiments, and for each

sample the resonance frequencies were determined when temperature ranged from –20ºC to 200ºC.

The experimental setup used is shown in Fig. 7.5. The environmental chamber (EC) was used to cycle the NiTiNOL sample from –20ºC to 200ºC. The interferograms were obtained through the OEH system, Fig. 7.5. A frequency doubled YAG laser (LS) with a wavelength of 514 nm (1nm = 10^{-9} m) was used for illuminating the samples. The dynamic stiffness of the NiTiNOL based composites was also determined in a similar manner using the OEH. The composites had boundary conditions of a cantilever plate. Resonant frequencies were measured and the dynamic stiffness was calculated from the resonant frequencies. The dynamic stiffness was obtained for temperatures ranging from 20°C to 150°C. A narrower temperature range was used for the composite in order to prevent softening of the polymide matrix (NiTiNOL-polymide composite), and the same range was used for uniformity in measurement range for the NiTiNOL-Al composite.

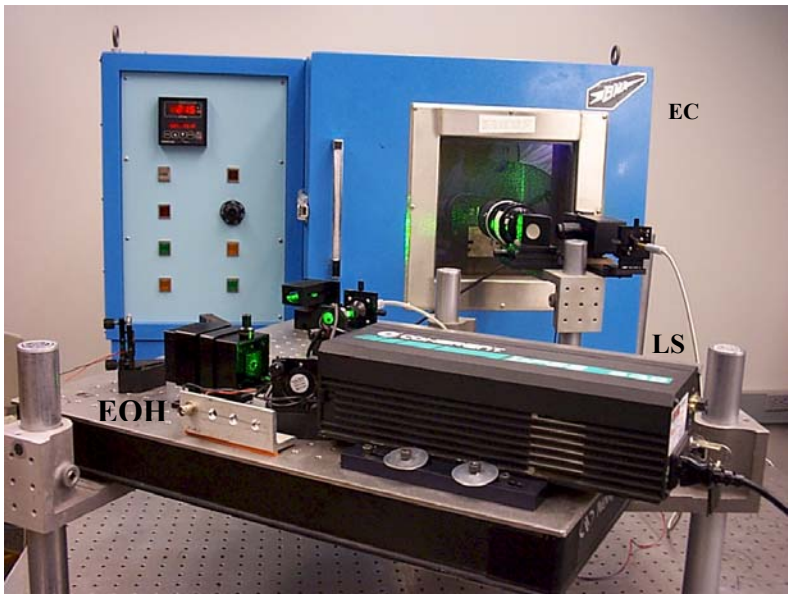

Fig. 7.5. OEH setup for the measurement of resonant frequencies.

7.4. Manufacturing the NiTiNOL based composite

The NiTiNOL composites were manufactured using the state-of-the-art CAD/CAM facilities at WPI. Figure 7.6 shows the composite being machined using the HAAS® CNC machining center (Hass®, 2001). Appendix B lists the G-code that was used to manufacture the NiTiNOL based composites. Appendix C provides a screenshot capture from GIBBSCAM®. This software is used to simulate and validate the G-code in order to efficiently, and accurately machine the component.

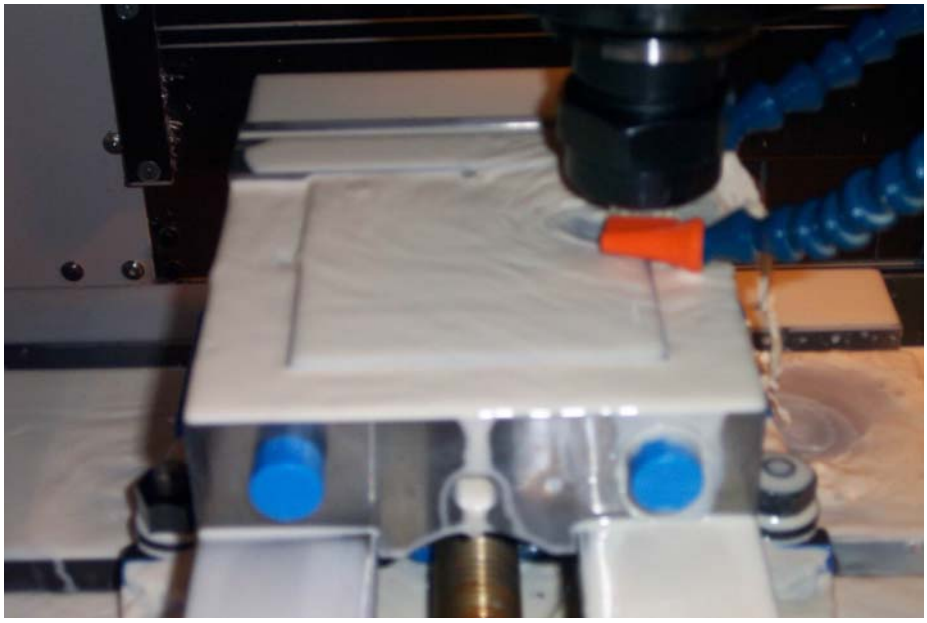

Fig. 7.6. HAAS setup for NiTiNOL composite.

8. RESULTS AND DISCUSSION

Frequency response of NiTiNOL samples and composites that incorporate NiTiNOL was studied. The NiTiNOL samples and the composites were subjected to free undamped vibrations and the resonance modes were obtained using OEH methodology. Based on measured resonance frequencies the modulus of elasticity was determined. The modulus of elasticity was calculated based on the theory presented in Chapter 4 and the results are presented in Section 8.2.

8.1. Chemical analysis of NiTiNOL using the SEM

It is a known fact that material properties are directly related to the stoichiometry of a material. It was, therefore, important to determine the percentage composition by weight for the NiTiNOL sample by utilizing X-ray analysis on the SEM that houses the Kevex system. Quantitative analysis on the NiTi sample provided data pertaining to the amounts of Nickel and Titanium and also traces of other elements. Table 8.1 summarizes composition of the alloy used in this Dissertation, as obtained from the SEM. Details of the information based on which Table 8.1 was generated are included in Appendix D, while Appendix E lists the powder diffraction files used to identify the phases of the NiTiNOL sample using XRD.

From Table 8.1 it is clear that the composition is close to equiatomic. Even very small variations in the stoichiometry are known to affect the material properties. It is also

evident from Table 8.1 that traces of aluminum and silicon were detected in the analysis. The presence of these elements can be attributed to metallographic polishing (Al) and the detector on the SEM (Si).

Table 8.1. Summary of chemical analysis on NiTiNOL.

Element	Line	Weight (%)	K-ratio	Counts/sec	Atomic (%)
Al	Ka	0.13	0.0007	3.97	0.26
Si	Ka	0.32	0.0021	11.82	0.62
Ni	Ka	56.66	0.5537	382.15	47.70
Ti	Ka	42.88	0.4260	934.71	51.42

8.2. Determination of modulus of elasticity from OEH

Using the analytical model presented in Chapter 4, modulus of elasticity of the samples was determined using the resonance frequencies measured by OEH. For a frequency *f* of a cantilever beam undergoing free undamped vibartions, the modulus of elasticity can be calculated as

$$E = \frac{4\pi^2 f^2 L^4 \rho \ A}{\beta_n^4 I} \quad , \tag{8.1}$$

where E is the modulus of elasticity, f is the frequency as measured from OEH, L is the active length of the NiTi sample, ρ is the density of the NiTi sample, A is the cross sectional area of the sample, I is the moment of inertia of the sample, and β_n is the

constant that has specific values for mode shape n. Similarly, the dynamic stiffness of NiTiNOL composites was determined from

$$D_{11} = \frac{E_L}{1 - \mu_{LT}^2 \frac{E_T}{E_L}} \frac{h^3}{12} \quad , \tag{8.2}$$

where subscripts L and T represent the longitudinal and transverse directions, respectively, μ_{LT} represents the Poisson's ratio for the NiTiNOL based composite, E represents the modulus of elasticity, D_{11} represents the dynamic stiffness of the composite, and h is the thickness of the composite.

8.3. Determination of temperature during measurements of the modulus of elasticity

Modulus of elasticity of NiTiNOL and NiTiNOL based structures is a non-linear function of temperature. Therefore, accurate determination of parameters, used in Eqs 8.1 and 8.2, to properly evaluate the equations, depends on accurate knowledge of the temperature of the sample at the instant measurements are made.

In this Dissertation, time constant necessary to assure uniform temperature field throughout the samples was determined experimentally. This determination was based on temperature-time history similar to those shown in Figs 8.1 to 8.4. For example, Fig. 8.1 shows temperature as a function of time measured by a type T thermocouple attached to a control sample during measurements, when the EC was set to change temperature from 79.5ºC to 68.5ºC. Clearly, initial fluctuations stabilize within about 9 min, then

temperature monotonically approaches equilibrium temperature at about 35 min after the instant the change was imposed on the EC.

Similar trend is observed in Fig. 8.2, which shows temperature as a function of time of a control sample exposed to the change in temperature within the EC from 59ºC to 53ºC. This figure indicates that the sample reaches thermal equilibrium at about 30 min after the instant the change in temperature within the EC is imposed.

Figure 8.3 shows temperature as a function of time, measured by a type T thermocouple attached to a control sample during measurements, when the EC was set to change temperature from 40ºC to 50ºC. Initial fluctuations stabilize within about 10 min, then temperature monotonically approaches equilibrium temperature at about 40 min after the instant the change was imposed on the EC. Figure 8.4 also shows a similar trend when the EC was set to a temperature change from 50ºC to 60ºC.

Based on the results shown in Figs 8.1 to 8.4 and similar data for other temperature ranges, the time constant used in this Dissertation was set to 60 min. The time constant was determined by temperature measurements on a 30 mm long, 2.25 mm wide, and 0.5 mm thick NiTiNOL sample. The value of 60 minutes was required to achive thermal equilibrium. Based on this time constant measurements of parameters used in Eq. 8.1 were made 60 min after the temperature change was imposed on the samples within the EC, for all measurements in this Dissertation.

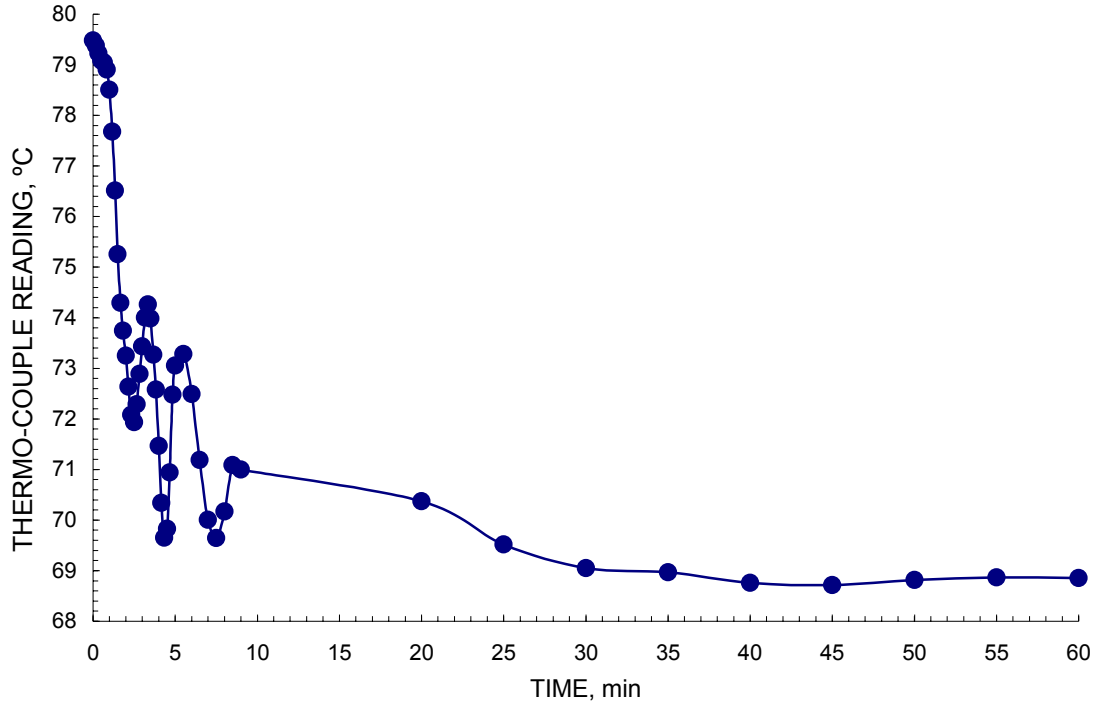

Fig. 8.1. Temperature as a function of time of a control sample exposed to the change in temperature (cooling) from 79.5ºC to 68.5ºC within the EC.

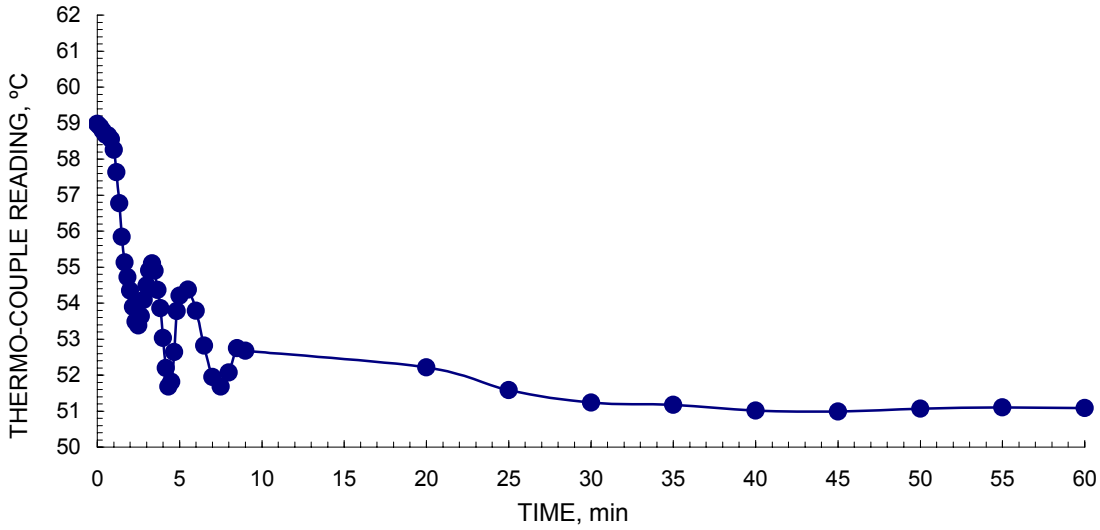

Fig. 8.2. Temperature as a function of time of a control sample exposed to the change in temperature (cooling) from 59ºC to 53ºC within the EC.

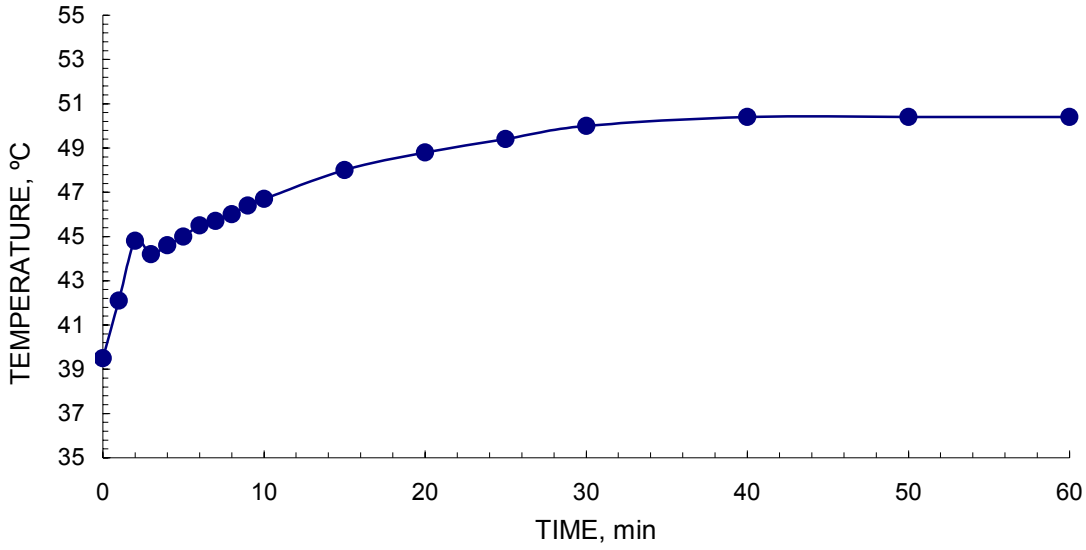

Fig. 8.3. Temperature as a function of time of a control sample exposed to the change in temperature (heating) from 40ºC to 50ºC within the EC.

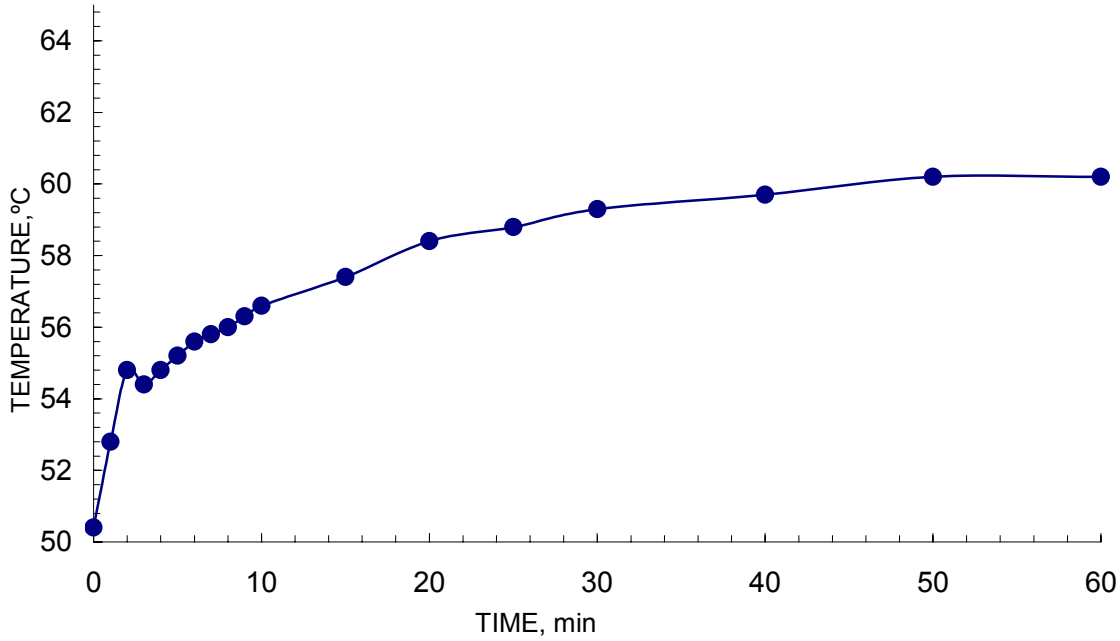

Fig. 8.4. Temperature as a function of time of a control sample exposed to the change in temperature (heating) from 50º to 60ºC within the EC.

8.4. Results from the OEH measurements

In this Section, experimentally determined values of modulus of elasticity are presented as a function of temperature. This determination was made as a function of temperature using the OEH and facilities developed at WPI's CHSLT. The data were obtained for the temperature range from –20ºC to 200ºC. During these experiments all samples were placed in a specially designed EC. Figure 8.5 shows a representative dependence of the modulus of elasticity of NiTiNOL, used in this study, on temperature. Appendix F shows additional results obtained for the temperature dependent modulus of elasticity using OEH.

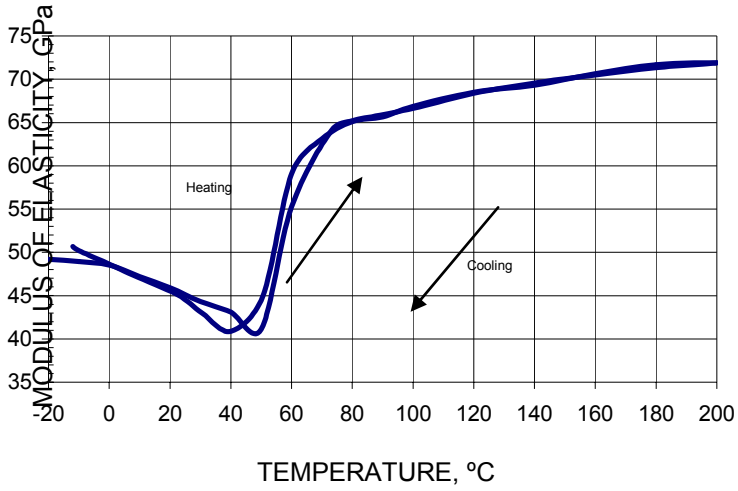

Fig. 8.5. Temperature dependence of modulus of elasticity of NiTiNOL on temperature.

The results shown in Fig. 8.5 clearly indicate a hysteritic behavior due to heating and cooling parts of a cycle, which is typical of SMAs. The slope initially is

found to decrease during the heating part of the NiTi sample. Stated alternately, the modulus of elasticity initially decreases as temperature increases at the beginning of the heating cycle, when temperature increases from -20ºC to 50ºC. According to the results shown in Fig. 8.5 the phase transformation from Martensite to Austenite starts at around 50ºC. Martensitic transformations are never complete in nature and there will always be residual Martensite or Austenite that is retained. The results shown in Fig. 8.5 were obtained for the NiTiNOL sample of effective length of L = 39.85 mm, and the modulus of elasticity was calculated from the first bending mode. Similar dependence of modulus of elasticity on temperature was observed for the second, third, and the fourth bending modes.

Figure 8.6 shows the combined results from the first four bending modes for the NiTi sample with L = 39.85 mm. There is good agreement between the moduli of elasticity shown.

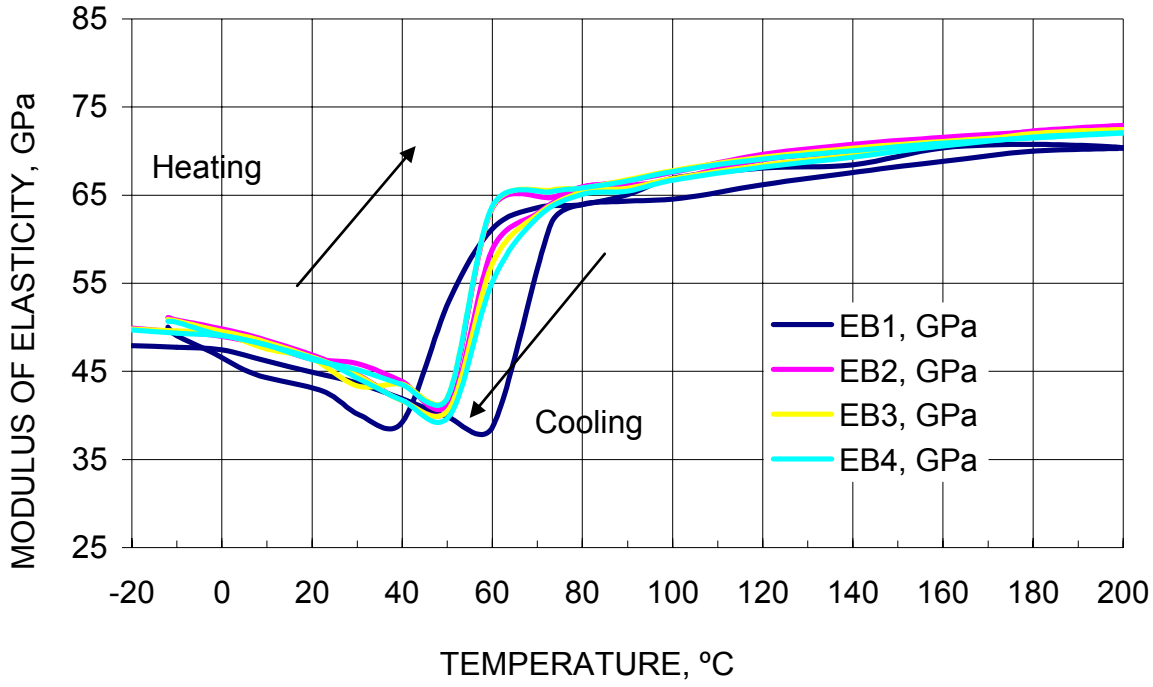

Fig. 8.6. Modulus of elasticity of NiTiNOL as a function of temperature, based on the first four bending modes of a 39.85 mm long sample.

OEH was also used to determine the modulus of elasticity of the matrix material. Based on the OEH measurements, the modulus of elasticity was determined to be 14 GPa. The composite was mounted as a cantilever plate and the effective length and width were 4 inches and 2.5 inches, respectively; the thickness was 0.25 inches. Dimensions of the NiTiNOL ribbon were 0.84 mm by 0.17 mm. At the TT of 60ºC there is a change in the resonant frequency of the composite due to activation of the NiTiNOL fibers. The introduction of NiTiNOL fibers in the matrix material can, therefore, be used to shift the resonant frequency of the composite as a whole. The composite was subjected to

vibrations using a PZT shaker. Change in the TT between the heating and cooling cycles is normally attributed to hysteresis or absorption of energy. Figures 8.7 and 8.8 represent the first two mode shapes for the NiTiNOL composite with cantilever boundary conditions.

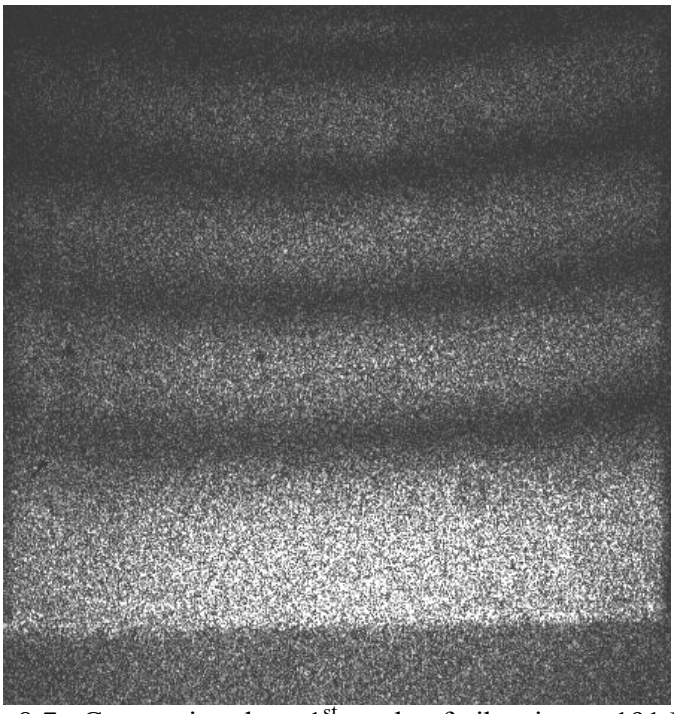

Fig. 8.7. Composite plate: 1st mode of vibration at 191 Hz.

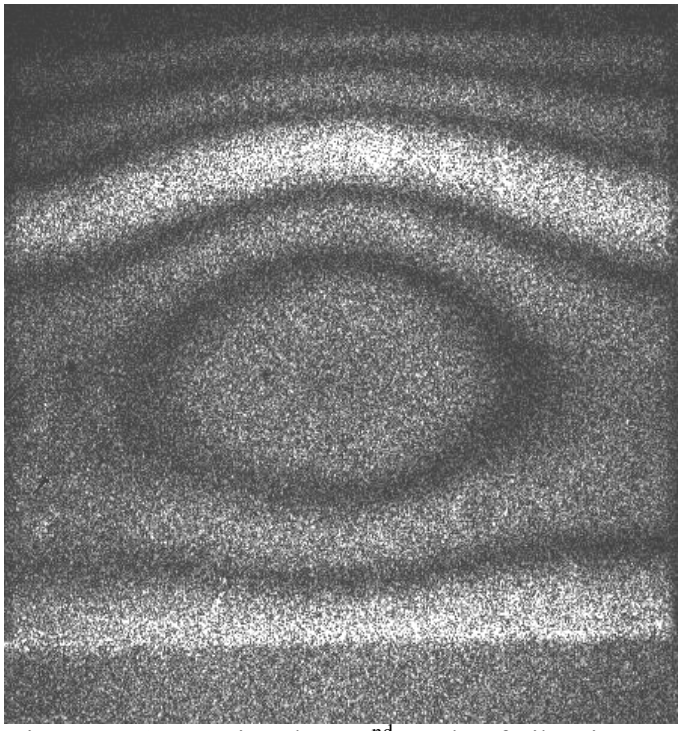

Fig. 8.8. Composite plate: 2nd mode of vibration at 993 Hz.

Figure 8.9 represents dependence of resonant frequency of the NiTiNOL composite on temperature. As seen from Fig. 8.10 it is evident that repeated activation of the NiTiNOL fibers results in an upward shift (i.e., an increase) in the frequency response. In the absence of the NiTiNOL fibers the frequency response would have had a decreasing slope. This would mean that the modulus of elasticity would decrease as temperature is increased. Appendix G presents additional results for the thermomechanical response of NiTiNOL based composites that were investigated in this Dissertation. Appendix H presents the temperature dependence of the NiTiNOL based composites as determined from Eq. 8.2.

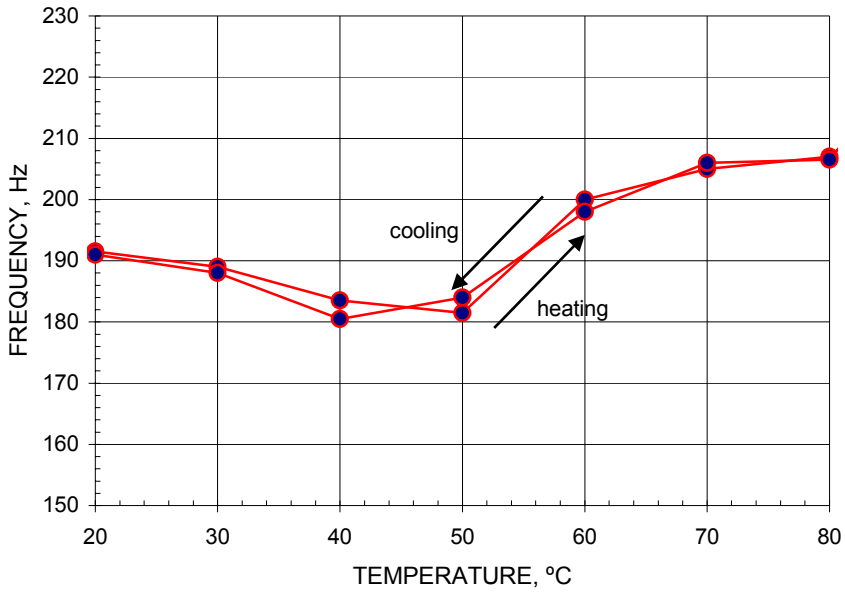

Fig. 8.9. Thermomechanical response of the 30 mm by 30 mm NiTiNOL-polymide composite as measured by OEH: Run 01 (additional results are included in Appendix F).

Results presented in this Dissertation show that the thermomechanical response of NiTiNOL and NiTiNOL based structures can be determined using OEH methodology. This Dissertation used ACES methodology to determine dependence of the modulus of elasticity of NiTiNOL and NiTiNOL based structures on temperature. It also addressed issues relating to hysteresis from thermomechanical cycling. Hysteresis involves a change (usually an increase) in the TT resulting in thermomechanical cycling. Figure 8.10 shows hysteresis observed in NiTiNOL while it is undergoing an activation during the first 40 cycles. A cycle represents one heat-cool loop that results in a phase transformation from Martensite to Austenite and back to Martensite. The Dissertation

also includes uncertainty analysis of metal matrix (e.g., aluminum) based NiTiNOL composites.

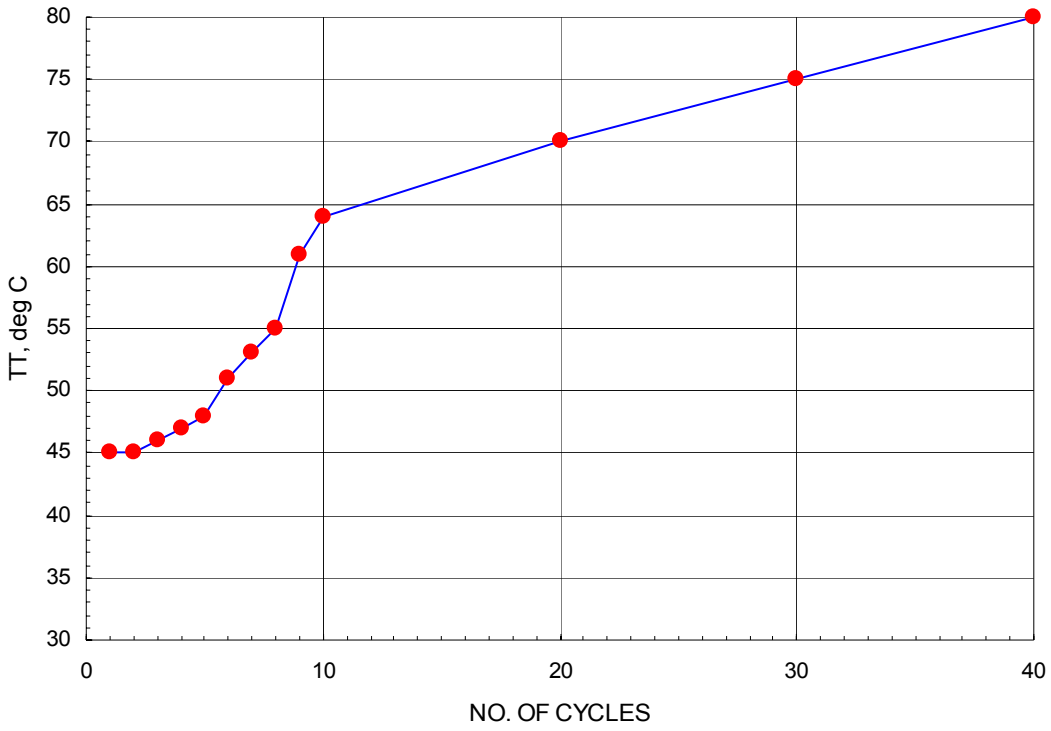

Fig. 8.10. Hysteresis as indicated by change in TT for NiTiNOL during the first 40 cycles.

8.5. Uncertainty analysis on the modulus of elasticity for NiTiNOL and NiTiNOL based composites

As discussed in Chapter 4, uncertainty analyses were conducted for obtaining tolerances on design parameters that best facilitate improved design. In this Dissertation uncertainty analysis was performed based on the RSS method to determine tolerances for the modulus of elasticity (Mizar, 1999). Figure 8.11 shows uncertainty in the average

modulus of elasticity (in the units of MPa) as a function of temperature of a NiTiNOL sample of length 39.95 mm. Appendix I presents additional results from uncertainty analysis for NiTiNOL and NiTiNOL based composites.

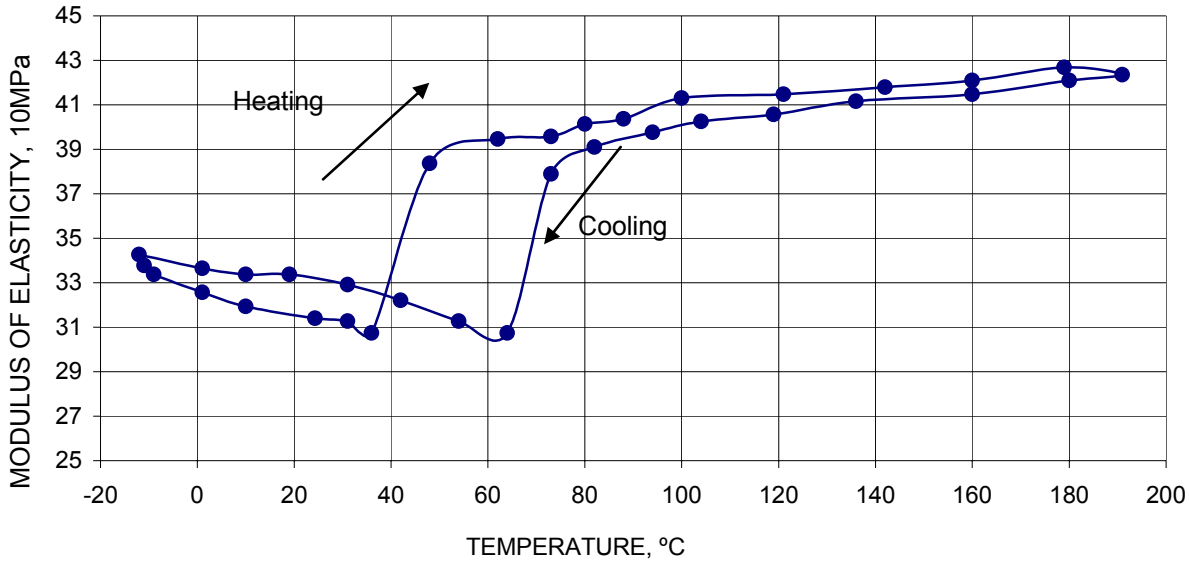

Fig. 8.11. Uncertainty of the average modulus of elasticity as a function of temperature for NiTiNOL of length 39.85mm.

8.6. Development of material model for NiTiNOL

As discussed in this Dissertation, NiTiNOL exhibits complex thermomechanical behavior. Based on the properties of MT, that NiTiNOL undergoes, it is evident that the phase transformation depends on stress, strain, and temperature. Also, from different types of shape memory phenomena exhibited by NiTiNOL such as OWE, TWE, and pseudoelasticity (Chapter 3), it is possible to execute successful designs incorporating NiTiNOL in which only one of the three states (i.e., stress, strain, or temperature) can be

the controlling parameter. This simplifies calculations involved during development of NiTiNOL related designs.

The objective of this Dissertation was to develop a method that could characterize NiTiNOL and to obtain material properties as a result of this characterization. NiTiNOL was successfully characterized using the OEH technique that aided in obtaining temperature dependence of the modulus of elasticity. In literature that normally deals with material property values for NiTiNOL or any other SMA, only values at the martensitic plateau, or the parent phase are listed. This means that the actual temperature dependence of the modulus of elasticity is ignored in the design process because of unavailability of these characteristics (Duerig, 1990).

Using temperature dependent nature of the modulus of elasticity as obtained from OEH, an interpolation function has been developed that facilitates simulation of the thermomechanical behavior of NiTiNOL using computational techniques such as FEM. Equation 8.3 represents a preliminary interpolation function that has been developed in this Dissertation. As more advancement is done in the characterization process, the interpolation function will also be improved accordingly. Table 8.2 represents a summary of coefficients for the interpolation function given by Eq. 8.3.

$$\ln\left(E\right) = \frac{\left(a + c \cdot T + e \cdot T^2\right)}{\left(1 + b \cdot T + d \cdot T^2\right)} \quad , \tag{8.3}$$

where a, b, c, d, and e represent interpolation coefficients, E is the modulus of elasticity, and T is the temperature.

Table 8.2. A summary of the interpolation function.

Parameters	Values	Std Error	T Value	95% Conf Limit	95% Conf Limit
A	24.5803	0.03211	765.588	24.51089396	24.64978827
B	-0.0244	0.00431	-5.6723	-0.033759477	-0.015120117
C	-0.6054	0.10785	-5.6129	-0.838658079	-0.372076903
D	0.00029	0.00012	2.46499	3.55575E-05	0.000544968
E	0.00724	0.00295	2.45655	0.000864565	0.013606736

Figure 8.12 represents a plot of the interpolation function as given by Eq. 8.3 This interpolation function was used as input for FEM computations using FEMLAB® version 3.2 (Appendix A). It is also to utilize the interpolation function in designs where modulus of elasticity is a parameter. This type of approach for developing an interpolation function for the temperature dependence of the modulus of elasticity can facilitate complete considerations of the dependency of material properties on temperature.

Figure 8.13 shows the difference between the OEH measured values and the interpolated values that were obtained using Eq. 8.3. It is evident from Fig. 8.13 that the maximum difference between the measured and the interpolated values occurs around the phase transition temperature. This is expected as lot of activity takes place as the martensitic phase gets transformed into the austenitic phase. As better versions of the interpolation function are developed and/or additional experimental data are obtained, in the future, it may be possible to have smaller differences between measured and interpolated values.

8.7. Shape memory alloy based composites (SMABC)

8.7.1. Introduction

The SMABC constitute materials that are reinforced with shape memory alloy (SMA) fibers. Sometimes the SMA fibers can be replaced with thin-film SMA. A thin-film is a sheet of the SMA usually about 50 microns in thickness. One of many configurations of SMABC is when SMA fibers (e.g., ribbons, wires) are embedded on either side of the neutral axis of the matrix material. When the SMA fibers, or a composite, are heated, there will be a change in the resultant stiffness of the structure. This is because the SMA fibers will undergo a phase transformation from the low temperature phase (Martensite) to the high temperature phase (Austenite). This phase transformation is complete at the Transformation Temperature (TT). In this Dissertation, annealed NiTiNOL SMA (the most commonly used SMA) was used in SMABC considered herein. The composites were subjected to free undamped vibrations, in which resonant frequencies were monitored as functions of temperature. From the experimentally determined resonant frequencies, dynamic stiffness of the composites was determined as a function of temperature.

8.7.2. Determination of effective modulus of elasticity (EMOE)

A unidirectional composite consists of parallel fibers arranged in a matrix. This type of an arrangement forms a basic configuration of composite materials. An elementary cell of such a composite can be considered to be made of a fiber embedded in

a matrix with either a circular or a rectangular base. Figure IB1.1 shows such a unit cell of a composite material. The direction parallel to the fibers in the composite is referred to as the longitudinal direction. Any direction that is perpendicular to this direction is referred to as the transverse direction. Simplified and practical expressions for material properties (e.g., modulus of elasticity) can be determined by considering mechanical behavior of a unit cell of a composite material. Derivations of modulus of elasticity for the longitudinal and transverse directions are discussed in Sections IB1.3, and IB1.4, respectively.

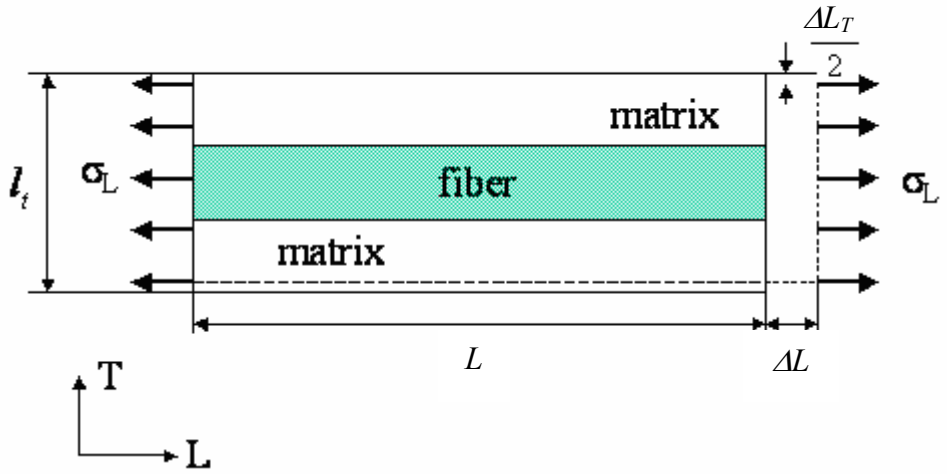

Fig. 8.12. Simplified representation of a composite cell under uniform state of tension.

8.7.3. Derivation of modulus of elasticity in the longitudinal direction

The longitudinal modulus of elasticity (LMOE) is determined normally from a longitudinal tensile tests. It is assumed that the fiber and the matrix undergo uniform and

identical elongation under the applied longitudinal stress. A schematic diagram used in the analysis is shown in Fig. 8.12.

If ΔL represents the elongation experienced by both the fiber and the matrix, the longitudinal strain ε_L can be written in as

$$\varepsilon_L = \frac{\Delta L}{L} \quad , \tag{8.4}$$

where L is the length of the cell under consideration. Strain in the fiber as well as in the matrix, in relation to the longitudinal strain as defined by Eq. 8.4, can be written as

$$\varepsilon_f = \varepsilon_m = \varepsilon_L \quad , \tag{8.5}$$

where ε_f and ε_m represent the strains in the fiber and the matrix respectively.

The fiber and the matrix are supposed to behave elastically (within allowable elastic limits), the stresses in the fiber and the matrix can be written as

$$\sigma_f = E_f \varepsilon_f = E_f \varepsilon_L \quad , \tag{8.6}$$

and

$$\sigma_m = E_m \varepsilon_m = E_m \varepsilon_L \quad . \tag{8.7}$$

Resultant load (force) carried by the composite material is the sum of all loads carried individually by the fibers and the matrix and can be written as

$$F_R = \sigma_f A_S + \sigma_m A_m \quad , \tag{8.8}$$

where F_R is the resultant force, σ_f is the stress induced in the fiber, σ_m is the stress induced in the matrix of the composite, while A_f, A_m are the cross-sectional areas of the

fibers and matrix, respectively. If A is the cross-sectional area of a unit cell of a composite material, then we can write the average stress as follows:

$$\sigma_{Avg} = \frac{F_R}{A} \quad . \tag{8.9}$$

Equation 8.9 can be rewritten as

$$\sigma_{Avg} = \sigma_f V_f + \sigma_m V_m \quad , \tag{8.10}$$

where V_f and V_m are the volume fractions for the fibers and the matrix, respectively.

The average stress for the cell of the composite material can be written in terms of the longitudinal modulus of elasticity E_L as

$$\sigma_{Avg} = E_L \varepsilon_L \quad . \tag{8.11}$$

Combining Eqs 8.5 and 8.6 we have from Eq. 8.11

$$E_L = E_f V_f + E_m \left(1 - V_f\right) \quad . \tag{8.12}$$

Equation 8.12 can be referred to as the law of mixtures (LOM) for the modulus of elasticity in the longitudinal direction. Variations of the moduli E_f and E_m are linear, and the volume fractions V_f and V_m take values that vary from 0 to 1.

8.7.4. Determination of the longitudinal Poisson's ratio (LPR)

In order to determine the LPR, the unidirectional composite is considered to be described by successive layers. A schematic representing a unidirectional composite is shown in Fig. 8.13. The LPR represented by (LPR means Poisson's ratio for the longitudinal direction of the composite) μ_{LT} can be determined based on a longitudinal

tensile test. As a result of this tensile test, the fibers and the matrix of the composite material will be subjected to uniform amounts of strains (i.e., identical strains).

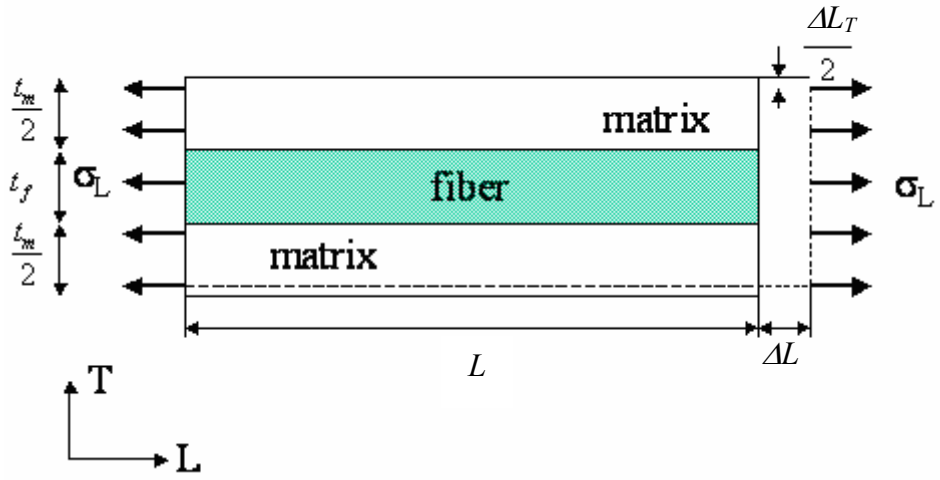

Fig. 8.13. Layer description of longitudinal tension in a composite cell.

Therefore the transverse strains induced in the matrix as well as the fibers can be written as follows:

$$\varepsilon_{\tau m} = -\mu_m \varepsilon_L \quad , \tag{8.13}$$

and

$$\varepsilon_{\tau f} = -\mu_f \varepsilon_L \quad . \tag{8.14}$$

Under the applied stress, the corresponding elongation of the elemental cell of the composite can be written as

$$\Delta L_T = -\mu_m \varepsilon_L t_m - \mu_f \varepsilon_L t_f \quad . \tag{8.15}$$

where t_m is the thickness of the matrix and t_f is the thickness of the fibers, respectively.

The corresponding transverse strain can be written in the form

$$\varepsilon_T = \frac{\Delta L_T}{t_f + t_m} = -\left[\mu_m\left(1 - V_f\right) + \mu_f V_f\right]\varepsilon_L \quad . \tag{8.16}$$

The equation for the LPR can, therefore, be written as

$$\mu_{LT} = -\mu_f V_f - \mu_m\left(1 - V_f\right) \quad . \tag{8.17}$$

Equation 8.17 represents the law of mixtures for the LPR.

8.7.5. Determination of the longitudinal shear modulus (LSM)

Figure 8.14 displays a schematic representation of the cross-section of a composite that is subjected to a shear stress τ. Figure 8.14 is used in the derivation of the LSM of the composite material.

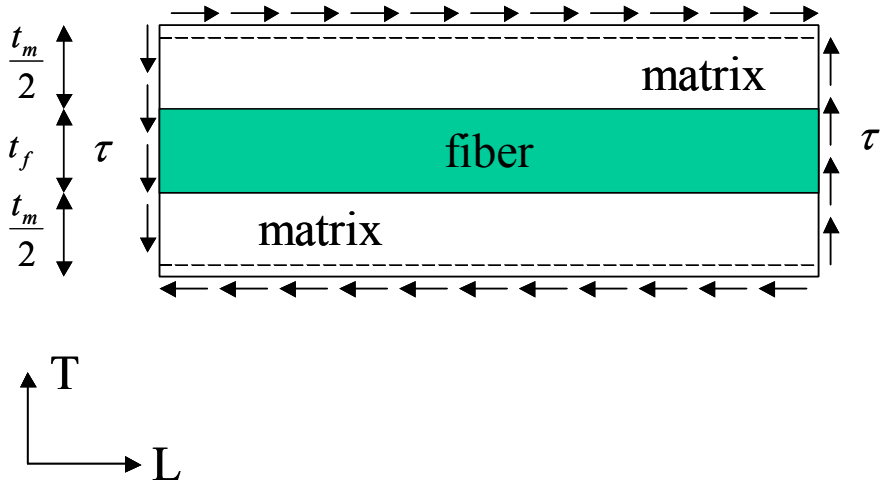

Fig. 8.14. Longitudinal shear modulus for a composite cell.

The LSM denoted by G_{LT} is determined using a longitudinal shear test. Determination of the LSM is done using a unidirectional composite comprised of layers. As a result of the shear stress, the corresponding shear strains induced in the unit cell of the composite can be written as follows:

$$\gamma_f = \frac{\tau}{G_f}, \quad \gamma_m = \frac{\tau}{G_m} \quad . \tag{8.18}$$

The shear deformations induced in the fibers and matrix can be written as

$$\delta_f = t_f \gamma_f \text{ and } \delta_m = t_m \gamma_m \quad . \tag{8.19}$$

Total shear deformation of a unit cell of the composite material can be written as

$$\delta = \delta_f + \delta_m = t_f \gamma_f + t_m \gamma_m \quad . \tag{8.20}$$

The corresponding shear strain for the unit cell of the composite material can be shown to be

$$\gamma = \frac{\delta}{t_m + t_f} \quad . \tag{8.21}$$

Equation IB1.18 can be rewritten as

$$\gamma = \gamma_f V_f + \gamma_m \left(1 - V_f\right) \quad . \tag{8.22}$$

The shear strain is related to the shear stress by means of the shear modulus, given by G_{LT}, i.e.,

$$\gamma = \frac{\tau}{G_{LT}} \quad . \tag{8.23}$$

Combining Eqs 8.19 to 8.23 we obtain

$$\frac{1}{G_{LT}} = \frac{V_f}{G_f} + \frac{1 - V_f}{G_m} \quad . \tag{8.24}$$

Using Eq. 8.24 the LSM can be determined. Equations 8.4 through 8.24 provide the mathematical background that will be used in Section 8.7.6 to determine the behavior of a NiTiNOL composite based on measured material properties.

8.7.6. Determination of thermomechanical response of a NiTiNOL composite based on measured material properties

In this Dissertation, from analytical considerations, the frequency of resonance for NiTiNOL based composites was obtained using the Ritz's method and is given by

$$f_i = \frac{1}{2\pi} K_i \frac{1}{ab} \sqrt{\frac{D_{11}}{0.70\rho}} \quad , \tag{8.25}$$

where D_{11} can be obtained to be

$$D_{11} = \frac{E_L}{1 - \mu_{LT}^2 \frac{E_T}{E_L}} \frac{t^3}{12} \quad . \tag{8.26}$$

In Eq. 8.26, t is the thickness of the composite, the subscripts L and T represent the longitudinal and transverse directions, respectively, while

$$\mu_{LT} = -\mu_f V_f - \mu_m (1 - V_f) \quad , \tag{8.27}$$

where V represents the volume, and the subscripts f and m represent the fiber and matrix, respectively, μ_{LT} represents the Poisson's ratio for the NiTiNOL based composite as defined by Eq. 8.17.

The values of K_i (appearing in Eq. 8.25) equal 5.429 for the first mode and 15.108 for the second mode (Mizar and Pryputniewicz, 2004). The modulus of elasticity for the polycarbonate matrix material was determined (in this Dissertation) based on the resonant frequencies of a cantilever configuration of the material of the matrix.

In this Dissertation, modulus of elasticity for the matrix materials (polymide) as well as the modulus of elasticity for NiTiNOL were determined experimentally using the OEH technique. It is therefore possible to use the experimentally determined material property values along with the model developed as given by Eq. 8.26, to estimate the thermomechanical response of the NiTiNOL composite. Sample calculations indicating the procedure for obtaining the response for the NiTiNOL-polymide composite based on experimentally measured material properties are presented in this section. The volume fraction for the matrix was 0.88 (i.e., polymide) and for the NiTiNOL fibers was 0.12, respectively. Based on the volume fractions, the longitudinal modulus of elasticity can be determined by Eq. 8.27 to be

$$E_L = E_f V_f + E_m \left(1 - V_f\right) \quad . \tag{8.28}$$

Similarly, Eq. 8.29 is used to determine the modulus of elasticity in the transverse direction

$$\frac{1}{E_T} = \frac{V_f}{E_f} + \frac{\left(1 - V_f\right)}{E_m} \quad . \tag{8.29}$$

where E_L represents the modulus of elasticity in the longitudinal direction, E_T represents the modulus of elasticity in the transverse direction, E_f represents the modulus of

elasticity for the NiTiNOL fibers, E_m represents the modulus of elasticity for the polymide matrix, and V_f represents the volume fraction for the NiTiNOL fibers. Based on the OEH measurements, the modulus of elasticity for the polymide matrix was determined as 10 GPa, and was determined to be 37 GPa for the NiTiNOL fibers for the composite at 20ºC. Equation 8.27 represents the Poisson's ratio for the NiTiNOL-polymide composite. The Poisson's ratio for the polymide matrix material was taken as 0.33 and for the NiTiNOL fibers to be 0.32 based on "book values" (Whitney and Ashton, 1987). Based on these values for Poisson's ratio and volume fractions, using Eq. 8.27, the overall Poisson's ratio, μ_{LT} was determined to be -0.33. Similarly, based on Eq. 8.28, E_L was calculated to be equal to 33.7 GPa, and E_T (based on Eq. 8.29) was calculated to be equal to 10.9 GPa. Using Eq. 8.26 we have an estimated value of D_{11} equal to 14 *N/m*. Similar calculations were performed for temperatures ranging from 20ºC to 100ºC, for both the heating and cooling cycles. The estimated response is shown in Fig. 8.16. It is important to note that the prediction using analytical models, takes into account the boundary conditions set forth during the development of the analytical model. It is therefore for the sake of completeness to compare the response obtained from experimentation (i.e., OEH measurements) to the estimated response. Figure 8.16 shows the thermomechanical response in terms of dynamic stiffness change as a function of temperature based on experimental considerations.

The next step is to obtain a difference between experimentally determined response and the estimated (i.e., analytical) response. Such a comparison is shown in

Fig. 8.29. Based on calculations for a temperature of 20ºC, the difference between the measured and the analytically estimated value of the dynamic stiffness was found to be equal to 1.2 *N/m*. As seen from Fig. 8.29, the maximum difference between experimental and estimated values of the dynamic stiffness occurs in the vicinity of the TT, for both heat and cool parts of the loading cycle. This is expected, as most of the forward and reverse phase transformation is prominent at the TT. Also, the difference between experimental and predicted values of the dynamic stiffness is a result of the difference in boundary conditions between the actual composite, and the assumptions in the boundary conditions made during the analytical modeling. Analytical models consider perfect boundary conditions, and also complete contact between the matrix and the fibers. However, experimentally the contact condition between the matrix and the fibers is such that there is no stress in the NiTiNOL fibers; which is a condition that does not properly represent the "actual loading". This is to ensure that during testing, any stress in the NiTiNOL fibers could result in strain energy, and therefore change in the type of modal modification technique (i.e., active modal modification) that was proposed in the Dissertation. It is therefore possible to estimate response of NiTiNOL based composites using proper analytical models, and boundary conditions when experimentally determined material properties for the matrix and NiTiNOL fibers are known. The important and the most critical thing, however, are the proper application and interpretation of boundary conditions. The analytical model used in the estimation of the NiTiNOL-polymide composite also ignores the strain energy in the fibers, and therefore will not contribute additional errors.

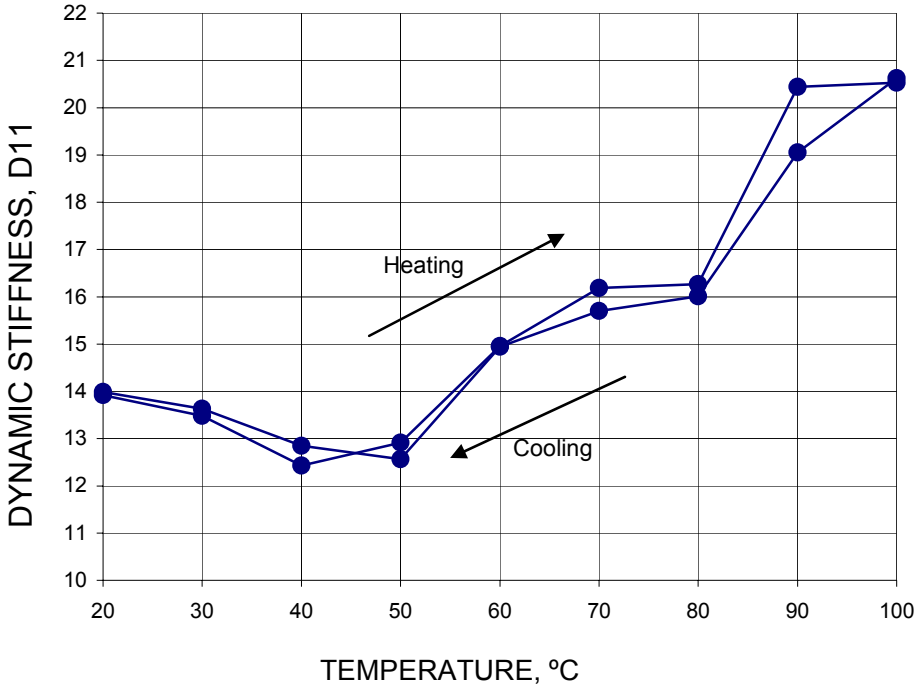

Fig. 8.15. Temperature dependence of the dynamic stiffness for a NiTiNOL-polymide composite as estimated by the analytical model.

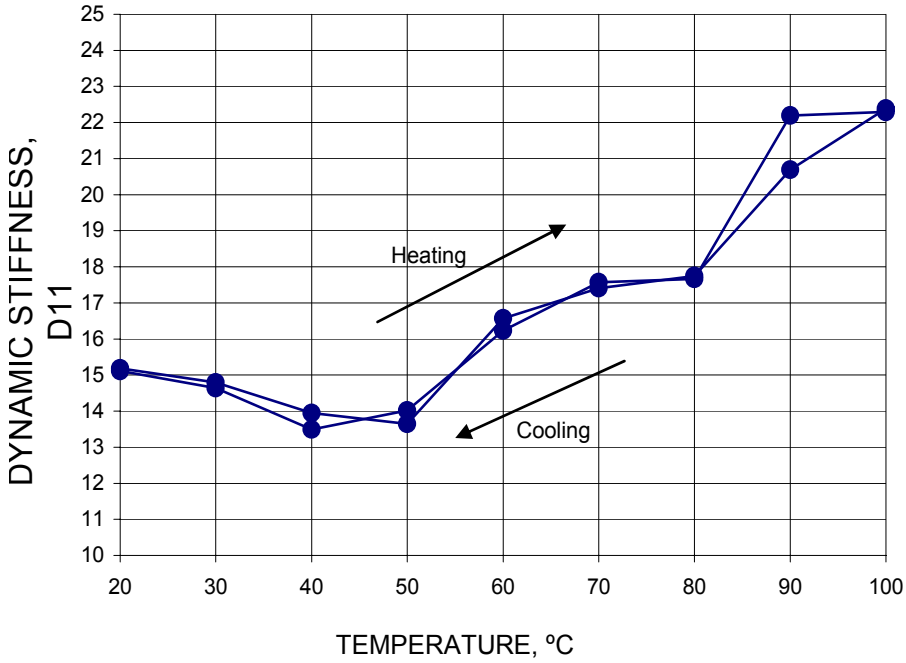

Fig. 8.16. Temperature dependence of the dynamic stiffness for a NiTiNOL-polymide composite as measured by OEH.

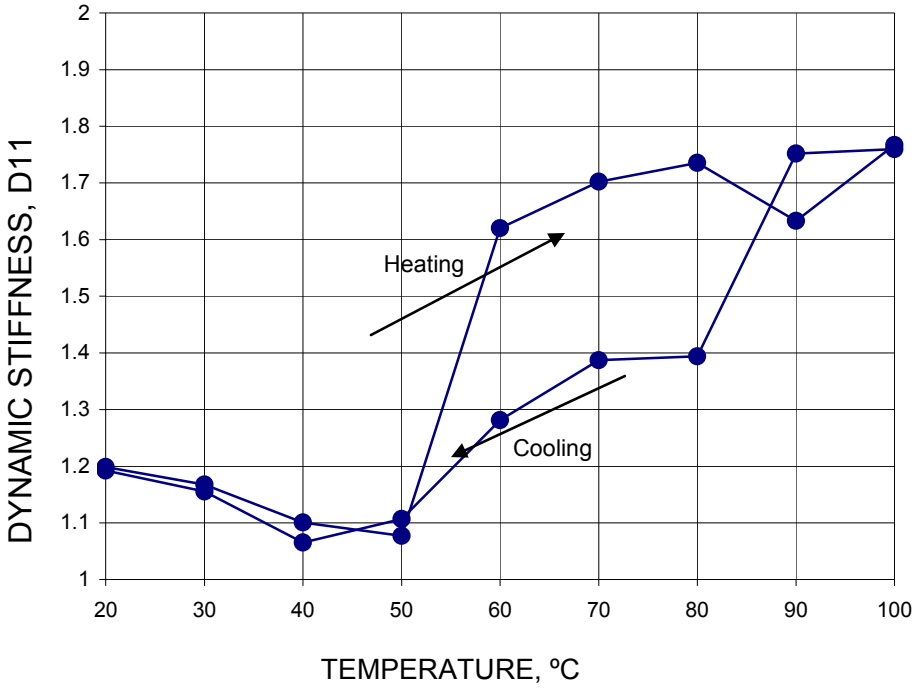

Fig. 8.17. Difference between experimental and analytical values for dynamic stiffness for a NiTiNOL-polymide.

In the Dissertation, the uncertainty in the experimentally determined dynamic stiffness for a NiTiNOL-polymide composite was 1.21 *N/m* at 20ºC. The difference plot (between experimental and analytical values of the dynamic stiffness D_{11}) indicated by Fig. 8.17 shows a value of 1.2 *N/m*. Therefore, the estimated response of the NiTiNOL-polymide composite can be considered to be within the uncertainty bounds based on the RSS technique (Pryputniewicz, 1993; Mizar, 1999).

8.8. Comparison of results from OEH and FEM for NiTiNOL

Results obtained from OEH and FEM are compared and discussed in this Section. Holograms were measured based on the theory presented in Chapter 7. Representative mode shapes predicted by FEM analysis (for the samples used in this Dissertation) are presented in Figs 8.14 and 8.15. The results of Figs 8.14 and 8.15 were obtained at temperatures of 25ºC and 20ºC, respectively. Additional results showing comparison of FEM and OEH data, for the temperature range from 20ºC to 200ºC, are included in Appendix J. The resonance frequencies as obtained from FEM are compared with frequencies from OEH, Figs 8.18 to 8.19.

From Figs 8.18 and 8.19 the resonance frequencies based on FEM and OEH correlate well. In this Dissertation the ACES approach has been implemented and all of the three methodologies agree within the limits based on the uncertainty analysis. The uncertainty analysis indicated a variation of 10% - 12% respectively. Appendix J presents additional results for comparison between OEH and FEM. Recommendations and conclusions are discussed in Chapter 9.

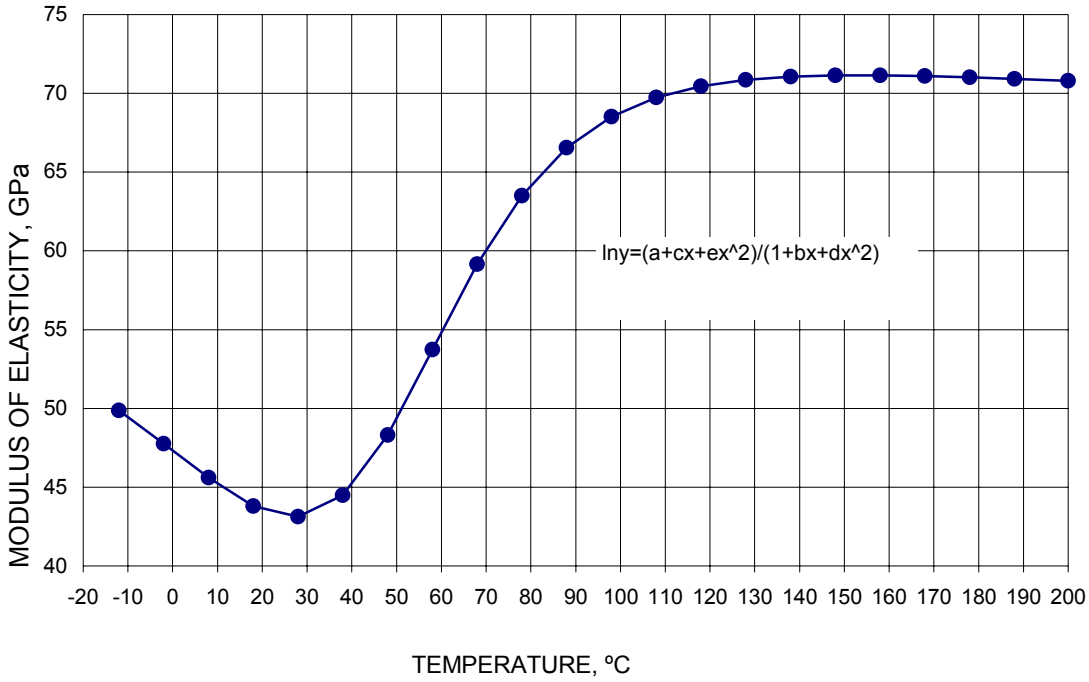

Fig. 8.12. Interpolation function for the temperature dependence of modulus of elasticity for NiTiNOL.

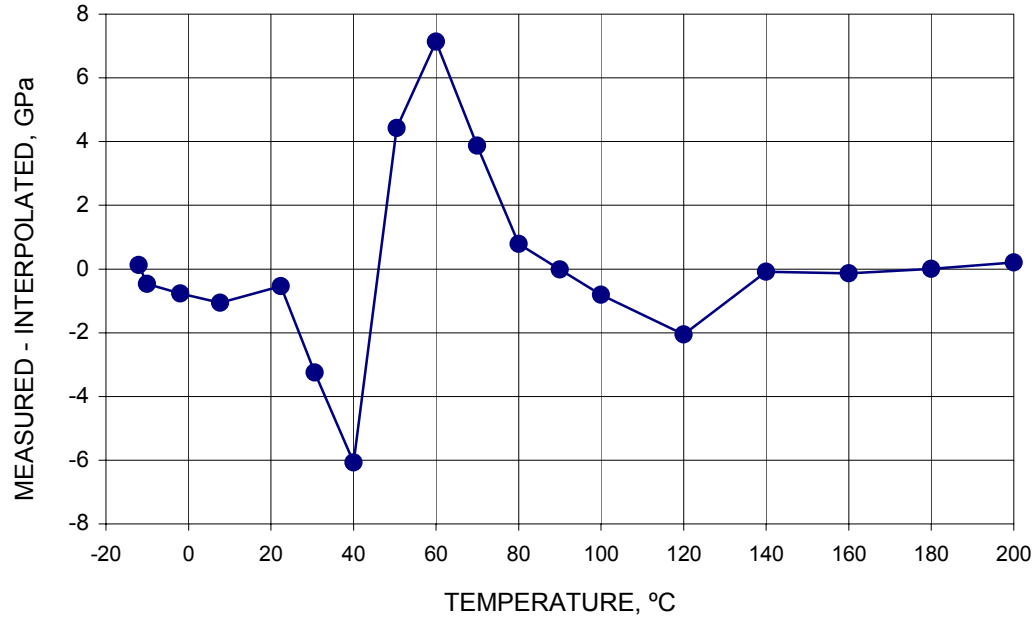

Fig. 8.13. Difference between measured and interpolated values of the modulus of elasticity for NiTiNOL.

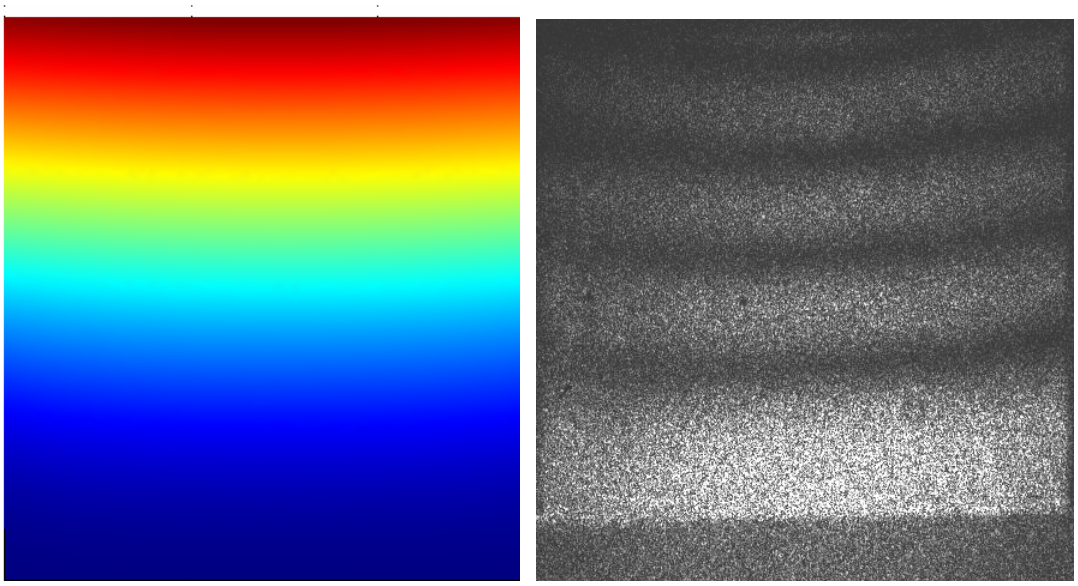

B1 = 1610 Hz B1 = 1623 Hz

Fig. 8.14. Comparison of results from FEM
and OEH for NiTiNOL – Al composite (30 mm by 30mm), measured at T = 25ºC.

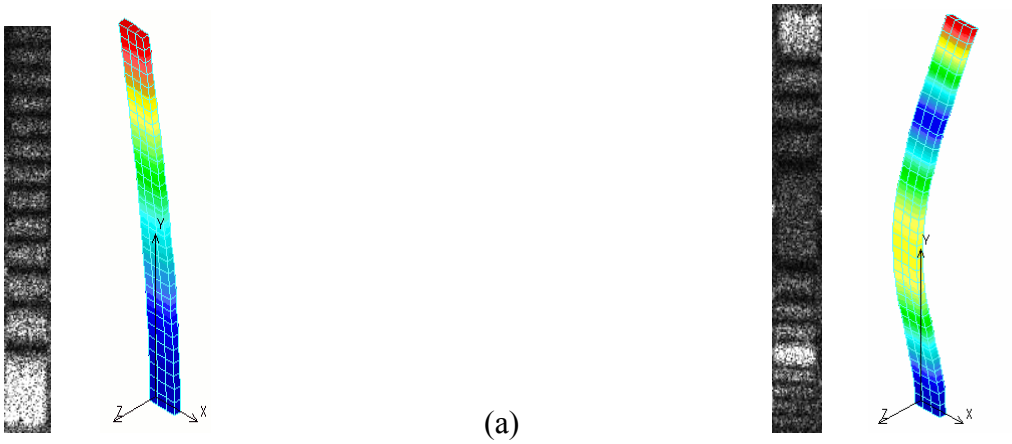

(a)

First bending mode
FEM = 291.3 Hz
OEH = 288.0 Hz

Second bending mode
FEM = 1819.0 Hz
OEH = 1790.0 Hz

Fig. 8.15a. Comparison of results from FEM (shell)
and OEH for NiTiNOL of length 28.82 mm; the first and the
second bending modes, measured at T= 20ºC.

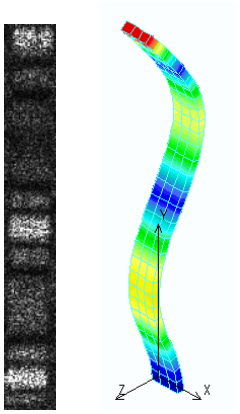

Third bending mode
FEM = 5127.2 Hz
OEH = 5080.0 Hz

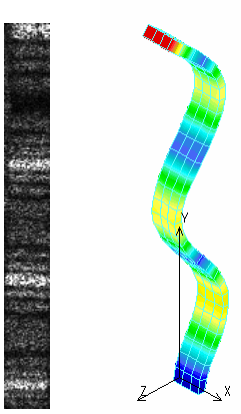

Fourth bending mode
FEM = 9985 Hz
OEH = 9950 Hz

Fig. 8.15b. Comparison of results from FEM (solid) and OEH for NiTiNOL of length 28.82 mm; the third and the fourth bending modes, measured at T = 20ºC.

9. CONCLUSIONS AND RECOMMENDATIONS

Results presented in this Dissertation show validity of using a hybrid approach in characterizing NiTiNOL, a SMA. The Dissertation presents, discusses, and shows validity of a hybrid approach, based on the ACES methodology, which provides the user with results and insight. By doing so, the user can be certain and comfortable with modeling and with results obtained. This Dissertation applied analytical and experimental methodologies to determine dependence of the modulus of elasticity on temperature, and computational techniques (FEM) were used to simulate/model experimental results. A fundamental background on SME, ACES methodology, analytical, computational, and experimental methodologies have been provided to familiarize the reader with these topics.

In this Dissertation a variety of methods have been used. OEH was used to characterize the modulus of elasticity, XRD was used for identification of phases present after heat treatment, SEM was used to conduct chemical analyses that provided information on elements present by %weight. Computational techniques, in particular the FEM, were used to computationally simulate behavior of samples used.

Material property value determination was achieved by OEH, a noninvasive holographic methodology.

Many times analyses are performed based on “book”, or published, values of material properties. This usually results in inaccuracy in evaluation/analysis of the design. The errors resulting from poorly defined material property values are even more

critical for SMAs, which exhibit a strong dependence of these material property values on stress, strain, and temperature. The material dependence (e.g., modulus of elasticity) on temperature was measured by OEH and the values obtained reflect reality and actual behavior of the material used rather than the approximate (sometimes, very approximate) "book" values (or ranges) provided by the manufacturer.

Linear computational methods used in this study correlate to within 0.3% with the analytical and experimental results. In spite of the close correlation of 0.3% (Chapter 8 and Appendix J), it is not sufficient to account for phenomena taking place during phase transformations. Therefore, a non-linear FEM approach based on a thermomechanical foundation (taking into account the phase transformations) would possibly provide results that have a closer agreement with experimental results and should be used in subsequent research. The same holds for comparisons between analytical and experimental results. The "book" values provide ranges for the moduli of elasticity for Martensite and Austenite. Correlation between analytical and computational results would agree better if non-linear approaches were used. In this Dissertation, a comparison between analytical and experimental methods yielded differences ranging from –0.8% to –18%, and comparisons between experimental and computational results have provided differences in the order of –0.8%.

Overall, this Dissertation shows that there exists good correlation between the analytical, computational, and experimental methodologies in terms of material property determination and prediction of resonance frequencies based on experimental values for NiTiNOL. Furthermore, following convergence analysis, the FEM can be used as a

primary source of analysis in place of expensive and often time consuming experimental work. Finally, a hybrid approach, such as ACES methodology, proves to be an important step in the characterization of material behavior.

Development of cost effective and durable high performance engineering structural materials and systems is important for the economic well being of a country. This is because the cost of civil infrastructure constitutes a major portion of the national wealth. To address issues relating to deteriorating civil infrastructure, research is essential on smart and/or adaptive materials. This discussion relates to use of smart materials for optimal performance and design of buildings and other civil infrastructures particularly those under the threat of earthquakes and other natural hazards. The unique properties of the SMAs for smart structures render a promising area of research.

The term shape memory refers to the ability of certain alloys (e.g., Ni-Ti, Cu-Zn-Al) to recover large strains, while remembering their initial configurations at the end of the phase transformation process. The deformation recovery is triggered by a change in temperature, with the recovery being complete at a critical transformation temperature known as TT. The particular properties of SMAs are strictly associated with solid to solid phase transformations, which can be either thermal or stress induced. Currently, SMAs are mainly applied in biomedical engineering applications, electronics and communications engineering, aerospace applications, and structural applications. However, a potential for use of these alloys can be extended to new applications in civil

engineering specifically in seismic protection of buildings. Properties of SMAs that render them to be ideal candidates for use in seismic applications are:

1) repeated absorption of large amounts of strain energy under loading without permanent deformation,
2) recoverable strain from 8% to 11%,
3) fatigue resistance even under large strain cycles,
4) possibility to obtain a wide range of cyclic behavior - from supplemental and fully recentering to highly dissipating - by simply varying a number and/or characteristics of SMA components.

A concept of adaptive behavior has been an underlying theme of active control of structures, which are subjected to earthquake and other environmental, or uncontrolled, type of loads. The structure adapts its dynamic characteristics to meet the performance objectives at any instant when the "load" the structure is designed to withstand takes place. For a futuristic smart bridge system, a thermomechanical approach to develop a constitutive relation for bending of a composite beam with continuous SMA fibers embedded eccentric to neutral axis can be implemented. Based on the study presented in this Dissertation, it can be concluded that SMAs can be successfully used for active vibration control of complex structures. Since, a bridge structure is a composite in nature SMA reinforcement along with passive components (e.g., concrete, stainless steel) can

facilitate the structure to respond more effectively to undesirable vibrations due to activation of the SME .

Two families of passive seismic control devices exploiting the unique properties of SMA kernel components are being investigated within the Memory Alloys for New Seismic Isolation and Energy Dissipation Devices (MANSIDE) (Bernardini et al., 1999) project. They are Special braces for framed structures and isolation devices for buildings and bridges.

Another area for using SMAs in composite materials is by incorporating them as smart material tags. These tags can be used to monitor from the exterior of the structure the internal condition of the structure. Monitoring is conducted for stress levels, moisture content, and presence of voids, development of cracks as well as their propagation and discontinuities.

SMAs can also be used as self-stressing fibers and, therefore, be applied for retrofitting. Self-stressing fibers are the ones in which the SMA reinforcements are placed into the composite in a non-stressed state. A pre-stressing force is applied to the SMAs. Thermomechanical treatment can be applied at any time after hardening of the matrix instead of during its curing and hardening. Long or short term pre-stressing is introduced by triggering the change in SMAs shape using temperature or electricity.

In this Dissertation NiTiNOL in the form of ribbons (characterized by rectangular cross-sections) was used in the investigations. However, the approach can be extended to

any NiTiNOL based structures. In aerospace engineering, the concept of the "smart wing" is becoming popular. A design that uses sputter deposited NiTiNOL on an airfoil can be envisioned as a candidate for the "smart wing". NiTiNOL is sputter deposited in a controlled vacuum environment on an airfoil. The structure is then subjected to a heat treatment process in order to eliminate residual strains, if any, due to the manufacturing process. Also, this step facilitates proper setting of the TT. Dynamic testing based on the OEH method can be conducted on the airfoil to obtain its frequency response. The material properties can be extracted from the "composite" airfoil based on a similar approach that was used for generic NiTiNOL based composites as discussed in this Dissertation. Figure 9.1 shows a schematic representation for testing of an airfoil using the OEH methodology. The airfoil could be mounted with specific boundary conditions. However, for this discussion, cantilever boundary conditions have been applied.

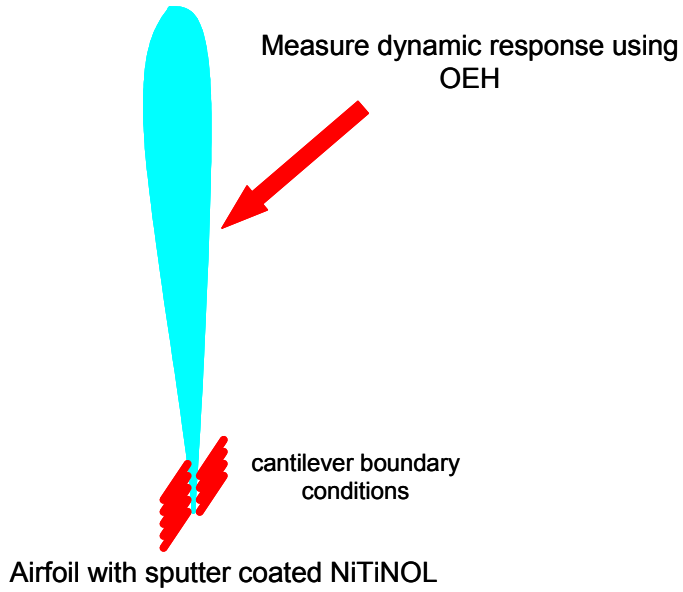

Fig. 9.1. OEH testing of an airfoil sputter coated with NiTiNOL.

During the testing process, temperature dependent resonant frequencies can be obtained. Using a similar material law to that used in characterization of NiTiNOL based composites, as discussed earlier in the Dissertation, the material properties can be extracted. This method is useful in developing a technique in which the response can be determined based on the measured material properties. This determination is achieved using either a material law (i.e., an interpolation function) developed using experimental results, or using the analytical model developed that is based on material properties as, e.g., determined by OEH. Both of these simulation techniques are advantageous as actual testing is not required for the composite airfoil. Figure 9.2 displays a flow chart representation of the process for testing and evaluation of a hybrid airfoil that uses NiTiNOL as the active component. Using NiTiNOL on airfoil can result in active vibration response modification of the structure.

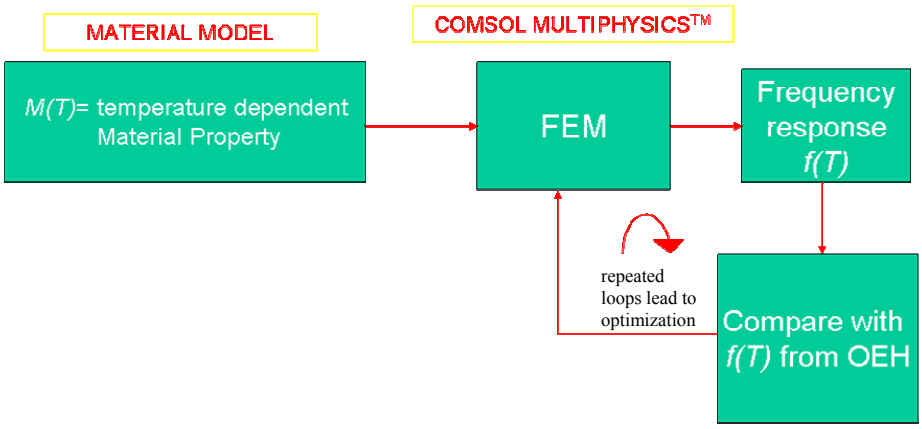

Fig. 9.2. Flow chart representing a process for testing of NiTiNOL coated airfoil.

Shape memory alloys have the unique ability to recover up to 11% plastic strain as a result of a phase transformation from Martensite to Austenite. Impact damage is common in automobile accidents. Repair of damage to the frame as well as other parts of the structure costs drivers as well as insurance companies billions of dollars every year. A situation where, using automobile frames made of SMAs, it would be possible to reverse the damage to the structure by changing temperature alone may be feasible. Also, if superelastic SMAs are used, then the structure could rebound to the undamaged state once the loading has ceased. However, the important factor that has to be taken into consideration is the cost of using SMAs in automobile chassis designs. It is, however, possible to use SMAs along with other conventional materials such as Aluminum to develop a suitable composite. After proper thermomechanical treatment the NiTiNOL composite can be trained to absorb deformations within allowable limits (not greater than 11% strain). Also, using SMAs like NiTiNOL could affect corrosion behavior of frames for automobiles especially in areas where salt is a problem during winter months. When properly engineered from a structural and metallurgical point of view, it is possible to employ SMAs (particularly NiTiNOL) in automotive chassis designs.

Also, utilizing unique properties of SMAs, new energy storage devices can be developed. These devices would have potentially high energy to volume ratios which would make them favorable for any application that is space/size-conscious.

The discussion presented in this Section, particularly the potential use of SMAs in automotive chassis design in order to absorb impact energy and also to utilize the shape recovery aspect of this unique engineering alloy, are just some of possible applications that have not, in my opinion, been adequately explored and implemented heretofore.

10. REFERENCES

Barishpolsky, B. M., 1980, "A combined experimental and numerical method for the solution of generalized elasticity problems," *Exp. Mech*., 20:1-5.

Baz, A., and J. Ro, 1992, "Thermodynamic characteristics of NiTiNOL-reinforced composite beams," *Composite Engineering*, 2:527-542.

Baz, A., S. Poh, J. Ro, and J. Gilheany, 1994,"Control of the natural frequencies of NiTiNOL-reinforced composite beams," *J. Sound and Vibration*, 185:171-185.

Bernardini, F., P. Gasperini, G. Valensise, and E. Boschi, 1999, "Defining seismogenic sources from historical earthquake felt reports," *Bulletin of the Seismological Society of America*, 89:94-110.

Boyd, J. G., and K. Lagoudas, 1995, "Microthermodynamic analysis of the shape memory effect in composite materials," *Center for Mechanics of Composites, Aerospace Engineering Department*, pp. 198-209, College-Station, TX.

Brinson, L. C., A. Bekker, and S. Hwang, 1996, "Deformation of shape memory alloys due to thermo-induced transformation," *J. Intelligent Material Systems and Structures*, 7:97-107.

Buehler, W. J., and J. W. Gilfrich, and R. C. Wiley, 1963, "Effect of low-temperature phase changes on the mechanical properties of alloys near composition TiNi ," *J. Appl. Phys.*, 34:1475-1477.

Burkart, M. W., and T. A. Read, 1953, "Diffusionless phase change in the Inidium-Thallium system," *Trans. AIME*, 197:1516-1524.

Chang, L. C., and T. A. Read, 1951, "NiTi, the mechanism of phase transformation," *Trans.* AIME, 189:47-51.

Chattopadhyay, G., and H. Kleykamp, 1983, "Phase Equilibria and Thermodynamic Studies in the Titanium--Nickel and Titanium--Nickel--Oxygen Systems," *Z. Metallkd*. Vol. 74, no. 3, pp. 182-187.

Chen, C. W., 1957, "Some characteristics of the Martensite transformation of Cu-Al-Ni alloy," *Trans. of AIME*, 209:1202-1203.

Duerig, T. W., 1990, "Engineering aspects of shape memory alloys," Butterworth-Heinemann, London, England.

Eckelmeyer, E. K., 1976, "Titanium nickelide. Structure and properties," *Scripta Met.*, 10: 667-674.
Escher, K., and M. Huhner, 1990, "Metallographical preparation of NiTi Shape Memory Alloys," *Praktishe Metallographie*, 27:231-235.

Falk, F., 1980, "Model free energy, mechanics, and thermodynamics of shape memory alloys," *Acta Metallurgica,* 28:1773-1780.

Femlab, 2005, *Femlab® Structural module user guide*, Version 3.2, Burlington MA.

Ford, D. S., and S. R. White, 1995, "Thermomechanical behavior of 55Ni45Ti NiTiNOL,"*Acta Metallurgica*, 44:2295-2307.

Gandhi, M. V., and B. S. Thompson, 1995, "Smart materials and structures," Chapman and Hall, New York, NY.

Hass® , 2001, *V5 series guide for programming and tooling and operator manual*, Dublin, OH.

Hariharan P., and B. F. Oreb, 1986, "Stroboscopic holographic interferometry: application of digital techniques," *Opt. Commun.*, 59:83.

Hissaki, T., Y. Shinya, and, H. Takashi, 1996, "Cyclic deformation properties of TiNi shape memory alloy under thermomechanical loading," *Proc. ICIM/ECSSM Conf.,* pp. 452-457, Lyon, France.

Hoffmann, K. H., and J. Sprekels, 1987, "Phase transitions in shape memory alloys I: stability and optimal control," *J. Numerical Functional Analytical and Optimization*, 9:743-760.

Honma, T., Y. Miwa, and N. Iguchi, 1981, "Twinning accommodation mechanism in shape memory alloys," *Proc. of the Jap. Soc. of Mech. Eng.,* No. 813-5, pp. 82-93.

Honma, T., 1987, "Martensitic transformation in shape memory alloys," *Proc. Int. Conf. on Martensitic Trans. '86*, ed. Tamura, I., pp. 709-754.

Hornbogen, E., and G. Wassermann, 1956, " On the martensitic transformations," *Z. Metallka.*, 47:427-433.

Hornbogen, E., 1995,"Shape memory materials,"*New horizon of materials*, 45:pp. 111-122.

Hornbogen, E., 1989," Shape memory materials,"*Practical Metallurgy*, 26:279-294.

Hornbogen, E., and E. Kobus, 1993,"Characterization of shape memory alloys by hardness indentations,"*Praktishe Metallographie*, 30:507-518.

Humbeeck, J. V., R. Stalmans, M. Chandrashekaran, and L. Delaey, 1990," On the stability of shape memory alloys," *Engineering aspects of shape memory alloys*, p. 96, Butterworth-Heinemann, London, England.

Ineichen B., and J. Mastner, 1980, "Vibration analysis by stroboscopic two-reference beam heterodyne holographic interferometry," *Optics Applied to Metrology*, SPIE-210:207-212.

Kardestuncer, H., and R. J. Pryputniewicz, "Unification of FEM with laser experimentation," *NATO Advanced Science Institute Series on Optical Metrology*, Martinus Nijhoff, Dordreht, Netherlands, pp. 365-392.

Lee, R. N., and R. Withers, 1978, "Search for the electronic phase transition in NiTi", *J. of App. Phy.*, Vol. 49, Issue 11, pp. 5488-5492.

Macek, T., and J. M., Pitarresi, 1993, "Structural optimization of an electrical spring contact," *IEEE*, 569:1125-1134.

Mizar, S. P., 1999, "Thermomechanical characterization of shape memory alloys using ACES methodology," M. S. Thesis, Worcester Polytechnic Institute, Worcester, MA.

Mizar, S. P., M. I. Pech-Canul, and R. J. Pryputniewicz, 1999, "Characterization of NiTi materials using a novel ACES methodology," *Proc. MRS Symp. on Materials for smart structures III*: pp. 120-124, Boston, MA.

Mizar S. P., and R. J. Pryputniewicz, 2000, "New approach to measurements for shape memory alloys by ACES methodology," *Proc. Internat. Congress on Exp. Mech., SEM*, pp. 1013-1016, Bethel, Connecticut, CT.

Mizar S. P., and R. J. Pryputniewicz, 2003, "Characterization of NiTiNOL for smart structural systems using ACES methodology," 2003, *Proc. MRS Symp. on Materials for smart structures V*: pp. 120-124, Boston, MA.

Mizar S. P., and R. J. Pryputniewicz, 2004, "Steady state vibration control of NiTi based structures ," *Proc. of IMAC XXII*, pp. 115-119, Dearborn, MI.

Muller, I., 1986,"Shape memory alloys-phenomenology and simulation," pp. 23-35, Hermann-Fottinger-Institut, Berlin, Germany.

Nishida, M., and T. Honma, 1984, "All-round shape memory effect in Ni-rich TiNi alloys generated by constrained aging," *Scripta Metallurgica*, 18:1293-1307.

Nishiyama, Z., 1978, "*Martensitic transformations*," Academic Press, New York, NY.

Otsuka, T., 1998, *Shape memory materials*, p. 07, Cambridge University Press, Cambridge, England.

Perkins, J., 1975, ed.,"Shape memory effects in alloys", Plenum Press, New York, NY.

Powell, R. L., and K. A. Stetson, 1965, "Interferometric vibration analysis by wavefront reconstruction," *J. Opt. Soc. Am.*, 55:1593.

Pruski, A., and H. Kihl, 1992,"Shape memory alloy hysteresis," *Sensors and Actuators A*, 36:29-35.

Pryputniewicz, D. R., 1997 "ACES approach to the development of micro-components," M.S. Thesis, Worcester Polytechnic Institute, Worcester MA.

Pryputniewicz, R. J., 1980, "State-of-the-art in hologrammetry and related fields," *Internat. Arch. of Photogrammetry*, pp. 35-41.

Pryputniewicz, R. J., 1985, "Holographic and finite element studies of vibrating beams," *Proc. SPIE*, 599:54-62.

Pryputniewicz, R. J., 1986, "Computer aided fringe analysis," *Proc. Internat. Conf. on Holography Applications*, Beijing, China, pp. 250-257.

Pryputniewicz, R. J., 1987a, "Quantitative interpretation of time-average holograms in vibration analysis," *NATO Advanced Science Institute Series in Optical Metrology*, Martinus Nijhoff, Dordrecht, Netherlands, pp. 296-316.

Pryputniewicz, R. J., 1987b, "Review of methods for automatic analysis of fringes in hologram interferometry," *Critical Review of Optical Science and Metrology*, Boston, MA, pp. 140-148.

Pryputniewicz, R. J., 1988, "Vibration studies using heterodyne hologram interferometry," *Industrial Laser Interferometry II*, SPIE-955:154-161.

Pryputniewicz, R. J., 1990, "Automated systems for quantitative analysis of holograms," *Holography: Commemorating the 90th Anniversary of the Birth of Dennis Gabor*, P. Gregus, ed., Tatabana, Hungary, pp. 215-246.

.

Pryputniewicz, R. J., 1991, "Static and dynamic measurements using electro-optic

holography," *Photonics and Speckle Metrology*, F. P. Chen, ed., Bellingham, WA, pp. 790-798.

Pryputniewicz, R. J., 1992, "Electro-optic holography," in *SPIE critical reviews of optical science and technology*, CR-46:148-174.

Pryputniewicz, R. J., 1993, *Engineering experimentation*, Worcester Polytechnic Institute, Worcester, MA.

Pryputniewicz, R. J., 1994a, "Hybrid approach to deformation analysis," *Photomechanics*, pp. 282-296, Bellingham, WA.

Pryputniewicz, R. J., 1994b, "Quantitative determination of displacements and strains from holograms," Ch. 3 in Vol. 68 of *Springer series on optical sciences*, Springer-Verlag, Berlin, pp. 33-72.

Pryputniewicz, R. J., 1996, *Holographic numerical analysis*, Worcester Polytechnic Institute, Worcester MA.

Pryputniewicz, R. J., and K. A. Stetson, 1989, "Measurement of vibration patterns using electro-optic holography," *Proc. SPIE,* 1162:456-467.

Rogers, C. A., 1988, "Dynamic control concepts using shape memory alloy reinforced plates," *Proc. of the U.S. Army Res. Office Workshop*, September 15-16, Blacksburg, VA.

Rogers, C.A., C. Liang, and J. Jia., 1989, "Behavior of shape memory alloy reinforced composite plates," *AIAA*, 89:1389-1395.

Rondelli, G., B. Vicetini, and A. Cigada, 1988, "Corrosion properties of NiTi shape memory alloys," *Proc. of the MRS Inter. Meeting on Adv. Mat.*, Vol. 9. Shape Memory Materials, Tokyo, Japan, pp. 237-242.

Schwank, W., and J. Huber, 1974, "Analysis of passive film on Ni-Ti," SAMPE QUART 5: 17-20.

Shimizu, K., T. Tadaki, and K. Asayama, 1984, "Some observations of Ausageing effects on the martensitic transformation in an Fe--Ni--Ti alloy," *Trans. Jpn. Inst. Met.*, Vol. 25, no. 2, pp. 80-88.

Stetson, K. A., 1970,"Effects of beam modulation on fringe loci and localization in time-average hologram interferometry," *J. Opt. Soc. Am.*, 60:1378-1384.

Stetson, K. A., 1982, "Method of vibration measurements in heterodyne interferometry," *Opt. Lett.*, 7:233-234.

Stetson, K. A., and Brohinsky, W. E., 1988, "Fringe-shifting technique for numerical analysis of time-average holograms of vibrating objects," *J. Opt. Soc. Am.-A*, 5:1472-1476.

Stetson, K. A., and Brohinsky, W. E., 1987, "An electro-optic holography system for vibration analysis and nondestructive testing," *Proc. SPIE*, 746:44-51.

Suhir, E., 1989, "Analytical modeling of electronic packaging structures: its merits, shortcomings and interaction with experimental and numerical techniques", *J. of Electronic Packaging*, 111:157-161.

Tanaka, K., 1986, "A thermomechanical sketch of shape memory effect: one-dimensional tensile behavior," *Research Mechanica*, p. 251-263, Elsevier Applied Science Publishers Ltd, London, England.

Tanaka, K., 1990, "A phenomenological description on thermomechanical behavior of shape memory alloys,"*Trans. of the ASME*, 112:158-163

Tobushi, H., Y. Ohashi, T. Hori, and H. Yamamoto, 1992, "Cyclic deformation of NiTi shape-memory alloy helical spring," *Exp. Mech.*, 32:304-308.

Trochu, F., 1996, "Shape memory alloys: fundamentals and modeling", *Center for Applied Research on Polymers, Ecole d'Etude et de Modelisation sur les Materiaux et Methodes de fabrication*, p. 5-9, Montreal, Canada.

Vest, C. M., 1979, *Holographic interferometry*, Wiley, New York, NY.

Vicentini, B., G. Rondelli, A. Cigada, and Turisini, G., 1986, "Corrosion behavior of a nickel titanium alloy," Shape memory alloy 86, China Academic Publishers, Beijing, China, p. 447.

Wasilewski, R. J., S. R. Butler, and J. E. Hanlon, 1974, "Structure of Ni_3 Ti," *Met. Sci. J.*, 1:104-110.

Wayman, C. M., and T. W. Duerig, 1990, "An introduction to Martensite and shape memory", *Engineering aspects of shape memory alloys*, pp. 3-15, Butterworth-Heinemann, London, England.

Wick A., O. Vohringer, and A. R. Pelton, 1995, "The bending behavior of NiTi", *J. de Physique IV*, 5:789-794.

Whitney, J. M., and J. Ashton, 1987, "Structural analysis of laminated anisotropic plates," Technomic Publishing Company, Lancaster, PA.

APPENDIX A. FEM analysis

The following file represents a typical output generated by FEMLAB®. This file was generated for a NiTiNOL sample undergoing a thermomechanical phase transformation. Based on this analysis, the temperature dependent resonant frequencies were compared to measured values from OEH.

```
% FEMLAB Model M-file
% Generated by FEMLAB 3.1i (FEMLAB 3.1.0.163, $Date: 2005/04/07 13:19:21
$)

flclear fem

% Femlab version
clear vrsn
vrsn.name = 'FEMLAB 3.1';
vrsn.ext = 'i';
vrsn.major = 0;
vrsn.build = 163;
vrsn.rcs = '$Name:  $';
vrsn.date = '$Date: 2005/04/07 13:19:21 $';
fem.version = vrsn;

% Geometry
g1=block3('2.25e-3','25.4e-3','0.5e-
3','base','corner','pos',{'0','0','0'},'axis',{'0','0','1'},'rot','0');
clear s
s.objs={g1};
s.name={'BLK1'};
s.tags={'g1'};

fem.draw=struct('s',s);
fem.geom=geomcsg(fem);

% (Default values are not included)

% Application mode 1
clear appl
appl.mode.class = 'SmeSolid3';
```

```
appl.module = 'SME';
appl.gporder = 4;
appl.cporder = 2;
appl.assignsuffix = '_solid3';
clear prop
prop.analysis='eigen';
appl.prop = prop;
clear bnd
bnd.Hx = {0,1};
bnd.Hy = {0,1};
bnd.Hz = {0,1};
bnd.ind = [1,2,1,1,1,1];
appl.bnd = bnd;
clear equ
equ.E = 35e9;
equ.rho = 6500;
equ.ind = [1];
appl.equ = equ;
fem.appl{1} = appl;
fem.border = 1;

% Multiphysics
fem=multiphysics(fem);
```

The following file represents a typical output file generated by FEMLAB®. This file was generated for a NiTiNOL based composite. Based on this analysis the temperature dependent resonant frequencies were compared to measured values from OEH.

```
% COMSOL Multiphysics Model M-file
% Generated by COMSOL 3.2 (COMSOL 3.2.0.222, $Date: 2005/09/01 18:02:30
$)

% (Default values are not included)

% Application mode 1
clear appl
appl.mode.class = 'SmeSolid3';
appl.module = 'SME';
appl.shape = {};
appl.gporder = {};
appl.cporder = {};
appl.sshape = 2;
appl.assignsuffix = '_smsld';
clear prop
prop.analysis='eigen';
appl.prop = prop;
clear pnt
pnt.Hy = {};
pnt.R = {};
pnt.FyAmp = {};
pnt.Fx = {};
pnt.Hx = {};
pnt.FzPh = {};
pnt.H = {};
pnt.Hz = {};
pnt.constrcoord = {};
pnt.Rz = {};
pnt.FxAmp = {};
pnt.Fz = {};
pnt.Rx = {};
pnt.loadcoord = {};
pnt.Ry = {};
```

```
pnt.FxPh = {};
pnt.Fy = {};
pnt.FzAmp = {};
pnt.constrtype = {};
pnt.name = {};
pnt.FyPh = {};
pnt.ind = [];
appl.pnt = pnt;
clear edg
edg.Hy = {};
edg.R = {};
edg.FyAmp = {};
edg.Fx = {};
edg.Hx = {};
edg.FzPh = {};
edg.H = {};
edg.Hz = {};
edg.constrcoord = {};
edg.Rz = {};
edg.FxAmp = {};
edg.Fz = {};
edg.Rx = {};
edg.loadcoord = {};
edg.Ry = {};
edg.FxPh = {};
edg.Fy = {};
edg.FzAmp = {};
edg.constrtype = {};
edg.name = {};
edg.FyPh = {};
edg.ind = [];
appl.edg = edg;
clear bnd
bnd.Hy = {};
bnd.R = {};
bnd.FyAmp = {};
bnd.Fx = {};
bnd.Hx = {};
bnd.FzPh = {};
bnd.H = {};
bnd.Hz = {};
bnd.constrcoord = {};
bnd.Rz = {};
bnd.FxAmp = {};
```

```
bnd.Fz = {};
bnd.Rx = {};
bnd.loadcoord = {};
bnd.Ry = {};
bnd.FxPh = {};
bnd.Fy = {};
bnd.FzAmp = {};
bnd.constrtype = {};
bnd.name = {};
bnd.FyPh = {};
bnd.ind = [];
appl.bnd = bnd;
clear equ
equ.C10 = {};
equ.betadK = {};
equ.FyAmp = {};
equ.FzPh = {};
equ.Sys = {};
equ.Hz = {};
equ.Tflag = {};
equ.ETiso = {};
equ.syzi = {};
equ.alphavector = {};
equ.FxAmp = {};
equ.sxzi = {};
equ.Ey = {};
equ.syi = {};
equ.Rx = {};
equ.ezi = {};
equ.szi = {};
equ.nuxy = {};
equ.ini_strain = {};
equ.ETkin = {};
equ.FyPh = {};
equ.alpha = {};
equ.D = {};
equ.mu = {};
equ.alphadM = {};
equ.R = {};
equ.Tempref = {};
equ.Hx = {};
equ.rho = {};
equ.Gxy = {};
equ.Ez = {};
```

```
equ.Shard = {};
equ.exzi = {};
equ.nuyz = {};
equ.Syfunc_kin = {};
equ.mixedform = {};
equ.FxPh = {};
equ.ini_stress = {};
equ.Ex = {};
equ.yieldtype = {};
equ.dinit = {};
equ.exi = {};
equ.init = {};
equ.Fx = {};
equ.sxyi = {};
equ.hardeningmodel = {};
equ.H = {};
equ.cporder = {};
equ.Rz = {};
equ.materialcoord = {};
equ.eyzi = {};
equ.alphax = {};
equ.materialmodel = {};
equ.loadcoord = {};
equ.Ry = {};
equ.nuxz = {};
equ.usage = {};
equ.FzAmp = {};
equ.nu = {};
equ.kappa = {};
equ.constrtype = {};
equ.name = {};
equ.sxi = {};
equ.hypertype = {};
equ.Hy = {};
equ.Temp = {};
equ.Gyz = {};
equ.Syfunc = {};
equ.constrcoord = {};
equ.isodata = {};
equ.Fz = {};
equ.gporder = {};
equ.Gxz = {};
equ.alphay = {};
equ.C01 = {};
```

```
equ.exyi = {};
equ.Fy = {};
equ.alphaz = {};
equ.eyi = {};
equ.E = {};
equ.ind = [];
appl.equ = equ;
fem.appl{1} = appl;
fem.sdim = {'x','y','z'};
fem.border = 1;
fem.units = 'SI';

% Multiphysics
fem=multiphysics(fem);
% COMSOL Multiphysics Model M-file
% Generated by COMSOL 3.2 (COMSOL 3.2.0.222, $Date: 2005/09/01 18:02:30
$)

% Geometry
g1=block3('30e-3','30e-3','0.6e-
3','base','corner','pos',{'0','0','0'},'axis',{'0','0','1'},'rot','0');
g2=block3('2.25e-3','29.5e-3','0.5e-3','base','corner','pos',{'2.25e-3','0.1e-
3','0'},'axis',{'0','0','1'},'rot','0');
clear g2
g3=block3('2.25e-3','29e-3','0.5e-3','base','corner','pos',{'2.25e-3','0.5e-
3','0'},'axis',{'0','0','1'},'rot','0');
garr=geomarrayr(g3,2.25e-3,0,0,1,1,1);
[g4]=deal(garr{:});
garr=geomarrayr(g3,2.25e-3,0,0,4,1,1);
[g5,g6,g7,g8]=deal(garr{:});
clear g6 g7 g8
garr=geomarrayr(g3,4.5e-3,0,0,4,1,1);
[g9,g10,g11,g12]=deal(garr{:});
garr=geomarrayr(g10,4.5e-3,0,0,3,1,1);
[g13,g14,g15]=deal(garr{:});
garr=geomarrayr(g11,4.5e-3,0,0,3,1,1);
[g16,g17,g18]=deal(garr{:});
garr=geomarrayr(g12,4.5e-3,0,0,3,1,1);
[g19,g20,g21]=deal(garr{:});
g22=block3('30e-3','30e-3','0.25e-
3','base','corner','pos',{'0','0','0.5'},'axis',{'0','0','1'},'rot','0');
clear g22
g23=block3('30e-3','30e-3','0.25e-3','base','corner','pos',{'0','0','0.5e-
3'},'axis',{'0','0','1'},'rot','0');
```

```
g24=geomcomp({g1,g3,g10,g11,g12,g14,g15,g17,g18,g20,g21,g23},'ns',{'BLK1','
BLK2','BLK3','BLK4','BLK5','BLK6','BLK7','BLK8','BLK9','BLK10','BLK11','BLK12'},
'sf','BLK1+BLK2+BLK3+BLK4+BLK5+BLK6+BLK7+BLK8+BLK9+BLK10+BLK11
+BLK12','face','none','edge','all');
clear s
s.objs={g24};
s.name={'CO1'};
s.tags={'g24'};

fem.draw=struct('s',s);
fem.geom=geomcsg(fem);

% Initialize mesh
fem.mesh=meshinit(fem);

% Initialize mesh
fem.mesh=meshinit(fem, ...
                  'hmaxfact',5, ...
                  'hcurve',1, ...
                  'hgrad',2, ...
                  'hcutoff',0.07, ...
                  'hnarrow',0.1);

% (Default values are not included)

% Application mode 1
clear appl
appl.mode.class = 'SmeSolid3';
appl.module = 'SME';
appl.gporder = 4;
appl.cporder = 2;
appl.border = 'on';
appl.assignsuffix = '_smsld';
clear prop
prop.analysis='eigen';
appl.prop = prop;
clear bnd
bnd.Hy = {0,1};
bnd.Hx = {0,1};
bnd.Hz = {0,1};
bnd.ind = [1,2,1,1,2,1,1,2,1,1,1,1,1,1,2,1,1,1,1,1,2,1,1,1,1,1,2,1,1,1, ...
  1,1,2,1,1,1,1,1,2,1,1,1,1,1,2,1,1,1,1,1,1,1];
appl.bnd = bnd;
clear equ
```

```
equ.alpha = {'mat2_alpha',1.2e-5};
equ.rho = {'mat2_rho',6100};
equ.E = {'mat2_E',35e9};
equ.ind = [1,1,1,2,2,2,2,2,2];
appl.equ = equ;
fem.appl{1} = appl;
fem.border = 1;
fem.units = 'SI';

% Library materials
clear lib
lib.mat{1}.name='POLYMERS';
lib.mat{1}.varname='mat1';
lib.mat{2}.name='Polythene';
lib.mat{2}.varname='mat2';
lib.mat{2}.variables.k='0.38';
lib.mat{2}.variables.epsilonr='2.3';
lib.mat{2}.variables.rho='2200';
lib.mat{2}.variables.C='1900';
lib.mat{2}.variables.alpha='150e-6';
lib.mat{2}.variables.E='1e9';


fem.lib = lib;

% Multiphysics
fem=multiphysics(fem);

% Extend mesh
fem.xmesh=meshextend(fem);

% Solve problem
fem.sol=femeig(fem, ...
            'symmetric','on', ...
            'solcomp',{'w','u','v'}, ...
            'outcomp',{'w','u','v'}, ...
            'linsolver','spooles');

% Save current fem structure for restart purposes
fem0=fem;

% Plot solution
postplot(fem, ...
       'slicedata',{'mises_smsld','cont','internal'}, ...
```

```
        'slicexspacing',5, ...
        'sliceyspacing',0, ...
        'slicezspacing',0, ...
        'slicemap','jet(1024)', ...
        'solnum',1, ...
        'title','eigfreq_smsld(1)=199.794712    Slice: von Mises stress [N/m^2]', ...
        'refine',3, ...
        'grid','on', ...
        'campos',[1.49999996647239,1.49999996647239,21.2540172660291], ...
        'transparency',0.10000000000000014, ...
        'renderer','opengl');

% Plot solution
postplot(fem, ...
        'tetdata',{'disp_smsld','cont','internal'}, ...
        'tetmap','jet(1024)', ...
        'tetkeep',1, ...
        'tetkeeptype','random', ...
        'deformsub',{'u','v','w'}, ...
        'solnum',1, ...
        'title','eigfreq_smsld(1)=199.794712    Subdomain: Total displacement [m]
Deformation: Displacement [m]', ...
        'refine',3, ...
        'grid','on', ...
        'campos',[1.49999996647239,1.49999996647239,21.2540172660291], ...
        'transparency',0.10000000000000014, ...
        'renderer','opengl');

% Plot solution
postplot(fem, ...
        'tetdata',{'disp_smsld','cont','internal'}, ...
        'tetedgestyle',[1.0,0.0,0.0], ...
        'tetfacestyle',[1.0,0.0,0.0], ...
        'tetkeep',1, ...
        'tetkeeptype','random', ...
        'deformsub',{'u','v','w'}, ...
        'solnum',1, ...
        'title','eigfreq_smsld(1)=199.794712    Subdomain: Total displacement [m]
Deformation: Displacement [m]', ...
        'refine',3, ...
        'grid','on', ...
        'campos',[1.49999996647239,1.49999996647239,21.2540172660291], ...
        'transparency',0.10000000000000014, ...
        'renderer','opengl');
```

```
% Plot solution
postplot(fem, ...
        'tetdata',{'disp_smsld','cont','internal'}, ...
        'tetedgestyle',[1.0,0.0,0.0], ...
        'tetfacestyle',[1.0,0.0,0.0], ...
        'tetkeep',1, ...
        'tetkeeptype','random', ...
        'deformsub',{'u','v','w'}, ...
        'solnum',1, ...
        'title','eigfreq_smsld(1)=199.794712    Subdomain: Total displacement [m]
Deformation: Displacement [m]', ...
        'refine',3, ...
        'grid','on', ...
        'campos',[1.49999996647239,1.49999996647239,21.2540172660291], ...
        'transparency',0.10000000000000014, ...
        'renderer','opengl');

% Plot solution
postplot(fem, ...
        'tetdata',{'disp_smsld','cont','internal'}, ...
        'tetmap','hot(1024)', ...
        'tetkeep',1, ...
        'tetkeeptype','random', ...
        'deformsub',{'u','v','w'}, ...
        'solnum',1, ...
        'title','eigfreq_smsld(1)=199.794712    Subdomain: Total displacement [m]
Deformation: Displacement [m]', ...
        'refine',3, ...
        'grid','on', ...
        'campos',[15.6744133791513,4.31113380483847,15.5721109009936], ...
        'transparency',0.10000000000000014, ...
        'renderer','opengl');

% Plot solution
postplot(fem, ...
        'tetdata',{'disp_smsld','cont','internal'}, ...
        'tetmap','hot(1024)', ...
        'tetkeep',1, ...
        'tetkeeptype','random', ...
        'deformsub',{'u','v','w'}, ...
        'solnum',1, ...
        'title','eigfreq_smsld(1)=199.794712    Subdomain: Total displacement [m]
Deformation: Displacement [m]', ...
```

```
        'refine',3, ...
        'grid','on', ...
        'campos',[15.6744133791513,4.31113380483847,15.5721109009936], ...
        'transparency',0.10000000000000014, ...
        'renderer','opengl');

% (Default values are not included)

% Application mode 1
clear appl
appl.mode.class = 'SmeSolid3';
appl.module = 'SME';
appl.gporder = 4;
appl.cporder = 2;
appl.border = 'on';
appl.assignsuffix = '_smsld';
clear prop
prop.analysis='eigen';
appl.prop = prop;
clear bnd
bnd.Hy = {0,1};
bnd.Hx = {0,1};
bnd.Hz = {0,1};
bnd.ind = [1,2,1,1,2,1,1,2,1,1,1,1,1,1,2,1,1,1,1,1,2,1,1,1,1,1,2,1,1,1, ...
  1,1,2,1,1,1,1,1,2,1,1,1,1,1,2,1,1,1,1,1,1,1];
appl.bnd = bnd;
clear equ
equ.alpha = {'mat2_alpha',1.2e-5};
equ.rho = {'mat2_rho',6100};
equ.E = {'mat2_E',83e9};
equ.ind = [1,1,1,2,2,2,2,2,2];
appl.equ = equ;
fem.appl{1} = appl;
fem.border = 1;
fem.units = 'SI';

% Library materials
clear lib
lib.mat{1}.name='POLYMERS';
lib.mat{1}.varname='mat1';
lib.mat{2}.name='Polythene';
lib.mat{2}.varname='mat2';
lib.mat{2}.variables.k='0.38';
lib.mat{2}.variables.epsilonr='2.3';
```

```
lib.mat{2}.variables.rho='2200';
lib.mat{2}.variables.C='1900';
lib.mat{2}.variables.alpha='150e-6';
lib.mat{2}.variables.E='1e9';


fem.lib = lib;

% Multiphysics
fem=multiphysics(fem);

% Extend mesh
fem.xmesh=meshextend(fem);

% Solve problem
fem.sol=femeig(fem, ...
            'init',fem0.sol, ...
            'symmetric','on', ...
            'solcomp',{'w','u','v'}, ...
            'outcomp',{'w','u','v'}, ...
            'linsolver','spooles');

% Save current fem structure for restart purposes
fem0=fem;

% Plot solution
postplot(fem, ...
        'tetdata',{'disp_smsld','cont','internal'}, ...
        'tetmap','hot(1024)', ...
        'tetkeep',1, ...
        'tetkeeptype','random', ...
        'deformsub',{'u','v','w'}, ...
        'solnum',1, ...
        'title','eigfreq_smsld(1)=288.99397    Subdomain: Total displacement [m]
Deformation: Displacement [m]', ...
        'refine',3, ...
        'grid','on', ...
        'campos',[20.6683403622737,0.288884983596204,9.05129675057639], ...
        'transparency',0.10000000000000014, ...
        'renderer','opengl');

% Plot solution
postplot(fem, ...
        'tetdata',{'disp_smsld','cont','internal'}, ...
```

```
        'tetedgestyle','none', ...
        'tetfacestyle','flat', ...
        'tetmap','hot(1024)', ...
        'tetkeep',1, ...
        'tetkeeptype','random', ...
        'deformsub',{'u','v','w'}, ...
        'solnum',1, ...
        'title','eigfreq_smsld(1)=288.99397    Subdomain: Total displacement [m]
Deformation: Displacement [m]', ...
        'refine',3, ...
        'grid','on', ...
        'campos',[-7.38612811726988,20.5400010266473,-2.90455577646462], ...
        'transparency',0.10000000000000014, ...
        'renderer','opengl');

% Plot solution
postplot(fem, ...
        'tetdata',{'disp_smsld','cont','internal'}, ...
        'tetedgestyle','none', ...
        'tetfacestyle','flat', ...
        'tetmap','hot(1024)', ...
        'tetkeep',1, ...
        'tetkeeptype','random', ...
        'deformsub',{'u','v','w'}, ...
        'solnum',2, ...
        'title','eigfreq_smsld(2)=663.607032    Subdomain: Total displacement [m]
Deformation: Displacement [m]', ...
        'refine',3, ...
        'grid','on', ...
        'campos',[-9.71420853748234,-13.1133135887016,10.7742546339652], ...
        'transparency',0.10000000000000014, ...
        'renderer','opengl');

% Plot solution
postplot(fem, ...
        'tetdata',{'disp_smsld','cont','internal'}, ...
        'tetedgestyle','none', ...
        'tetfacestyle','flat', ...
        'tetmap','hot(1024)', ...
        'tetkeep',1, ...
        'tetkeeptype','random', ...
        'deformsub',{'u','v','w'}, ...
        'solnum',3, ...
```

```
        'title','eigfreq_smsld(3)=1433.38055    Subdomain: Total displacement [m]
Deformation: Displacement [m]', ...
        'refine',3, ...
        'grid','on', ...
        'campos',[-9.71420853748234,-13.1133135887016,10.7742546339652], ...
        'transparency',0.10000000000000014, ...
        'renderer','opengl');

% Plot solution
postplot(fem, ...
        'tetdata',{'disp_smsld','cont','internal'}, ...
        'tetedgestyle','none', ...
        'tetfacestyle','flat', ...
        'tetmap','hot(1024)', ...
        'tetkeep',1, ...
        'tetkeeptype','random', ...
        'deformsub',{'u','v','w'}, ...
        'solnum',4, ...
        'title','eigfreq_smsld(4)=1985.632885    Subdomain: Total displacement [m]
Deformation: Displacement [m]', ...
        'refine',3, ...
        'grid','on', ...
        'campos',[-9.71420853748234,-13.1133135887016,10.7742546339652], ...
        'transparency',0.10000000000000014, ...
        'renderer','opengl');

% Plot solution
postplot(fem, ...
        'tetdata',{'disp_smsld','cont','internal'}, ...
        'tetedgestyle','none', ...
        'tetfacestyle','flat', ...
        'tetmap','hot(1024)', ...
        'tetkeep',1, ...
        'tetkeeptype','random', ...
        'deformsub',{'u','v','w'}, ...
        'solnum',5, ...
        'title','eigfreq_smsld(5)=2561.548168    Subdomain: Total displacement [m]
Deformation: Displacement [m]', ...
        'refine',3, ...
        'grid','on', ...
        'campos',[-9.71420853748234,-13.1133135887016,10.7742546339652], ...
        'transparency',0.10000000000000014, ...
        'renderer','opengl');
```

```
% Plot solution
postplot(fem, ...
        'tetdata',{'disp_smsld','cont','internal'}, ...
        'tetedgestyle','none', ...
        'tetfacestyle','flat', ...
        'tetmap','hot(1024)', ...
        'tetkeep',1, ...
        'tetkeeptype','random', ...
        'deformsub',{'u','v','w'}, ...
        'solnum','end', ...
        'title','eigfreq_smsld(6)=2883.11276    Subdomain: Total displacement [m]
Deformation: Displacement [m]', ...
        'refine',3, ...
        'grid','on', ...
        'campos',[-9.71420853748234,-13.1133135887016,10.7742546339652], ...
        'transparency',0.10000000000000014, ...
        'renderer','opengl');

% Plot solution
postplot(fem, ...
        'tetdata',{'disp_smsld','cont','internal'}, ...
        'tetedgestyle','none', ...
        'tetfacestyle','flat', ...
        'tetmap','hot(1024)', ...
        'tetkeep',1, ...
        'tetkeeptype','random', ...
        'deformsub',{'u','v','w'}, ...
        'solnum',1, ...
        'title','eigfreq_smsld(1)=288.99397    Subdomain: Total displacement [m]
Deformation: Displacement [m]', ...
        'refine',3, ...
        'grid','on', ...
        'campos',[1.50137806558632,1.50190852582455,21.4797746155987], ...
        'transparency',0.10000000000000014, ...
        'renderer','opengl');

% Initialize mesh
fem.mesh=meshinit(fem, ...
                'hmaxfact',1.5, ...
                'hcurve',0.7, ...
                'hgrad',1.6, ...
                'hcutoff',0.04, ...
                'hnarrow',0.4);
```

```
% Initialize mesh
fem.mesh=meshinit(fem, ...
                  'hmaxfact',3, ...
                  'hcurve',0.9, ...
                  'hgrad',1.85, ...
                  'hcutoff',0.06, ...
                  'hnarrow',0.2);

% (Default values are not included)

% Application mode 1
clear appl
appl.mode.class = 'SmeSolid3';
appl.module = 'SME';
appl.gporder = 4;
appl.cporder = 2;
appl.border = 'on';
appl.assignsuffix = '_smsld';
clear prop
prop.analysis='eigen';
appl.prop = prop;
clear bnd
bnd.Hy = {0,1};
bnd.Hx = {0,1};
bnd.Hz = {0,1};
bnd.ind = [1,2,1,1,2,1,1,2,1,1,1,1,1,1,2,1,1,1,1,1,2,1,1,1,1,1,2,1,1,1, ...
  1,1,2,1,1,1,1,1,2,1,1,1,1,1,2,1,1,1,1,1,1,1];
appl.bnd = bnd;
clear equ
equ.alpha = {'mat2_alpha',1.2e-5};
equ.rho = {'mat2_rho',6100};
equ.E = {'mat2_E',83e9};
equ.ind = [1,1,1,2,2,2,2,2,2];
appl.equ = equ;
fem.appl{1} = appl;
fem.border = 1;
fem.units = 'SI';

% Library materials
clear lib
lib.mat{1}.name='POLYMERS';
lib.mat{1}.varname='mat1';
lib.mat{2}.name='Polythene';
lib.mat{2}.varname='mat2';
```

```
lib.mat{2}.variables.k='0.38';
lib.mat{2}.variables.epsilonr='2.3';
lib.mat{2}.variables.rho='2200';
lib.mat{2}.variables.C='1900';
lib.mat{2}.variables.alpha='150e-6';
lib.mat{2}.variables.E='1e9';


fem.lib = lib;

% Multiphysics
fem=multiphysics(fem);

% Extend mesh
fem.xmesh=meshextend(fem);

% Solve problem
fem.sol=femeig(fem, ...
            'symmetric','on', ...
            'solcomp',{'w','u','v'}, ...
            'outcomp',{'w','u','v'}, ...
            'linsolver','spooles');

% Save current fem structure for restart purposes
fem0=fem;

% Plot solution
postplot(fem, ...
        'tetdata',{'disp_smsld','cont','internal'}, ...
        'tetedgestyle','none', ...
        'tetfacestyle','flat', ...
        'tetmap','hot(1024)', ...
        'tetkeep',1, ...
        'tetkeeptype','random', ...
        'deformsub',{'u','v','w'}, ...
        'solnum',1, ...
        'title','eigfreq_smsld(1)=276.64623    Subdomain: Total displacement [m]
Deformation: Displacement [m]', ...
        'refine',2, ...
        'grid','on', ...
        'campos',[1.50137806558632,1.50190852582455,21.4797746155987], ...
        'transparency',0.10000000000000014, ...
        'renderer','opengl');
```

```
% Plot solution
postplot(fem, ...
        'tetdata',{'disp_smsld','cont','internal'}, ...
        'tetedgestyle','none', ...
        'tetfacestyle','flat', ...
        'tetmap','hot(1024)', ...
        'tetkeep',1, ...
        'tetkeeptype','random', ...
        'deformsub',{'u','v','w'}, ...
        'solnum',2, ...
        'title','eigfreq_smsld(2)=636.891527    Subdomain: Total displacement [m]
Deformation: Displacement [m]', ...
        'refine',2, ...
        'grid','on', ...
        'campos',[-19.6042568756794,-2.32970986843558,-0.173707513872505],
...
        'transparency',0.10000000000000014, ...
        'renderer','opengl');

% Plot solution
postplot(fem, ...
        'tetdata',{'disp_smsld','cont','internal'}, ...
        'tetedgestyle','none', ...
        'tetfacestyle','flat', ...
        'tetmap','hot(1024)', ...
        'tetkeep',1, ...
        'tetkeeptype','random', ...
        'deformsub',{'u','v','w'}, ...
        'solnum',3, ...
        'title','eigfreq_smsld(3)=1327.102865    Subdomain: Total displacement [m]
Deformation: Displacement [m]', ...
        'refine',2, ...
        'grid','on', ...
        'campos',[-0.39730332349301,-16.1328969016632,12.0937969680868], ...
        'transparency',0.10000000000000014, ...
        'renderer','opengl');
% COMSOL Multiphysics Model M-file
% Generated by COMSOL 3.2 (COMSOL 3.2.0.222, $Date: 2005/09/01 18:02:30
$)

% Geometry
g24=rotate(g24,4.71238898038469,[0,0,1],[0,0,0]);
clear s
s.objs={g24};
```

```
s.name={'CO1'};
s.tags={'g24'};

fem.draw=struct('s',s);
fem.geom=geomcsg(fem);

% Initialize mesh
fem.mesh=meshinit(fem, ...
                  'hmaxfact',3, ...
                  'hcurve',0.9, ...
                  'hgrad',1.85, ...
                  'hcutoff',0.06, ...
                  'hnarrow',0.2);

% (Default values are not included)

% Application mode 1
clear appl
appl.mode.class = 'SmeSolid3';
appl.module = 'SME';
appl.gporder = 4;
appl.cporder = 2;
appl.border = 'on';
appl.assignsuffix = '_smsld';
clear prop
prop.analysis='eigen';
appl.prop = prop;
clear bnd
bnd.Hy = {0,1};
bnd.Hx = {0,1};
bnd.Hz = {0,1};
bnd.ind = [2,1,1,2,1,1,2,1,1,1,1,1,1,2,1,1,1,1,2,1,1,1,1,2,1,1,1,1,2,1, ...
  1,1,1,2,1,1,1,1,2,1,1,1,1,1,1,1,1,1,1,1,1,1,1,1,1,1,1,1,1,1,1,1,1,1];
appl.bnd = bnd;
clear equ
equ.alpha = {'mat2_alpha',1.2e-5};
equ.rho = {'mat2_rho',6100};
equ.E = {'mat2_E',83e9};
equ.ind = [1,1,1,2,2,2,2,2,2];
appl.equ = equ;
fem.appl{1} = appl;
fem.border = 1;
fem.units = 'SI';
```

```
% Library materials
clear lib
lib.mat{1}.name='POLYMERS';
lib.mat{1}.varname='mat1';
lib.mat{2}.name='Polythene';
lib.mat{2}.varname='mat2';
lib.mat{2}.variables.k='0.38';
lib.mat{2}.variables.epsilonr='2.3';
lib.mat{2}.variables.rho='2200';
lib.mat{2}.variables.C='1900';
lib.mat{2}.variables.alpha='150e-6';
lib.mat{2}.variables.E='1e9';


fem.lib = lib;

% Multiphysics
fem=multiphysics(fem);
```

APPENDIX B. G-code for manufacturing NiTiNOL based composites using HASS® V5 series CNC machining center

This Appendix lists the G-code that was used to machine the NiTiNOL-polymide, and NiTiNOL-Al composites using the HASS® V5 CNC machining center. The G-code is the standard CNC programming protocol (Hass®, 2001).

```
O55( PROGRAM, MIZARSAMPLE.NCF)
( FORMAT, HAAS WPI MILL.PST )
( 04/31/04 AT  3:59 PM )
( OUTPUT IN ABSOLUTE INCHES )
( PARTS PROGRAMMED, 1 )
( FIRST TOOL NOT IN SPINDLE )
N1G0G17G40G80G90G54
G49G53Z0
T1M6
( OPERATION 1, CONTOUR )
( WORKGROUP )
( TOOL 1, .0625 FINISH ENDMILL )
G54G90G0X0.Y.8548S3000M3
G43Z2.H1M8
```

```
Z.1
G1Z-.02F10.
G42X8.05F20.D51
G40X8.175
G0Z.1
( OPERATION 2, CONTOUR )
( WORKGROUP )
( TOOL 1, .0625 FINISH ENDMILL )
G90G0X0.Y.8173
G1Z-.02F10.
G41X8.05F20.D51
G40X8.175
G0Z.1
( OPERATION 3, CONTOUR )
( WORKGROUP )
( TOOL 1, .0625 FINISH ENDMILL )
G90G0X0.Y.6458
G1Z-.02F10.
G42X8.05F20.D51
G40X8.175
G0Z.1
( OPERATION 4, CONTOUR )
```

```
( WORKGROUP )
( TOOL 1, .0625 FINISH ENDMILL )
G90G0X0.Y.6083
G1Z-.02F10.
G41X8.05F20.D51
G40X8.175
G0Z.1
( OPERATION 5, CONTOUR )
( WORKGROUP )
( TOOL 1, .0625 FINISH ENDMILL )
G90G0X0.Y.4368
G1Z-.02F10.
G42X8.05F20.D51
G40X8.175
G0Z.1
( OPERATION 6, CONTOUR )
( WORKGROUP )
( TOOL 1, .0625 FINISH ENDMILL )
G90G0X0.Y.3993
G1Z-.02F10.
G41X8.05F20.D51
G40X8.175
```

```
G0Z.1
( OPERATION 7, CONTOUR )
( WORKGROUP )
( TOOL 1, .0625 FINISH ENDMILL )
G90G0X0.Y.2278
G1Z-.02F10.
G42X8.05F20.D51
G40X8.175
G0Z.1
( OPERATION 8, CONTOUR )
( WORKGROUP )
( TOOL 1, .0625 FINISH ENDMILL )
G90G0X0.Y.1902
G1Z-.02F10.
G41X8.05F20.D51
G40X8.175
G0Z.1
M9
G91G28Z0.M19
G49G53Z0
M30
%
```

```
( FILE LENGTH, 1391 CHARACTERS )

( FILE LENGTH, 11.88 FEET )

( FILE LENGTH, 3.69 METERS )
```

APPENDIX C. Simulation of G-code using GIBBSCAM®

A screen shot from GIBBSCAM® software that is used to simulate the G-code (presented in Appendix B) is presented in this Appendix, Fig. C.1. This simulation aides in testing accuracy of the parameters included in the G-code.

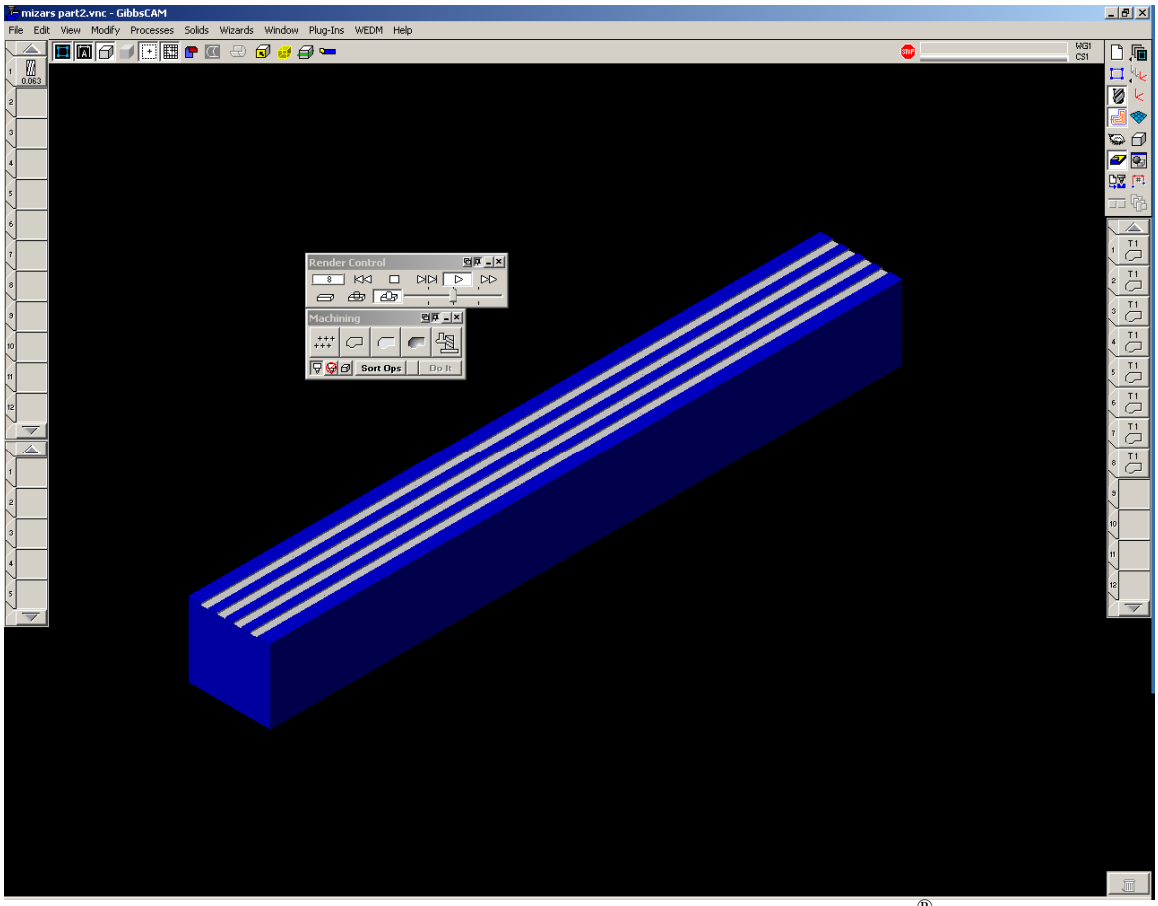

Fig. C.1. Screenshot of G-code simulation from GIBBSCAM®.

APPENDIX D. Analysis report for X-ray analysis (EDS) on NiTiNOL from SEM

This Appendix provides the analysis report obtained from the SEM. EDS was used to determine the stoichiometry of NiTiNOL.

[A N A L Y S I S R E P O R T]

GENERAL CONDITIONS

Result File	: NITI21500X
File Version	: 1
Background Method	: Fit
Decon Method	: Gaussian
Decon ChiSquared	: 1.40
Analysis Date	: 19-FEB-99
Microscope	: SEM
Comments	:

ANALYSIS CONDITIONS

Quant. Method	: XPP/ASAP
Acquire Time	: 100 secs
Normalization Factor	: 100.0

SAMPLE CONDITIONS

kV	: 15.0
Beam Current	: 0.0 picoAmps
Working Distance	: 0.0 mm
Tilt Angle	: 0.0 Degrees
TakeOff Angle	: 35.0 Degrees
Solid Angle*BeamCurrent	: 0.0

Element	Line	Weight%	K-Ratio	Cnts/s	Atomic%
O	Ka	0.00	0.0000	0.00	0.00
Al	Ka	0.13	0.0007	3.97	0.26
Si	Ka	0.32	0.0021	11.82	0.62
Ti	Ka	42.88	0.4260	934.71	47.70
Ni	Ka	56.66	0.5537	382.15	51.42
Total		99.99			

APPENDIX E. Powder diffraction files for phase identification of XRD spectrum for NiTiNOL

This Appendix provides standard powder diffraction cards that were used to identify the phases from the X-ray spectrum obtained for the NiTiNOL sample. Table F.1 shows the card that was used to identify Austenite peaks in the NiTiNOL sample, and Table F.2 shows the card used to identify the Martensite peaks in the NiTiNOL sample.

Table.F.1. 18-899 NiTiNOL 2 C Austenite.

d.	2.11	1.22	1.50	2.11	NiTiNOL 2 C Nickel ... Titanium		
I/I_1	100	60	40	100			
Rad. CuK α_1 λ 1.54050 Filter Ni Dia 114.6 mm					d. A	I/I_1	Hkl
Sys. Cubic Ref: Dwight, Trans. A.I.M.E 215 283 (1959) ao = 2.998 , CsCl type					2.111 1.496 1.222 1.059 0.948 0.865 0.801 2	100 40 60 10 30 20 70	110 200 211 220 310 222 321

Table F.2. 35 – 1281 NiTiNOL (Nickel Titanium) Martensite.

Rad. CuK α_1 λ 1.54178	d. A	Int	Hkl
Sys. Monoclinic Ref: Dwight, Trans. A.I.M.E 215 283 (1959)	4.59	6	010
	3.066	1	011
a = 2.998 , b = 4.622, c = 4.120 Obt'd from	2.865	<1	100
50 ± 0.01	2.570	13	$1\,\bar{1}\,0$
atomic % Ni, balance Ti. Hot rolled and	2.352	11	101
annealed at	2.311	2	110
973ºK for 4 hours. C.D cell a = 4.622, b =	2.295	54	020
4.120, c = 2.885, β = 96.80, a/b = 1.1218, c/b	2.181	100	$1\,\bar{1}\,1$
= 0.7002	2.060	54	002
F_{21} = 114.9 (0.009, 21)	2.016	94	111
	2.005	26	021
	1.904	1	$1\,\bar{2}\,0$
	1.879	<1	012
	1.728	8	$1\,\bar{2}\,1$
	1.696	<1	120
	1.673	<1	102
	1.607	5	$1\,\bar{1}\,2$
	1.568	<1	121
	1.538	1	112
	1.533	26	022
	1.530	1	

APPENDIX F. Additional results from OEH

Additional results from OEH pertaining to determination of the modulus of elasticity are presented in this Appendix. The experiments were repeated to check for repeatability of measurements and the experiments were repeated for active lengths of L = 39.85 mm, L = 28.82 mm, and for L = 25.0 mm. Results in addition to those presented in Chapter 8 are presented for each of these active lengths indicating the temperature dependence of the modulus of elasticity. The temperature dependence of the average modulus for each of the active lengths is also presented. Figure F.1 represents the temperature dependence of NiTiNOL for an active length L = 39.85 mm.

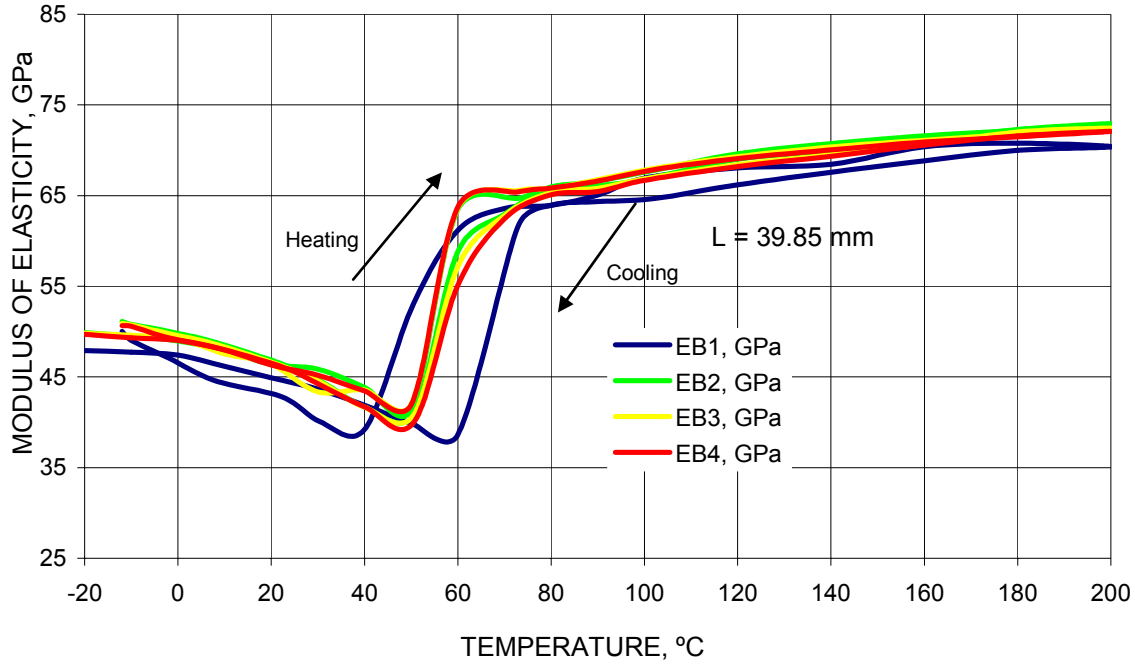

Fig. F.1. Modulus of elasticity of NiTiNOL as a function of temperature, based on the first four bending modes of 39.85 mm long sample.

Figures F.2 and F.3 indicate temperature dependence of the modulus of elasticity for active lengths of L = 28.82 mm, and L = 25.0 mm, respectively. Figure F.4 indicates the temperature dependence of the average modulus of elasticity for all three active lengths.

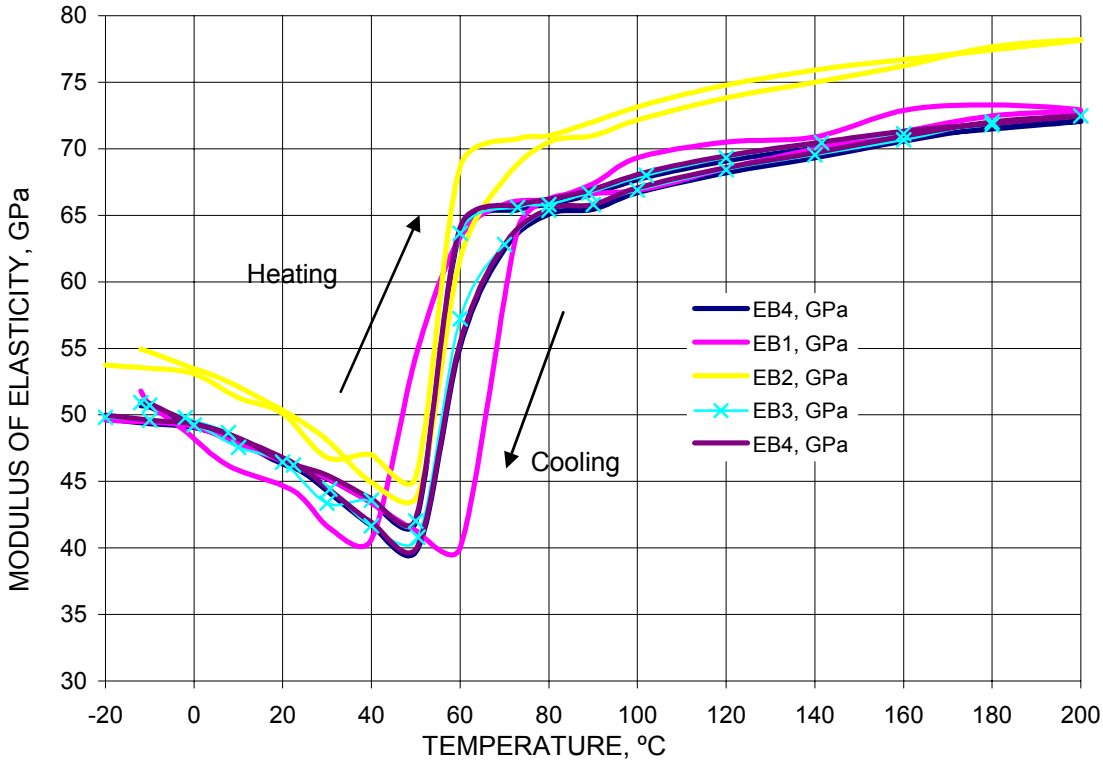

Fig. F.2. Modulus of elasticity of NiTiNOL as a function of temperature, based on the first four bending modes of 28.82 mm long sample.

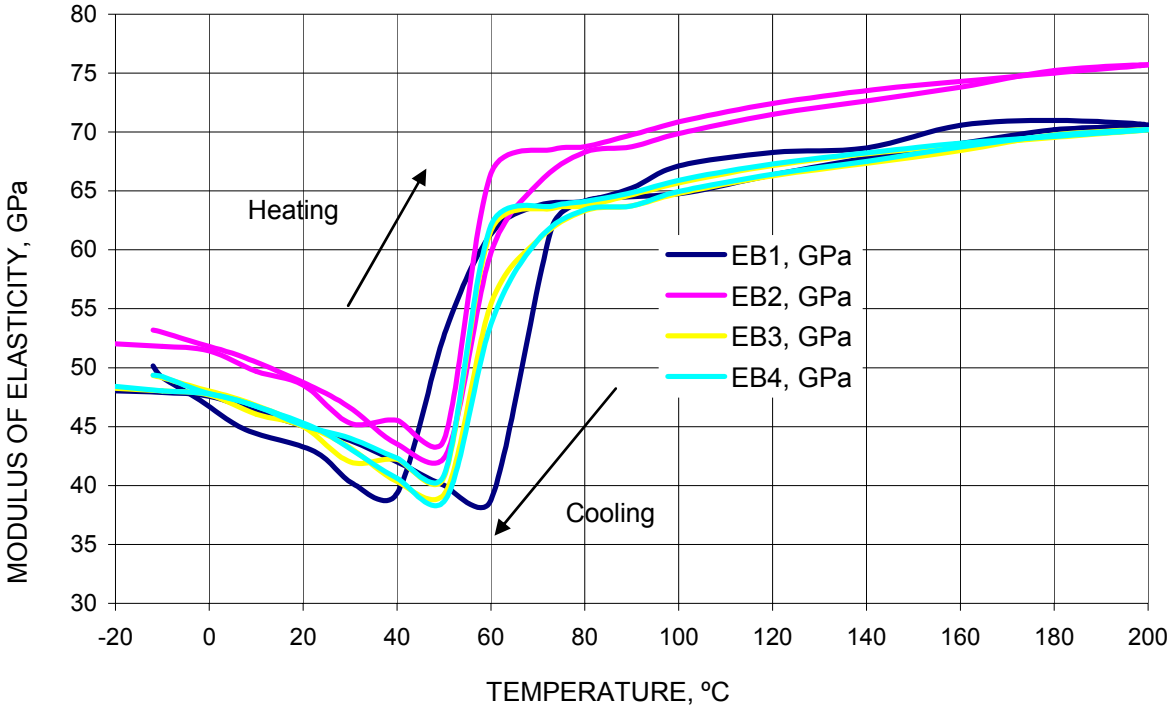

Fig. F.3. Modulus of elasticity of NiTiNOL as a function of temperature, based on the first four bending modes of 25.0 mm long sample.

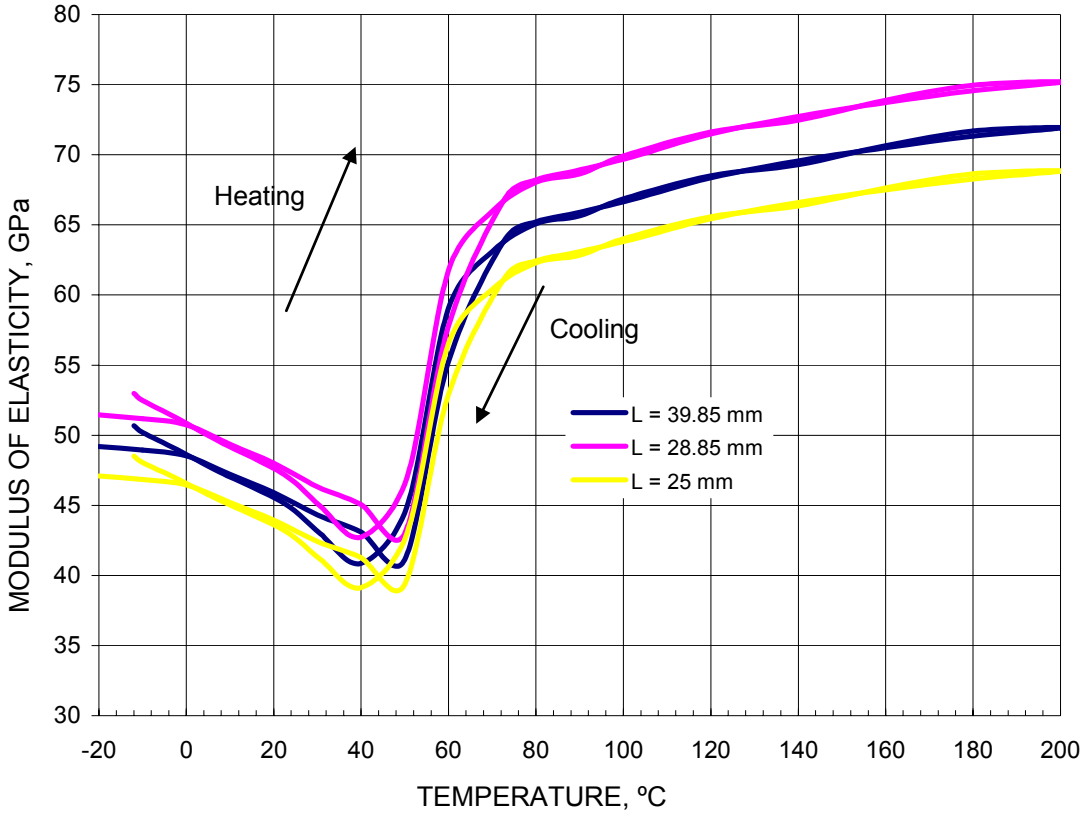

Fig. F.4. Average modulus of elasticity of NiTiNOL as a function of temperature for all three lengths.

APPENDIX G. Thermomechanical response of NiTiNOL-polymide composite

As discussed in Chapters 7 and 8, OEH was used to obtain frequency response of the composite made of a polymide matrix with embedded NiTiNOL fibers. Additional runs were performed to determine repeatability of the measurements. It was observed that the results were consistent with each other and cycling did not have a noticeable effect. The runs were conducted to only 100ºC in order to prevent sofenting of the polymide matrix. The composite was measured (cycled) five times and the results obtained are presented in this Section. Figure G.1 represents frequency response of the NiTiNOL as a function of temperature.

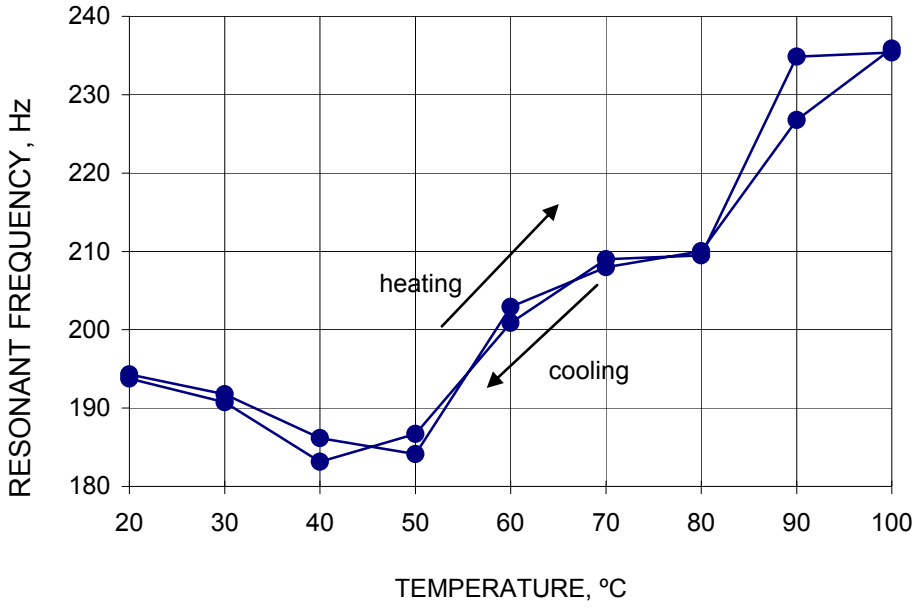

Fig. G.1. Thermomechanical response of a 30 mm by 30 mm NiTiNOL-polymide composite as measured by OEH: Run 02 (Run 01 is included in Chapter 8).

The TT is at around 60ºC. The loop that is encompassed between the heat and cool fibers cycles is attributed to hysteresis on the NiTiNOL. Hysteresis is related to energy absorbed during the course of phase transformation. Figures G.2 and G.3 represent the frequency response of the NiTiNOL-polymide composite after the third and the fourth run cycle (i.e., repetition), respectively. It is interesting to observe that there is not much evidence of a shift in the TT for the NiTiNOL. This could be because of the fact that the NiTiNOL fibers are not cycled long enough (on the basis of temperature) for the phase transformation to be complete.

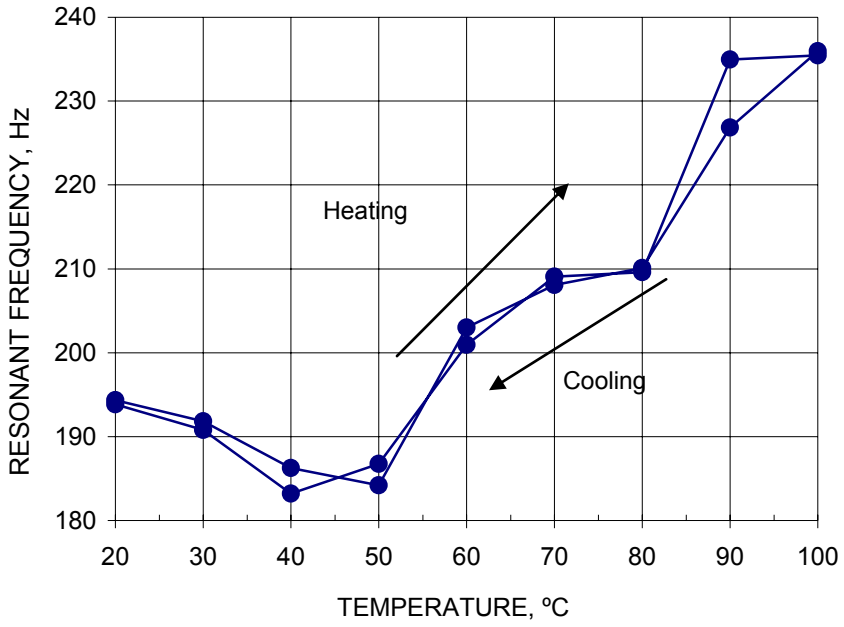

Fig. G.2. Thermomechanical response of a 30 mm by 30 mm NiTiNOL-polymide composite as measured by OEH: Run 03 (Run 01 is included in Chapter 8).

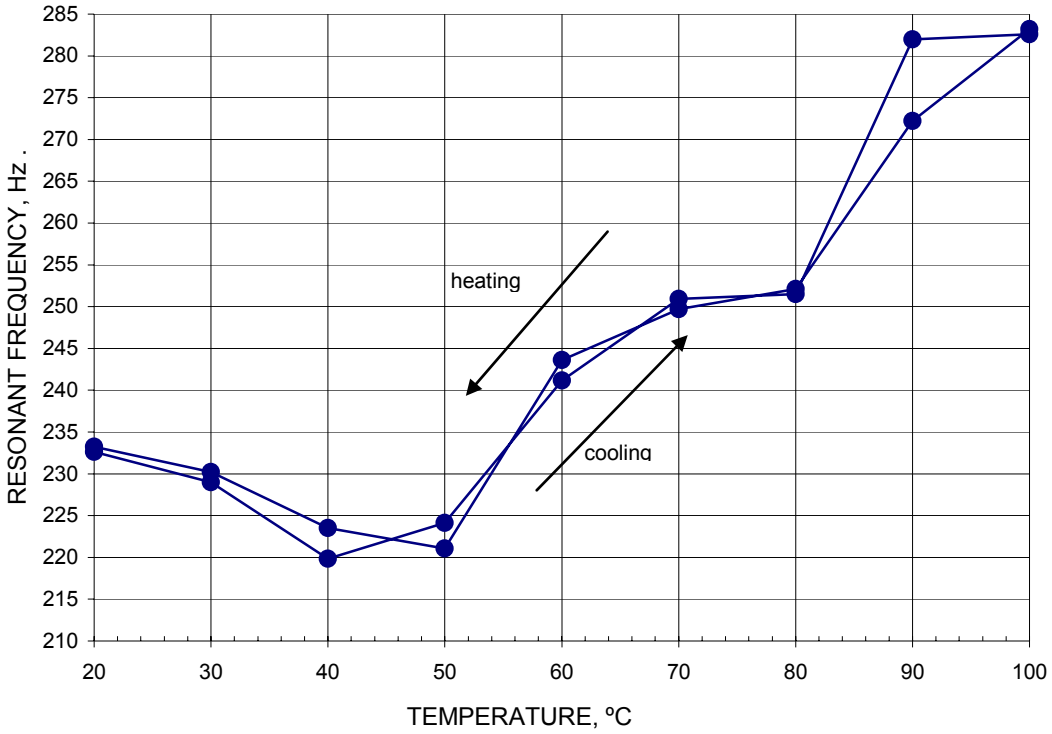

Fig. G.3. Thermomechanical response of a 30 mm by 30 mm NiTiNOL-polymide composite as measured by OEH: Run 04 (Run 01 is included in Chapter 8).

APPENDIX H. Dynamic stiffness determination of NiTiNOL-polymide composite

As discussed in Chapters 7 and 8, the dynamic stiffness D_{11} can be calculated from measured resonant frequencies from OEH. This Appendix provides results obtained for a NiTiNOL-polymide composite with dimensions of 30 mm by 30 mm. Figures H.1 and H.2 represent temperature variations of the dynamic stiffness D_{11} of the composite.

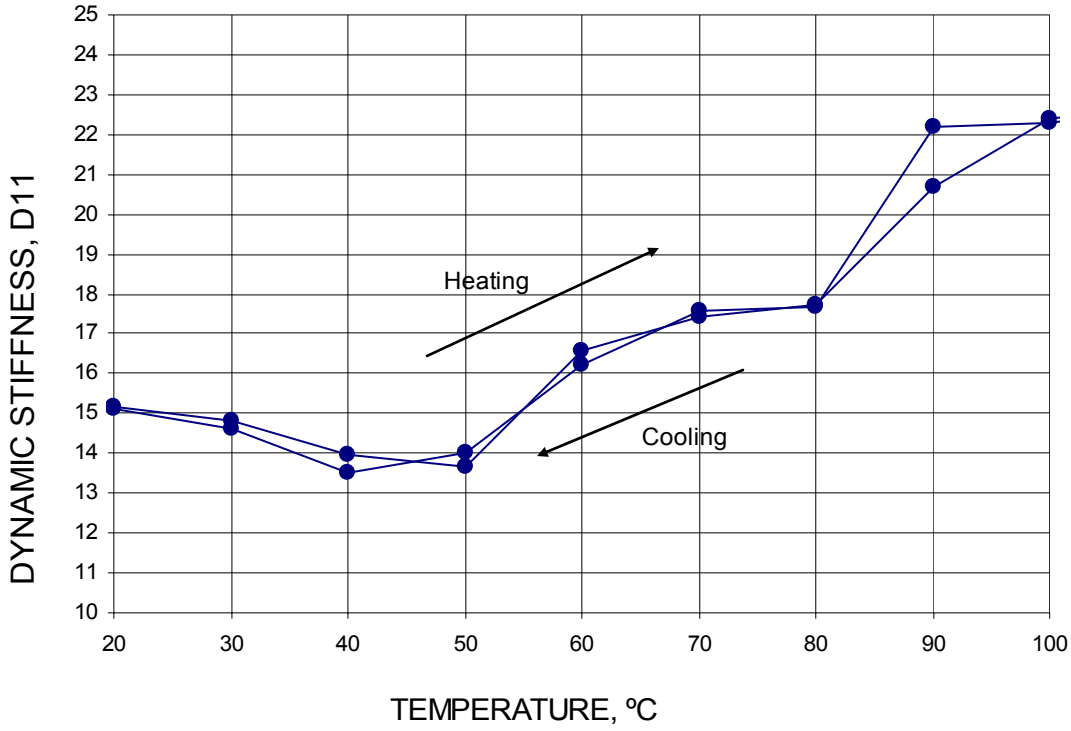

Fig. H.1. Dynamic stiffness of a 30 mm by 30 mm NiTiNOL-polymide composite as measured by OEH (Run 01).

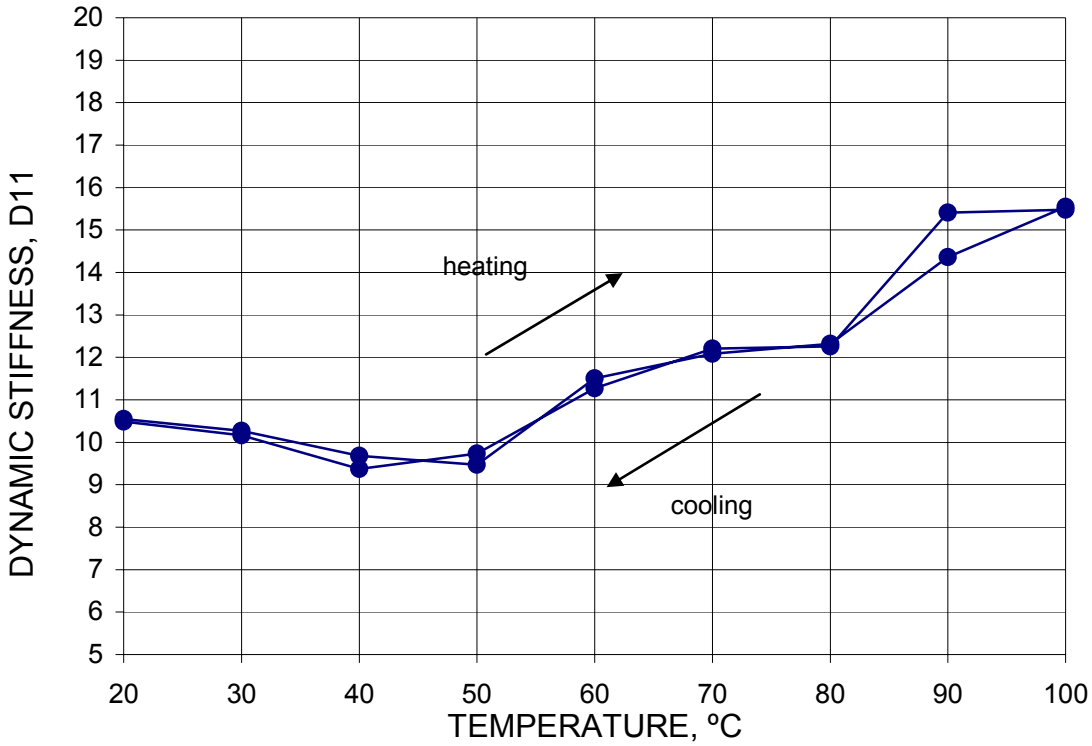

Fig. H.2. Dynamic stiffness of a 30 mm by 30 mm NiTiNOL-polymide composite as measured by OEH (Run 02).

APPENDIX I. Uncertainty analysis (additional results)

Uncertainty analysis is discussed in Chapter 4. Also temperature dependence of the uncertainty in the modulus of elasticity is presented for the active length L = 39.85 mm. Additional results on the temperature dependency of the modulus of elasticity were presented in Appendix F. The uncertainty analysis was performed on the average modulus of elasticity. The average modulus for each active length can be written mathematically as

$$E_{AVG} = \frac{E_{B1} + E_{B2} + E_{B3} + E_{B4}}{4}, \tag{G.1}$$

where E_{AVG} is the average modulus of elasticity, E_{B1}, E_{B2}, E_{B3}, and E_{B4} represent the moduli of elasticity determined from the first, second, third, and the fourth bending modes, respectively.

Figures I.1 and I.2 represent temperature dependence of the uncertainty in the modulus of elasticity for the active lengths of L = 28.82 mm and L = 25.0 mm, respectively. The average modulus of elasticity was calculated based on Eq. I.1. Based on the results obtained, the uncertainty in the modulus of elasticity was determined to be $\pm$ 500 MPa, and the total change of the modulus of elasticity was 1 GPa. The maximum contribution to the uncertainty in the modulus of elasticity came from the length of the samples.

In addition, the uncertainty in modulus of elasticity was also determined based on the RSS principle for the NiTiNOL-Al composite. Results obtained are shown in

Fig. I.2.

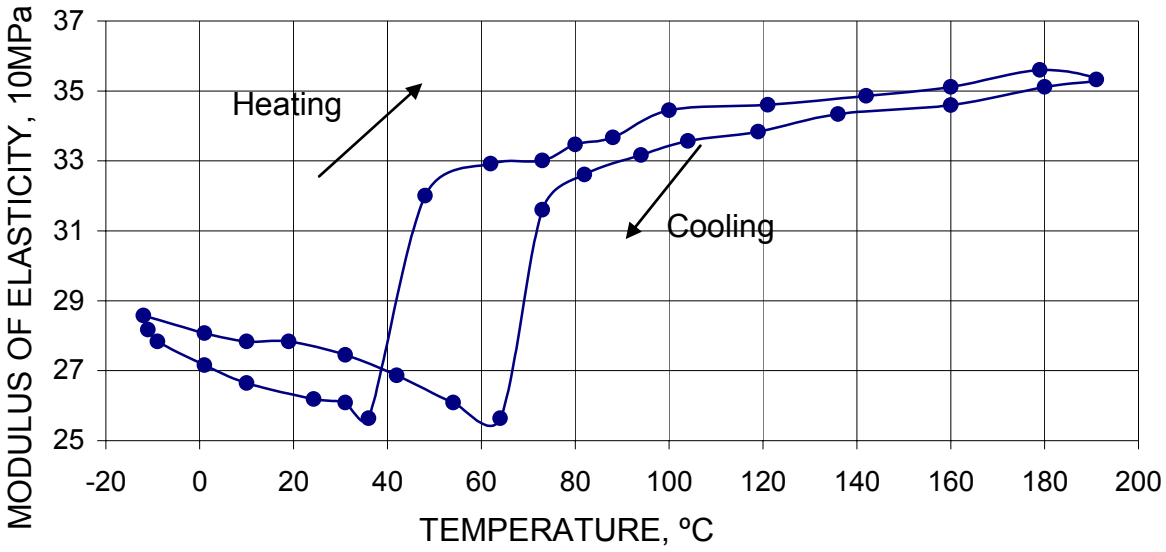

Fig. I.1. Temperature dependence of the uncertainty in the modulus of elasticity for an active length of L = 28.82 mm.

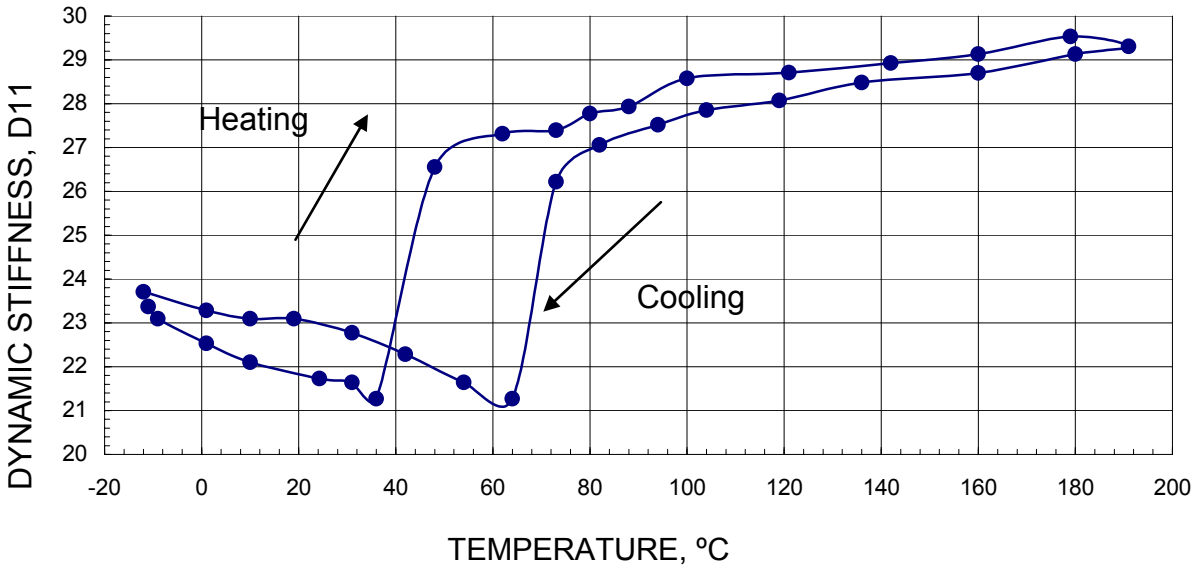

Fig. I.2. Temperature dependence of the uncertainty in the dynamic stiffness for a NiTiNOL-Al composite of 30 mm by 30mm.

APPENDIX J. Comparison of results from FEM and OEH

Results from OEH and FEM were presented in Chapter 8. This Appendix presents a comparison between results obtained for an active length of L = 30.76 mm using a 4-noded thin shell element for the FEM analysis with a mesh density of 360 elements. The OEH experiment was conducted from -20ºC to 200ºC at temperature intervals of 20ºC. Figures J.1 through J.4 represent a comparison between experimental (OEH) and computational (FEM) results for the first four bending modes for a active length of L = 30.76 mm.

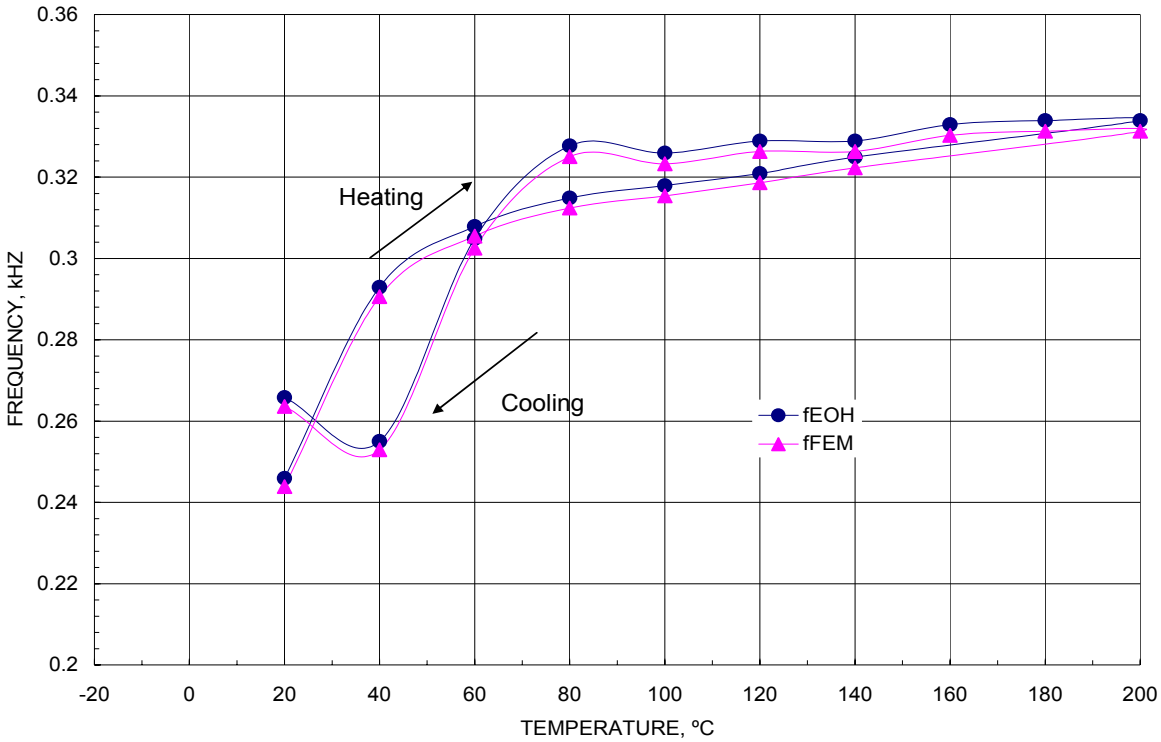

Fig. J.1. Comparison between FEM and OEH for a active length of L = 30.76 mm for the first bending mode.

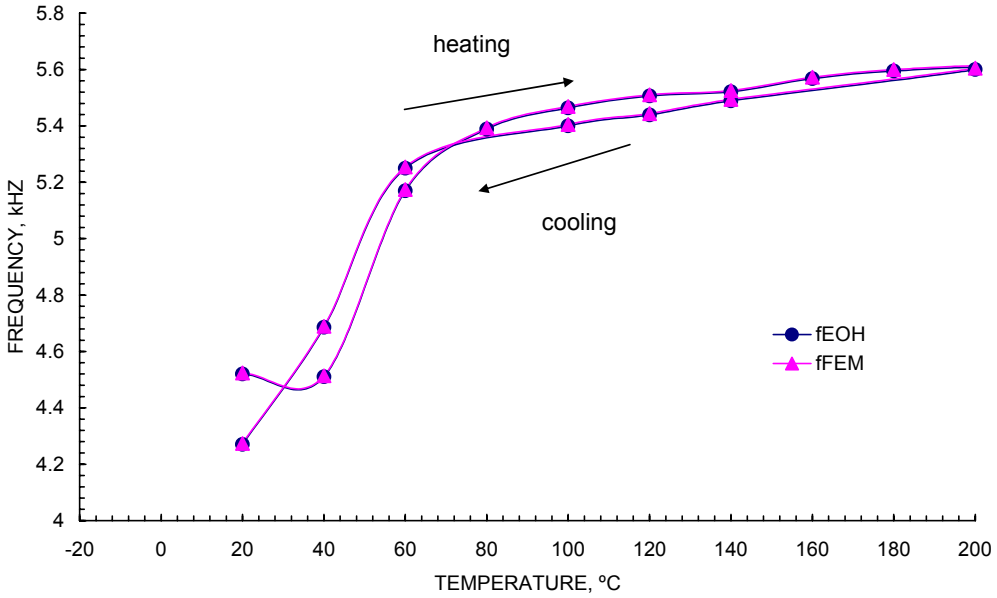

Fig. J.3. Comparison between FEM and OEH for a NiTiNOL-polymide composite 30 mm by 30 mm.

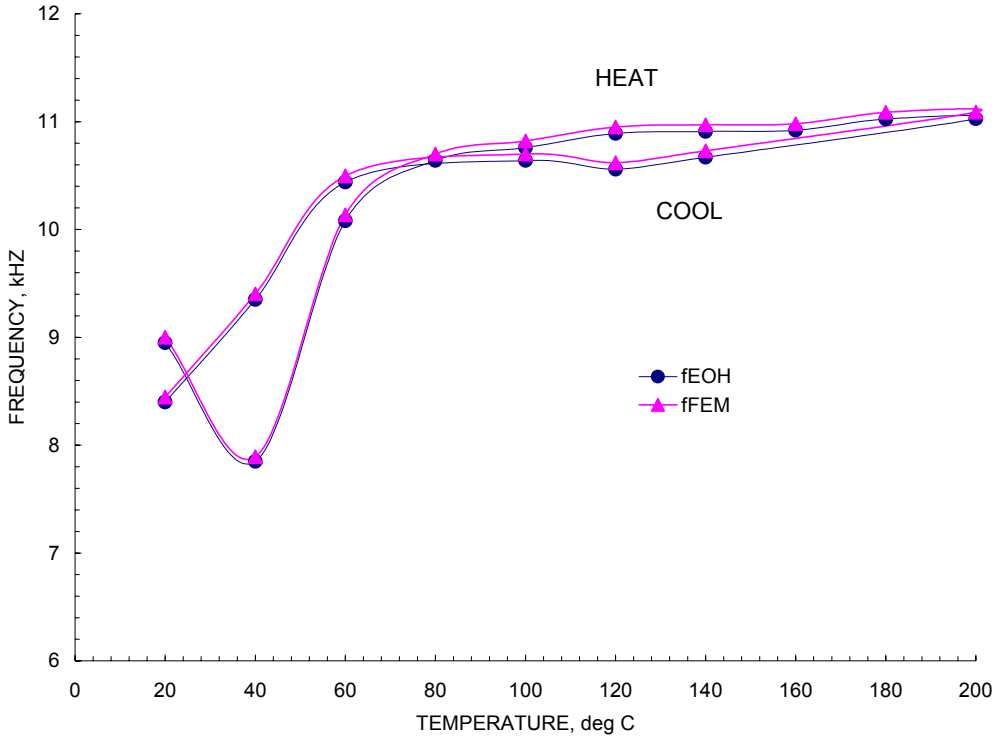

Fig. J.4. Comparison between FEM and OEH for a NiTiNOL-Al composite 30 mm by 30 mm.